Shiraz University

POLITECNICO DI TORINO

School of Electrical and Computer Engineering
Ph.D. Thesis in
Electrical Engineering (Fields and Waves)

Applications of Graphene Metasurfaces for Manipulation of Electromagnetic Waves Scattering

By
Zahra Hamzavi Zarghani

Supervised by
Prof. Alireza Yahaghi (Ph.D.)
Prof. Ladislau Matekovits (Ph.D.)

October 2019

بسم الله الرحمن الرحیم

In the Name of God

Declaration

The undersigned,…Write Your Name Here…, the M.A./Ph.D. student at Shiraz University, holding student number …Write Your Name Here…, hereby declares that this thesis/dissertation is the result of his/her own research, and wherever in this thesis/dissertation, other sources have been used, the exact references or specifications are provided. He/She also asserts that his/her research and its topic are not the repetition of others' works. In addition, he/she commits himself/herself:

1. Not to publish all or parts of the findings of his/her thesis/dissertation in scientific periodicals or academic congregations such as national or international conferences or journals without the prior permission of Shiraz University and his/her supervisor(s).

2. Not to add the name(s) of any other author(s) not included in the thesis/dissertation committee to the article(s) extracted from the thesis/dissertation without the prior permission of his/her supervisor(s).

3. Not to add the affiliation of the co-author(s) from the organizations or institutions other than Shiraz University to the article(s) extracted from the thesis/dissertation without the prior permission of his/her supervisor(s).

Following the code of practice for intellectual property rights, all the material and intellectual rights of the present work are reserved for Shiraz University. If it gets clear that the conditions of the declaration are breached, Shiraz University is fully entitled to take legal action in order to secure its rights at any time and in due order.

…Write Your Name Here…

Date and Signature:

In the Name of God

…Write the Title of Your Thesis/Dissertation in English Here…

By
…Write Your Name Here…

Thesis/Dissertation
Submitted to Shiraz University in Partial Fulfillment of the Requirements for the Degree of
Master of Science (M.Sc.)/ Master of Arts (M.A.)/ Doctor of Philosophy (Ph.D.)

In
…Write the Full Name of Your Field-Major Here…

Shiraz University
Shiraz
Islamic Republic of Iran

Evaluated and Approved by the Thesis/Dissertation Committee as: …Write the Degree Here…

………………………………..	…Supervisor's Name… (Ph.D.), …His/Her Academic Rank… of the Dept. of … His/Her Dept.… (Supervisor)
………………………………..	…Advisor's Name… (Ph.D.), …His/Her Academic Rank… of the Dept. of … His/Her Dept.… (Advisor)
………………………………..	…Advisor's Name… (Ph.D.), …His/Her Academic Rank… of the Dept. of … His/Her Dept.… (Advisor)
………………………………..	…External Examiner's Name… (Ph.D.), …His/Her Academic Rank… of the …His/Her University… (External Examiner)
………………………………..	…Internal Examiner's Name… (Ph.D.), …His/Her Academic Rank… of the Dept. of …His/Her Dept.… (Internal Examiner)

May 2020

To My Dear Parent

Table of Contents

List of Tables

k

List of Figures

m

p

Chapter One

Introduction

Conventional optical devices such as prisms, lenses and mirrors have the ability to control the light propagation based on geometrical and diffractive optics, However achieving these applications in nano sizes is difficult [10]. These optical devices must have big sizes to operate properly. Wavefront shaping in a small size, because of the diffraction limit can not be easily obtained. Progressing in metamaterials, plasmonic and nanophotonic makes control of optical waves accessible out of the diffraction limit [11]. New and interesting phenomenons such as negative refractive index [12]- [14], imaging [15]- [18], and cloaking [19]- [22] using plasmonics and metamaterials which are proved in theory and practice, have opened new horizons for designing optical devices with different desirable applications. In comparison to conventional lenses and imaging devices, metamaterials provide new methods for wavefront shaping with smaller sizes and higher resolutions. Despite huge progress in metamaterials, their operation faces some difficulties because of their high sensitivity to losses and fabrication complexities in 3-D structures. In order to reduce these limits, equivalent 2-D surfaces or metasurfaces with the ability to have the same operation as metamaterials, have been introduced [23].

Metasurfaces are formed by 2-D arrays of scattering particles in subwavelength sizes. They are designed in a way that could convert incident waves to the desired transmitted and reflected waves. In comparison to metamaterials, metasurfaces provide advantageous of being lighter, easier fabrication and less losses, because of their much smaller sizes. It has been proved that using metasurfaces is an efficient

way for controlling amplitude, phase and, polarization of electromagnetic waves. The optical characteristics of each element can be determined by its material, geometry, size, and orientation. By putting each element with different scattering characteristics along a surface, a metasurface providing a high degree of freedom in optical wavefront shaping is formed [24].

Recently, phase discontinuity phenomenon utilizing metasurfaces, has been attracted a lot of interests which has been used for new and interesting applications like planer lenses [25]- [27], processing optical information [28], [29], polarization changing [30], [31], wave front engineering in the transmission and reflection mode [32]- [36], manipulating the orbital angular momentum [37] and 2-D and 3-D holography [38]- [42].

Electromagnetic invisibility can also be achieved using metasurfaces named "mantle cloaking" [43], [44].

Tunable or reconfigurable applications such as dynamic wavefront shaping and adaptive optics are highly desirable which can be realized by using tunable materials in the metasurfaces [1]. Graphene, a single layer of carbon atoms is a very good candidate for this purpose with extraordinary properties, since its Fermi level can be adjusted by DC gate biasing [2]. The combination of metasurface technology and graphene can result in a great dynamic manipulation of electromagnetic waves [1].

Compared to other tunable metasurfaces with active materials such as liquid crystals [3], thermally-modulated materials [4] and mechanically-deformed materials [5], metasurfaces based on graphene have some advantages. Graphene is an ultra-thin material and compatible with silicon photonics and planer metasurfaces [1]. The electrical tuning speed of graphene is extremely high with a wide tuning range.

In 2011, the intensity modulation of electromagnetic waves in a metasurface based on graphene was introduced for the first time [6]. After that several switches and modulators [7], [8] and tunable absorbers [9] were presented. In addition to intensity modulation, recently phase modulation for tunable polarization control

and dynamic wavefront shaping has attracted researchers′ attentions.

In this thesis, designs of several tunable graphene based metasurfaces have been presented. The thesis is organized as follows: Section 2 introduces some applications of metasurfaces and their responses to electromagnetic waves are reported. In chapter 3, a summary of theoretical background about graphene is presented and some graphene based metasurfaces are introduced. In chapter 4, various metasurfaces based on graphene are designed in detail for some applications including: tunable mantle cloaking and scattering manipulation, leaky wave antenna, tunable polarization converter, and reconfigurable planer lens. Chapter 5 concludes the thesis and gives some suggestions for possible future researches.

Chapter two

Applications of metasurfaces

2.1 Anomalous refraction and reflection of electromagnetic wave

When a propagating plane wave encounters a surface between two media consisting of two different homogeneous materials, it will split into reflected and transmitted waves. The amplitude, phase, and direction of the transmitted and reflected waves can be determined using boundary conditions on the surface which are calculated by Fresnel's and Snell's law. If an array of ultra-thin resonators called a "metasurface", is added to the surface, the boundary conditions change because of the resonance effect of the metasurface, hence the transmission and reflection coefficients are modified. Phase changes that will occure to the transmission and reflection waves depend on the frequency of the incident wave. If elements of the array introduce same phase changes, and the transmission and reflection waves' direction will not be changed. However, it is possible to alter the direction of the propagating wave and to control wavefront shaping by producing phase gradient along the metasurface [45]. General laws of wave 's reflection and refraction can be demonstrated [46], [47]. According to Fig. 2.1 we have:

$$n_t \sin \left(\theta_t \right) - n_i \sin \left(\theta_i \right) = \frac{1}{k_0} \frac{d\phi}{dx} \tag{2.1}$$

$$\cos \left(\theta_t \right) \sin \left(\theta_t \right) = \frac{1}{n_t} \frac{1}{k_0} \frac{d\phi}{dy} \tag{2.2}$$
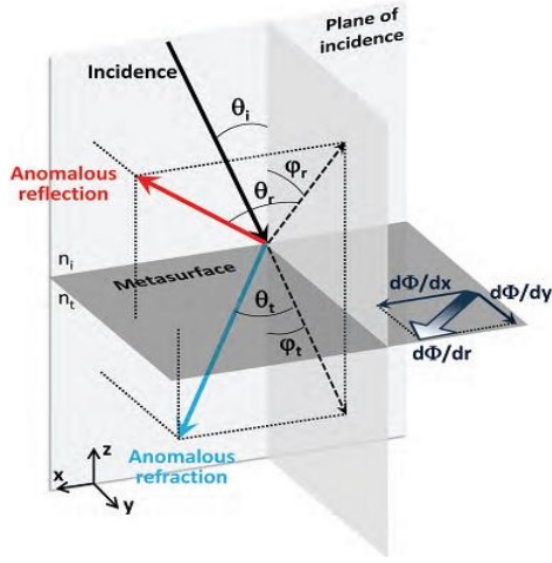
Figure 2.1: A metasurface with phase gradient element [45]

$$\sin\left(\theta_r\right) - \sin\left(\theta_i\right) = \frac{1}{n_i}\frac{1}{k_0}\frac{d\phi}{dx} \tag{2.3}$$

$$\cos\left(\theta_r\right)\sin\left(\phi_r\right) = \frac{1}{n_r}\frac{1}{k_0}\frac{d\phi}{dy} \tag{2.4}$$

where the angles are shown in Fig. 2.1 and $\frac{d\phi}{dx}$ and $\frac{d\phi}{dy}$ are the phase gradient components in x and y directions, respectively. The first two sets relate the transmission wave to the incident wave and the other two sets relate the reflection wave to the incident wave. These general laws show that the direction of transmission and reflection waves can be controlled by the relative permittivity of the two media and by the phase gradient of the elements.

One of the examples of anomalous refraction is bending the incident wave using C-shape metallic resonators for terahertz frequencies [48]. Elements of the considered metasurface should rotate along the surface in a way that provides required phase changes. The required phase of each element in order to bend the transmitted wave with an angle $\theta_{bending}$ can be calculated from eq. (2.5) which is a simplified formula of generalized laws of refraction [45],
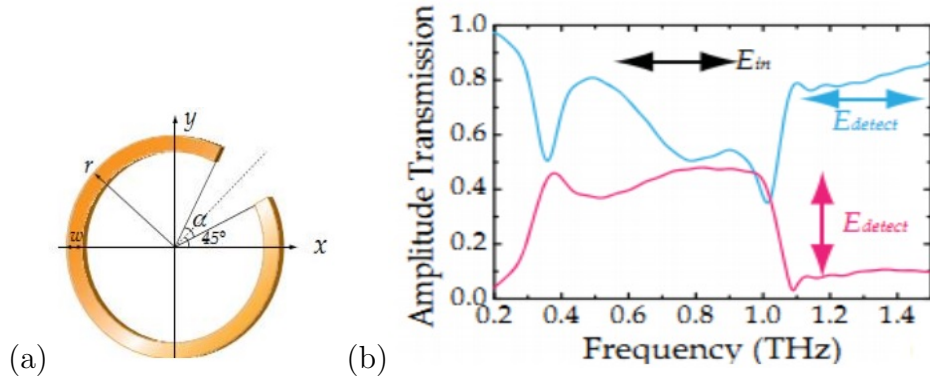
Figure 2.2:   (a) Split ring resonator as the element of the metasurface, (b) Amplitude of transmitted wave versus frequency [48].

$$\phi(x) = \frac{2\pi}{\lambda_0} x \sin\left(\theta_{bending}\right) \tag{2.5}$$

where $\phi(x)$ is the required phase for the element at a distance x from the origin and λ_0 is the wavelength in free space at the considered frequency.

Figure 2.2 shows the proposed element and the magnitude of the transmitted wave for different frequencies. It can be seen that at the frequency of 1THz there is a minimum and maximum in the magnitude for co and cross polarization, respectively. Since phase control is easier for a cross polarized wave [49], therefore, the metasurface has been designed to operate at 1THz for a cross polarized electromagnetic wave.

Figure 2.3(a) shows a super cell of the metasurface with its transmitted amplitude and phase response according to the rotation angle of the rings. It is illustrated that 360 degrees phase range can be achieved by the elements ' rotation. This super cell will be the building block of the considered metasurface. The transmission response of the metasurface for frequencies of 0.63THz, 0.8THz and 1THz are shown in Fig. 2.3(b).

The general law for reflection from reflectarrays is also investigated in some researches. In [50], a reflectarray antenna has been designed. The antenna consists of conducting elements on top of a thin dielectric substrate backed by the ground plane. Figure 2.4 shows a metasurface based reflectarray. In the pro-
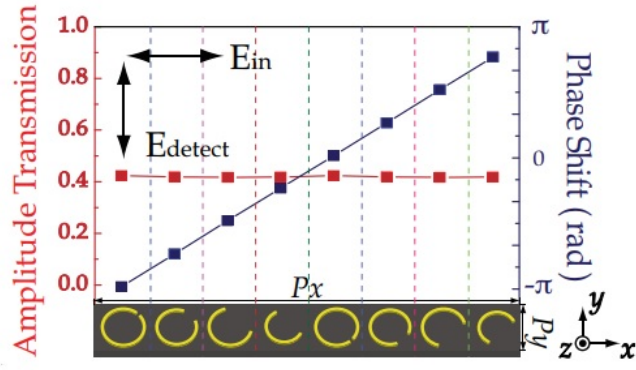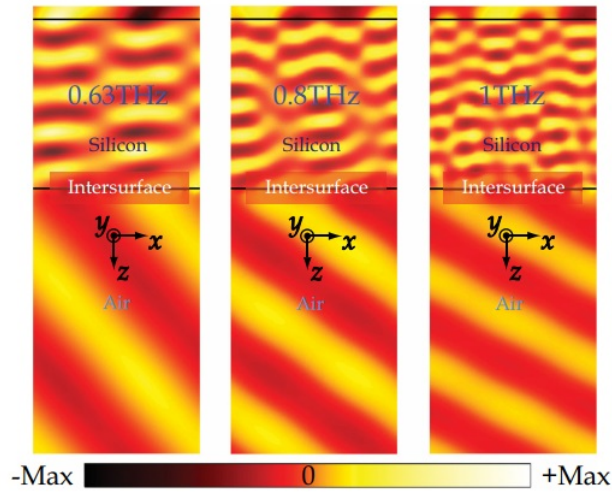
Figure 2.3: (a) Super cell of the metasurface with its transmission amplitude and phase response. (b) Transmitted bending waves for normal incidence at 0.63THz, 0.8THz and 1THz, from left to right [48].

posed metasurface, the required phase shift is achieved by changing the size of the elements.

Another example of a metasurface based reflectarray is shown in Fig. 2.5(a) which consists of H-shape elements and the required phase shift can be achieved by adjusting the size of the cells. Figure 2.5(b) shows the reflected phase of the elements versus the distance from the origin [51].
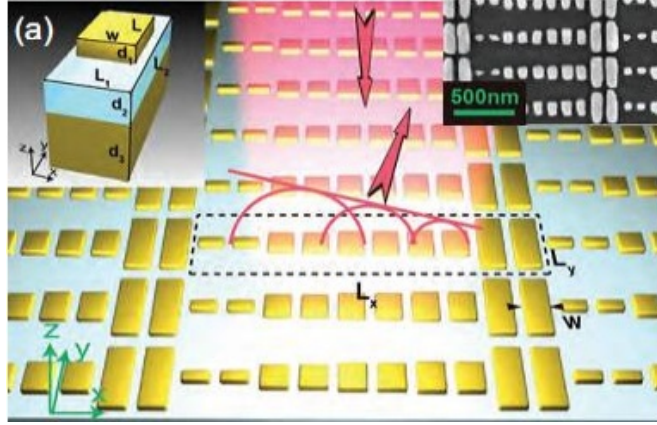
Figure 2.4:   A metasurface based reflectarray [50].

2.2   Wavefront shaping and beamforming

Metasurfaces provide an extraordinary opportunity to control wavefront shaping and producing desired beams [45]. To achieve a flat lens, the transmission phase from the elements of the metasurface must obey to the required phase pattern in eq. (2.6) [52], [53]. In this equation, phase change is applied only in the x direction. In the y direction, the elements are repeated periodically without any changes. Therefore in these antennas, focusing happens in two directions.

$$\phi(x) = \frac{2\pi}{\lambda_0}(\sqrt{F^2 + x^2} - F) \tag{2.6}$$

where $\phi(x)$ is the required phase shift for each element with a distance x from the origin, λ_0 is the wavelength at the centre frequency and F is the distance of the focusing point to the lens surface.

In [54], a 2-D flat lens has been designed using V-shape elements. Figure 2.6 shows a super cell of the considered elements with transmitted amplitude and phase for the cross polarized wave. The curve indicates more than 75% transmission and it can also be seen that 360 degrees phase range is provided using 8 elements with different rotation angles in the super cell. The designed lens is shown in Fig. 2.7. As mentioned above, the elements change in the x direction in order to provide the required phase shift while in the y direction they are repeated without any changes. Figure 2.8 shows a focused wave at the focal
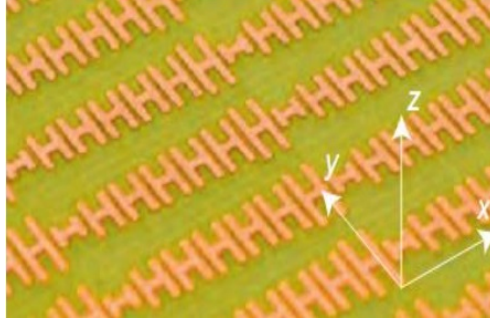
(a)
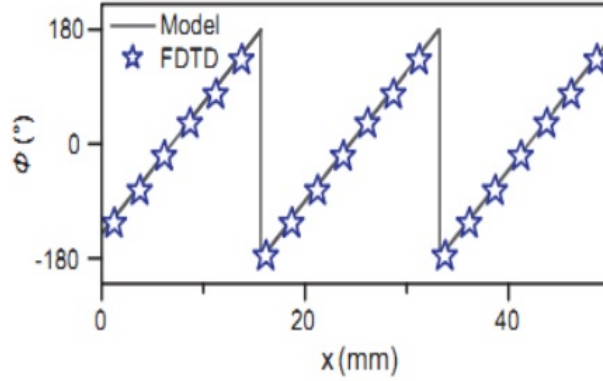
(b)

Figure 2.5: (a) Metasurface consisting of H-shape elements. (b) Reflected phase of the elements [50]

distances of $F = 3$cm and $F = 0.37$mm.

3-D focusing is also possible using eq. (2.7) for the required phase shift $\phi(x, y)$ of the elements in the (x,y) position:

$$\phi(x, y) = \frac{2\pi}{\lambda_0}(\sqrt{F^2 + x^2 + y^2} - F) \tag{2.7}$$

where λ_0 is the wavelength at the resonance frequency and F is the distance of focusing point to the lens surface.

Figure 2.9(a) shows an element consisting of patch and ring resonators and Fig. 2.9(b) shows a metasurface for 3-D focusing. It can be seen that the elements near the origin are larger and they are becoming smaller far from the origin to provide the required phase shift. Figure 2.10(a) [55] shows the transmitted amplitude and phase of an element for different plate width and Fig. 2.10(b) represents

11
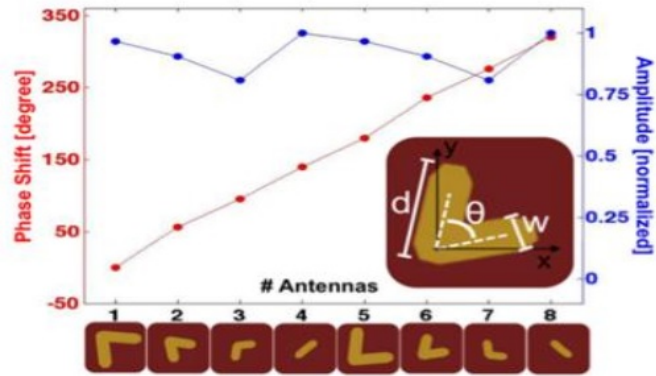
Figure 2.6: A super cell of lens consisting of V-shape elements with cross polarized transmitted amplitude and phase [54].
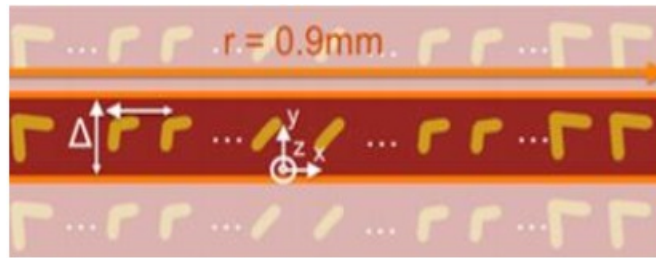
Figure 2.7: A transmit array lens based on a metasurface with V-shape elements. [54].
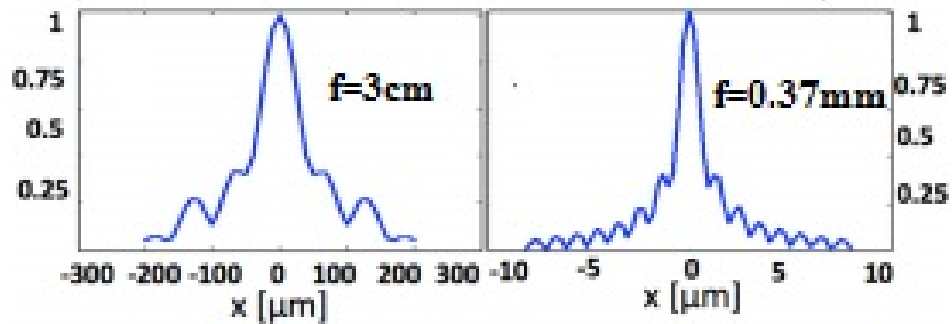
Figure 2.8: The transmitted electric field for the different focal points [54].

12
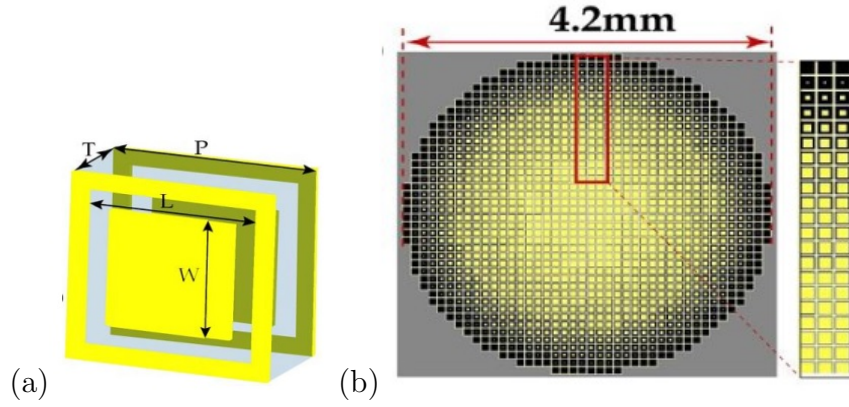
Figure 2.9: (a) An element of a metasurface consisting of patch and ring resonators, (b) transmit array lens for 3-D focusing [55].
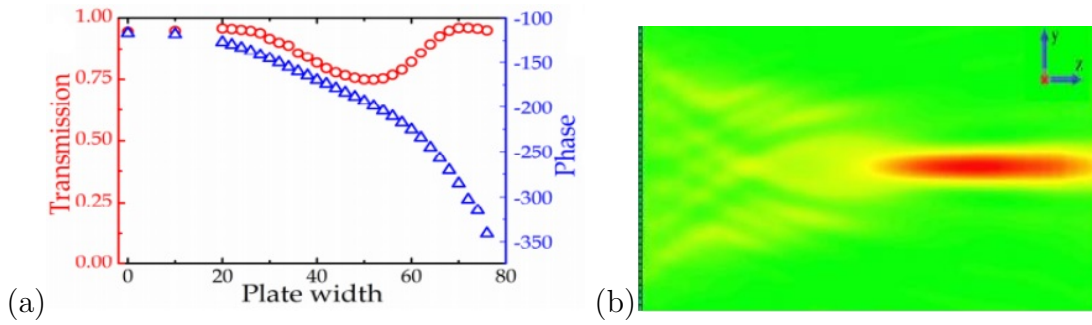
Figure 2.10: (a) Amplitude and phase of the transmitted wave (b) Electric field distribution of the transmitted wave [55].

the electric field amplitude of the transmitted wave from the metasurface. Wave focusing can easily be observed.

In [56] Puncharatnam-Berry phase concept has been used for making phase changes. In this method, subwavelength anisotropic elements with the same size but different rotation angles have been used.

Generally, Jones Matrix related to anisotropic scatterer can be written as follows [56]:

$$M = R(-\theta) \begin{bmatrix} t_o & 0 \\ 0 & t_e \end{bmatrix} R(\theta) \tag{2.8}$$

where t_o and t_e are transmission coefficients for linear polarizations along two main axes for an incident wave. Equation (2.9) represents the rotation matrix

where θ is the rotation angle of the element.

$$R(\theta) = \begin{bmatrix} \cos\theta & \sin\theta \\ -\sin\theta & \cos\theta \end{bmatrix} \qquad (2.9)$$

If $E_I^{R/L}$ is considered as the phasor of the impinging wave with circular right/left (R/L) handed polarizations, the phasor of the transmitted wave ($E_T^{R/L}$) can be written as follows [56]:

$$E_T^{R/L} = M \cdot E_I^{R/L} = \frac{t_o + t_e}{2} E_I^{R/L} + \frac{t_o - t_e}{2} \exp(im2\theta) E_I^{L/R} \qquad (2.10)$$

The first term illustrates a part of the transmitted wave with circular polarization and the same handedness as of the incident wave and the second term shows a part of transmitted wave with circular polarization with different handedness. Puncharatnam-Berry phase shift is equal to $m2\theta$; m is equal to -1 for right handed impinging wave and +1 for left handed one and θ is the rotation angle of the elements. From eq. (2.10) it can be understood that the transmitted wave with the same handedness as the incident wave does not produce any phase change. Therefore, to control the phase we can only use a part of the transmitted wave with opposite handedness to the incident wave. According to eq. (2.10), a phase shift equal to twice of the rotation angle of the element for transmitted wave can be achieved. If the transmission coefficients related to the two main axes have the same amplitude and 180 degrees phase difference, the first term will vanish and the second term will remain with the phase shift of twice of the elements $'$ rotation angle.

Figure 2.11 shows an element as a building block of a metasurface lens using Puncharatnam-Berry phase concept [56]. The parameters α_1, α_2, R_1, R_2, R_3 and R_4 have been optimized such that the required transmitted amplitude and phase related to the two main axes have been achieved. Figure 2.12(a) indicates that the transmitted amplitude for the two main axes (y and z axes) are the same at
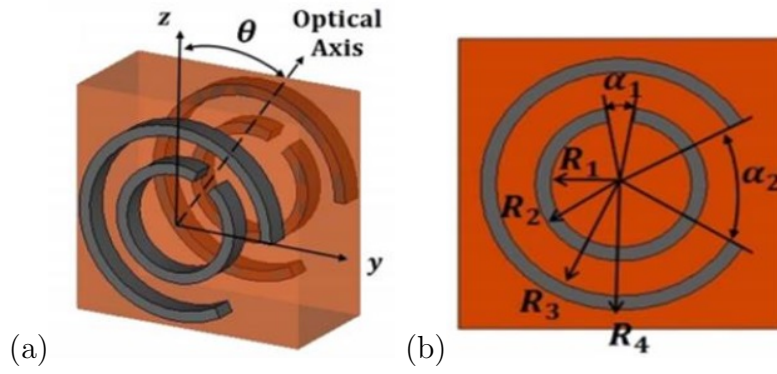
Figure 2.11: An element of a metasurface consisting of double split ring resonators, (a) 3-D view, (b) top view [56].

193.5THz and Fig. 2.12(b) illustrates that at this frequency, the two transmitted waves have a 180-degree phase difference. Therefore, the desired conditions for producing the Puncharatnam-Berry phase shift are provided. Figure 4.34 shows the transmitted amplitude and phase of the transmitted wave for an impinging wave with circular polarization versus different rotation angles of the element. Figure 4.34(a) indicates that the cross polarized transmitted wave′s amplitude is half of the incident wave′s amplitude while the co polarized one is almost zero. Furthermore, Fig. 4.34(b) shows that the rotation of elements causes the cross polarized transmitted phase shift to be twice as large as the angle of rotation. It can be seen that the phase curve for right handed circularly polarized impinging wave decreases and the curve for left handed circularly polarized wave increases with the rotation angle of elements. Therefore, the elements′s rotation provides the required phase shift to bend, focus and diverge the incident wave.

Figure 2.14 shows the required phase shift for 8 elements to achieve transmitted 30 degrees bending wave which has been calculated from eq. (2.5). Figure 2.15 reports the transmitted electric field distribution for right and left handed circularly polarized incident wave, when the elements rotate in clockwise direction. It is observed that the transmitted electric field bends with angle of 30 degrees confirming the Puncharatnam-Berry phase theory. It is worth noting that for a right handed circularly polarized (RHCP) incident wave, transmitted wave is a left handed circularly polarized (LHCP) and vice versa. To address the
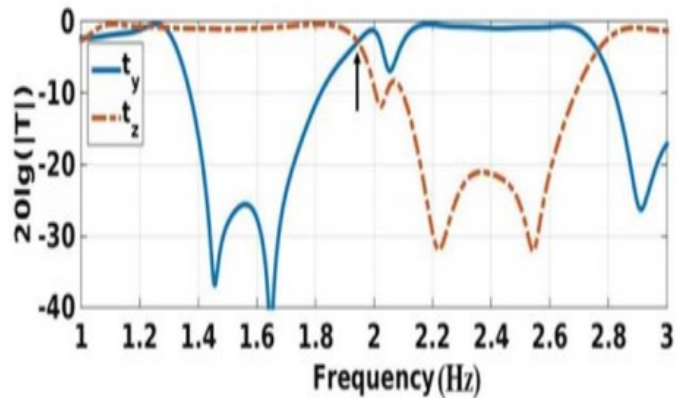
(a)
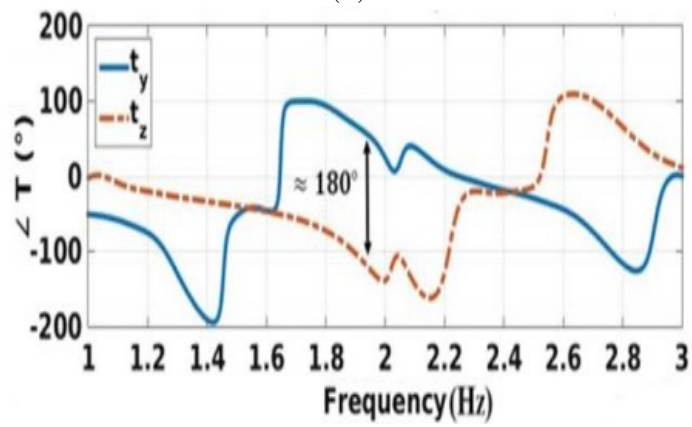
(b)

Figure 2.12: (a) Transmitted amplitude for the two main axes, (b) Transmitted phase for the two main axes [56].
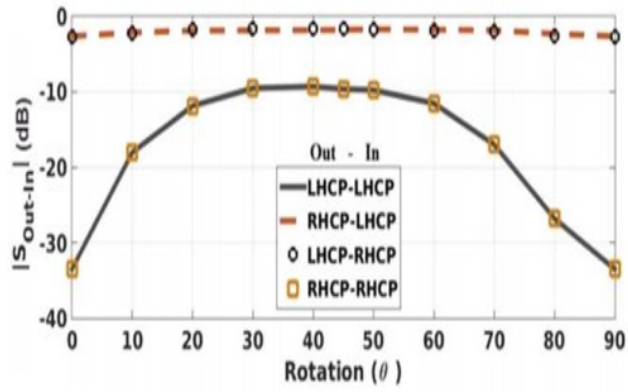
(a)
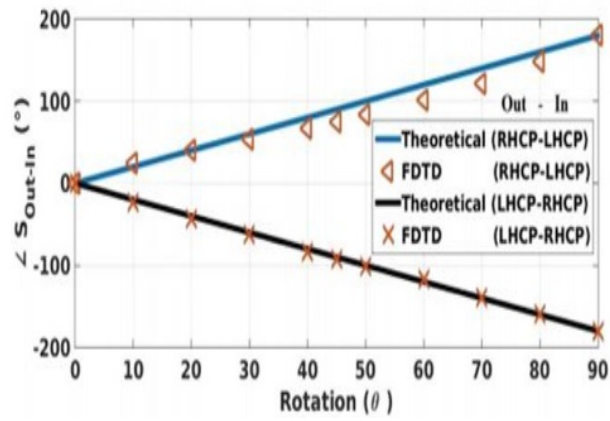
(b)

Figure 2.13: (a) Transmitted wave's amplitude, (b) Transmitted wave's phase versus element's rotation angle [56].
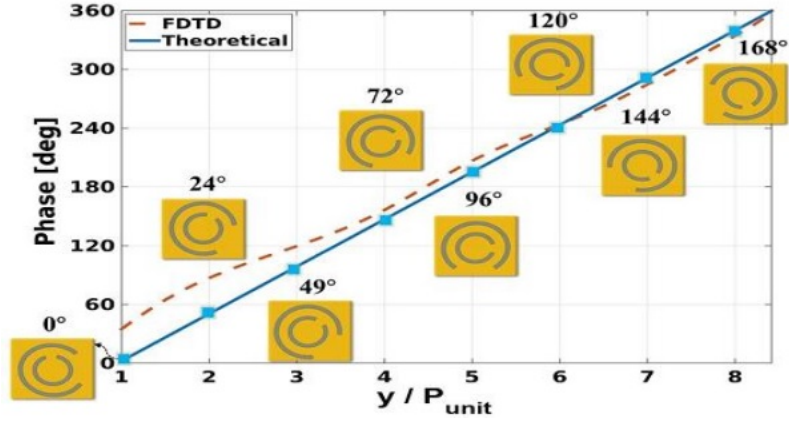
Figure 2.14: The required phase shift for bending the transmitted wave with an angle of 30 degrees. [56].

(a)

(b)
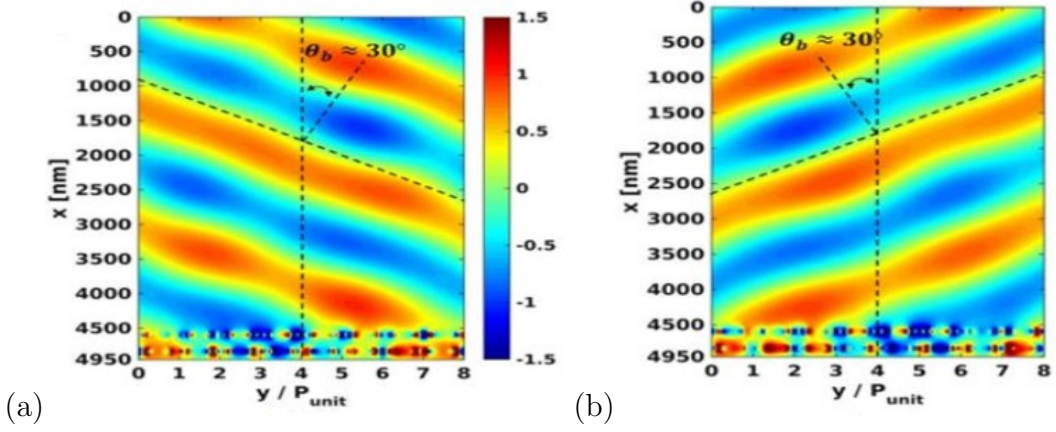
Figure 2.15: Electric field distribution for (a) LHCP, (b) RHCP incident wave [56].

difference between Fig. 2.15(a) and (b) we refer to the fact that for RHCP wave the elements which rotate θ degree in clockwise direction, produce -2θ phase shift while for LHCP wave these elements introduce 2θ phase shift. This difference causes that two waves with different polarizations to bend 30 degrees in different directions.

Equation (2.6) has been used to achieve wave focusing. Figure 2.16(a) shows 22 elements of a metasurface lens for focusing purpose and Fig. 2.16(b) shows the required phase shift for each element based on their distance to origin. Figure 2.16(c) shows the electric field distribution at 193.5THz which indicates a focused wave.
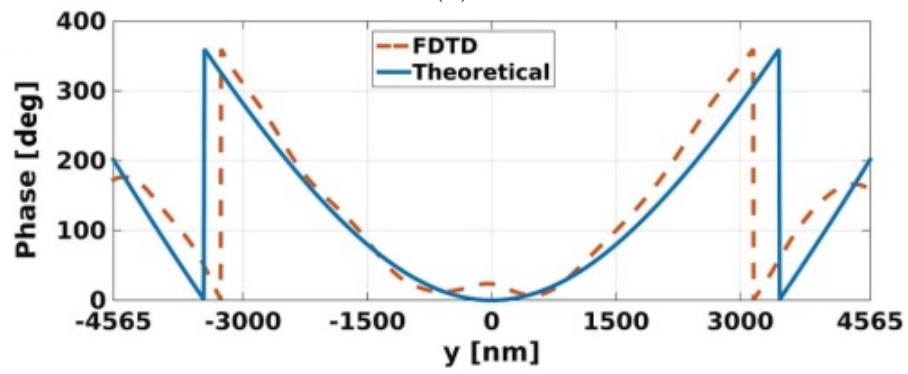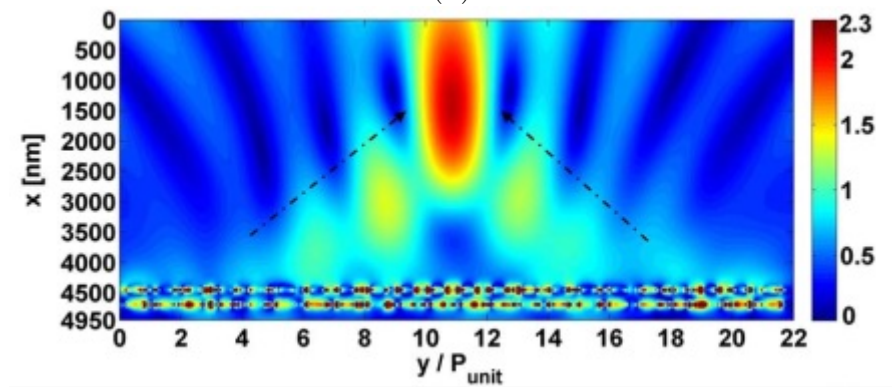
Figure 2.16: (a) A supercell of the metasurface lens, (b) required phase shift for focusing, (c) electric field distribution of the focused wave [56].
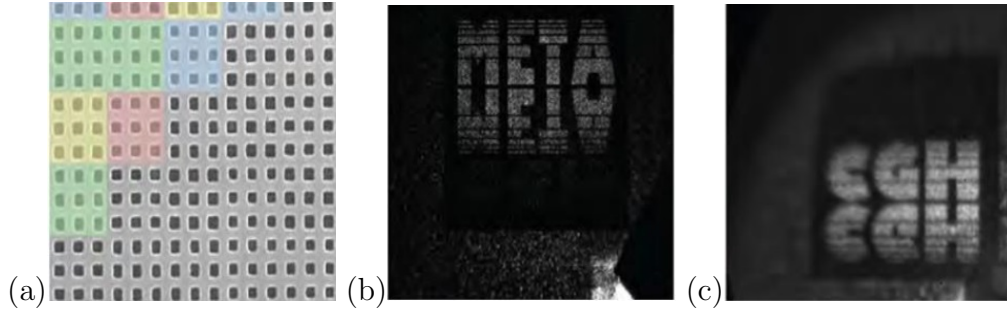
Figure 2.17:   (a) An array of aperture antennas (b) produces hologram at the first frequency, (c) produced hologram at the second frequency [57].

One of the most complex wavefront shaping is creating a holographic image. Amplitude, phase and polarization responses on an interface can be controlled by metasurfaces which make computer-generated holograms, possible. Figure 2.17(a) shows an array of aperture antennas producing a spatially varying transmission coefficient [57]. By designing the elements and adjusting their transmission amplitude, the metasurface is able to produce two different holograms at two different frequencies. The metasurface created the word "META" at the wavelength of 905nm shown in 2.17(b) and created the word "CGH" at the wavelength of 1385nm shown in 2.17(c) in the far field.

In another metasurface for imaging purpose, V-shape aperture antennas shown in Fig. 2.18(a) have been used to create the desired amplitude and phase change [58]. The transmission amplitude and phase of the elements have been adjusted to produce a hologram with the word "PURDUE" in the far field (Fig. 2.18(b)).

20
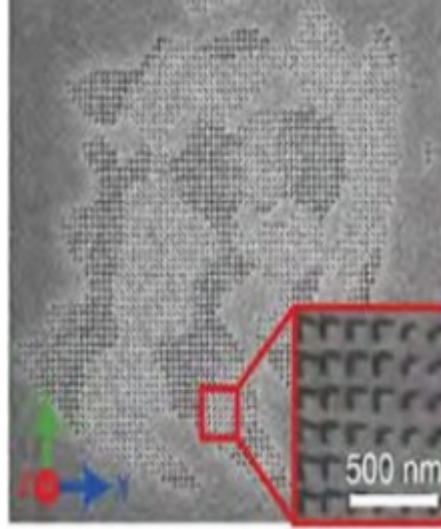
(a)
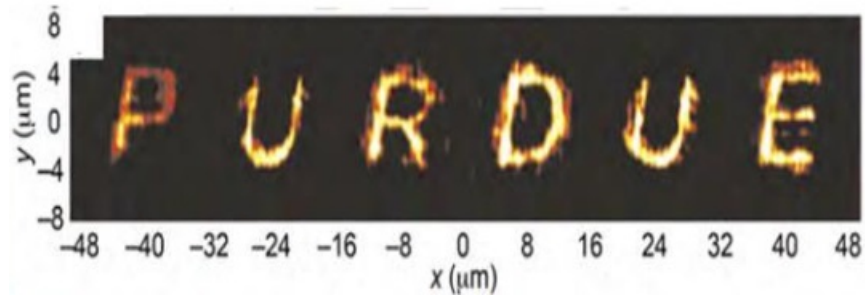
(b)

Figure 2.18:   (a) V-shape aperture antennas, (b) created hologram in the far field [58].

2.3   Polarization conversion

The polarization state is an intrinsic property of electromagnetic waves. Sometimes, it is necessary to convert one polarization state to another one. For example, one of the methods to make a linear polarized wave resistant to variation of environment and scattering is to convert it to a circular polarized wave. Recently, polarization conversion utilizing metasurfaces due to their flexibility and low profile has attracted much interest [45].

2.3.1 Polarization conversion from linear to circular

Figures 2.19(a) and (b) show a metasurface for polarization conversion from linear to circular [59]. Elements of the metasurface consist of two sub cells at a distance of d from each other. The two sub cells produce two transmitted waves with equal amplitude and the same polarization but with the phase difference of 90 degrees as a result of the offset d. The sum of these two waves will give rise to a circularly polarized wave. The polarizer based on metasurface converts linear to circular polarization with an efficiency of 97% and bandwidth from 5 to 12 μm as shown in Fig. 2.19(c).

(a)   (b)

(c)
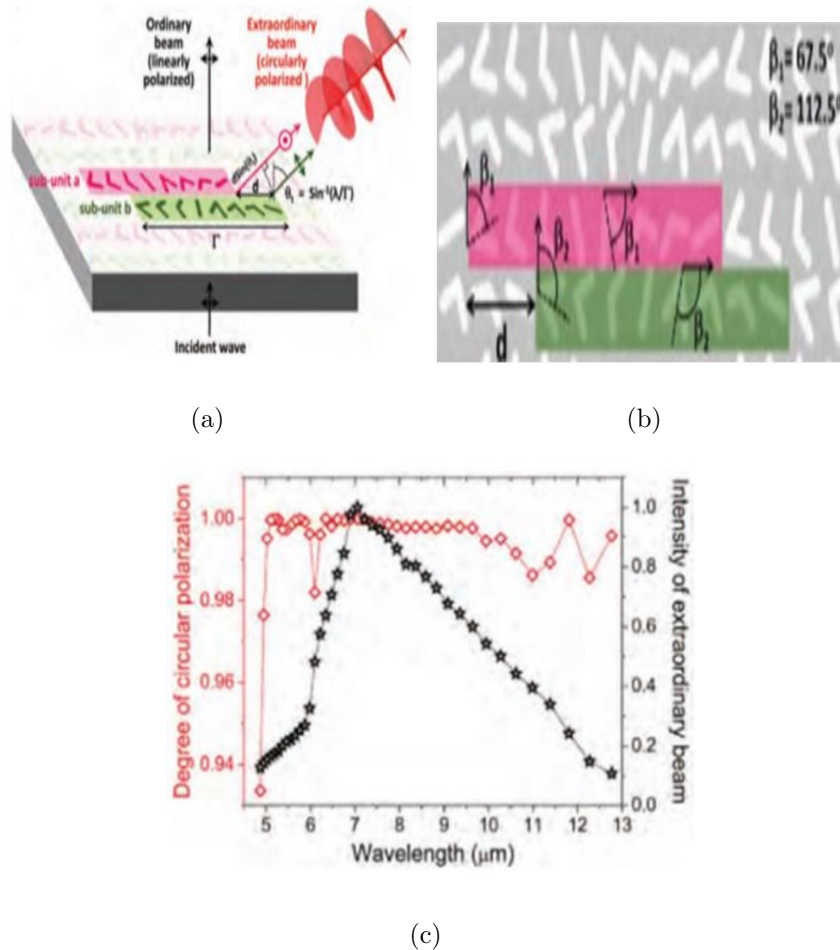
Figure 2.19: A metasurface consisting of two sub cells for linear to circular polarization conversion (a) 3-D view, (b) top view, (c) degree of circular polarization and beam intensity of the circularly polarized transmitted wave [59].

22

2.3.2 Linear polarization rotation

Figure 2.20(a) shows an array of cut-wires on the top of a dielectric polyimide substrate backed by a ground plane for linear polarization rotation for the reflected wave purpose [60]. If a plane wave with linear polarization in the x direction impinges to the structure, a linearly polarized wave in the y direction will be reflected. Figure 2.20(b) shows the reflected amplitude for the co and cross polarized wave versus frequency. It indicates polarization rotation of the incident wave is achieved over a broad bandwidth and with high efficiency.

(a)

(b)
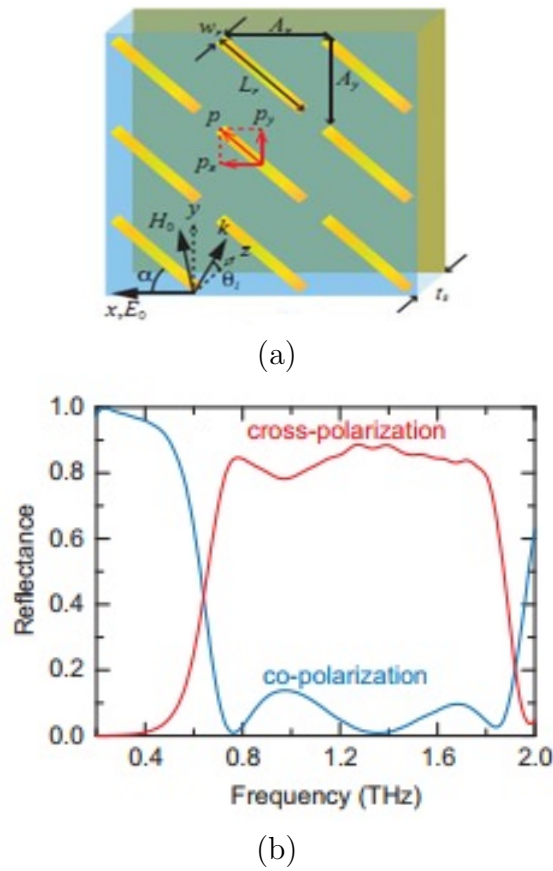
Figure 2.20: (a) Array of cut-wires, (b) reflected amplitude for co and cross polarized wave versus frequency [60].

Linear polarization rotation in transmission mode is another interesting application [45]. Figure 2.21(a) shows an element of a metasurface for linear polarization conversion in transmission mode [61]. It consists of an array of asymmetric split-ring resonators (ASRRs) on the top plane for polarization conversion and an

23
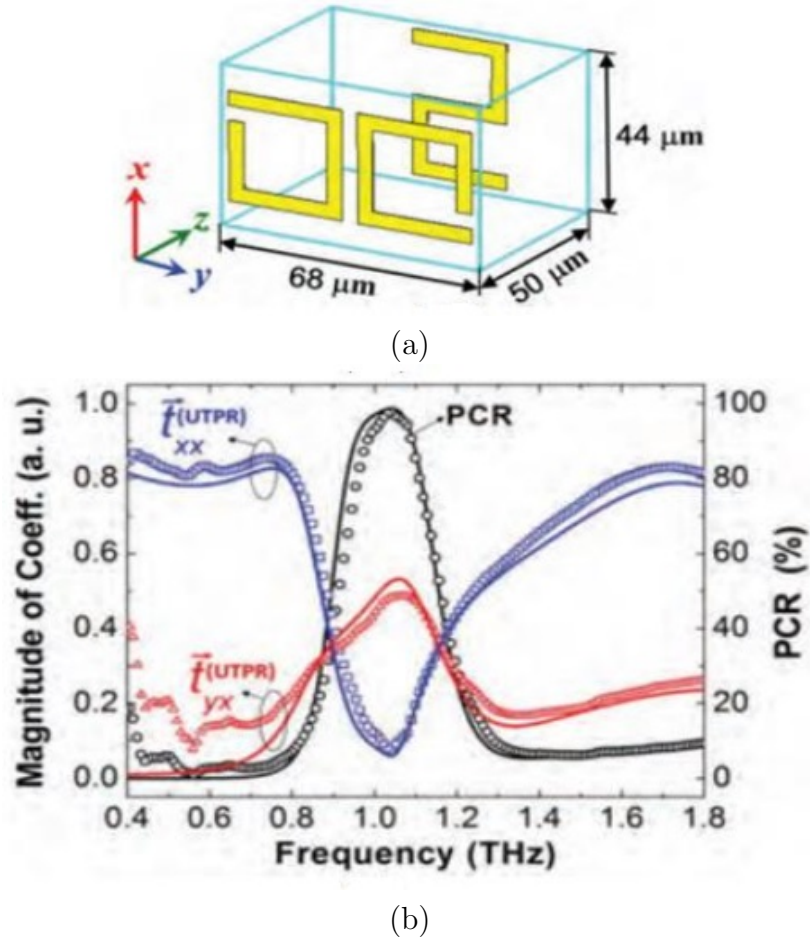
Figure 2.21: (a) An element of a metasurface as a polarization converter, (b) transmitted coefficient for co and cross polarized wave versus frequency [61].

array of S shaped resonators (SR) in the bottom plane for polarization selection. The ASRR makes the impinging y-polarized wave to induce currents and creates electric dipoles in the y-direction, which in turn provides both the x- and y polarized electric fields. The SR has a resonance frequency the same as the ASRR for x-polarized waves, which allows only the y-polarized waves to pass through and blocks the x-polarized waves. It can be observed from Fig. 2.21(b) that the transmission coefficient of the x polarized wave is $t_{yx} = 0.48$ with polarization conversion ratio of (PCR) = 97.7%.

2.4   Scattering manipulation and cloaking

Recently, cloaking has attracted many researchers ′ interest and a lot of investigations have been performed to decrease the visibility of objects [62]- [66]. In [20], a cover constructed of metamaterials has been utilized to cloak the considered object. The cover guides the impinging wave around the object and avoids any interaction of the wave with the covered object; therefore, scattering from the object will significantly reduce [67]. In this method, using transformation optics theory, objects with any dimension, shape and of any material can be cloaked [68]. Reported results for various structures prove the feasibility of this technique [22]. However, a cover of inhomogeneous and anisotropic metamaterial is not easily realizable, so they are not good candidates in practice [69], [70].

Another technique is plasmonic cloaking which is based on scattering cancellation method. In this method, introduced in [71], a thick cover consisting of materials with near zero or negative relative permittivity coats the object and an anti-phase scattered field compared to the field scattered by the uncovered object cancel each other and the object will become invisible [72]- [75]. The scattering cancellation method can also be achieved by using ultra-thin metasurfaces. This method is called mantle cloaking [76]. In this technique, an ultra-thin metasurface covers the object. The scattered field of the metasurface which is caused by an induced current and the field scattered by the object cancel out each other because of their anti-phase electric field resulting in an invisible covered object [77]- [81].

In [82], a cylinder with a radius of 0.14 λ and relative permittivity of $\epsilon_r = 4$ has been cloaked utilizing a metasurface based on graphene. To achieve invisibility with a metasurface, it is necessary to write the electric field inside and outside of the object and then apply boundary condition on the surface of the object to obtain the required surface impedance of the metasurface. Figure 2.22(a) shows a dielectric cylinder covered by the designed graphene metasurface which is exposed to a TM_z polarized plane wave. The impinging wave propagates in the x direction normal to the cylinder and the electric field is in the z direction. The electric

field can be written as:
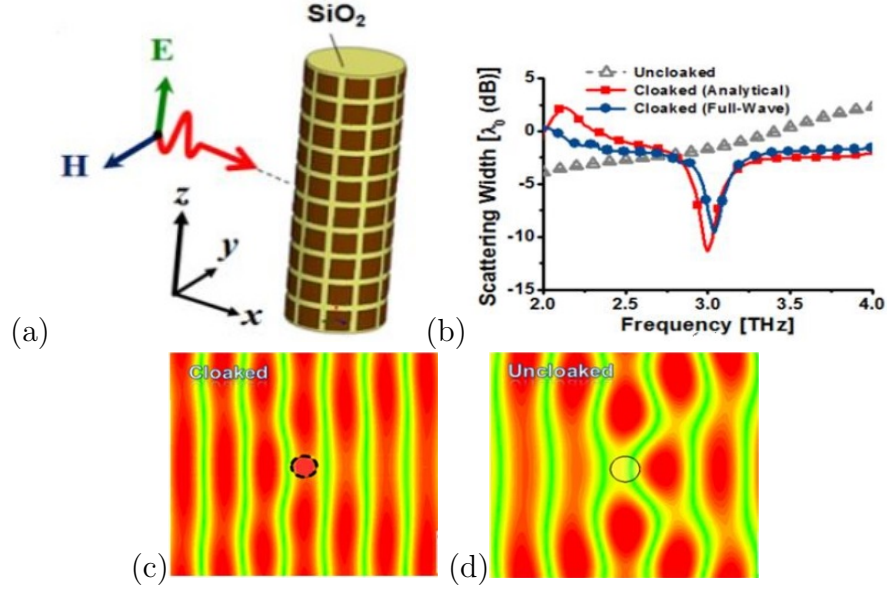
Figure 2.22: (a) A dielectric cylinder covered by a metasurface (b) Scattering width for the uncloaked and cloaked cylinders, (c) electric field distribution for cloaked cylinder, (d) electric field distribution for uncloaked cylinder [82].

$$E^i = \hat{z}E_0 exp(-j\beta x) \tag{2.11}$$

which can be written as an infinite sum of Bessel functions. [83]:

$$E_z^i = \hat{z}E_0 \sum_{n=-\infty}^{\infty} j^{-n} J_n(\beta_0 r)e^{jn\phi} \tag{2.12}$$

The scattered field can be written as an infinite sum of Hankel functions [83]:

$$E_z^s = \hat{z}E_0 \sum_{n=-\infty}^{\infty} j^{-n} \, C_n \, H_n^{(2)}(\beta_0 r)e^{jn\phi} \tag{2.13}$$

The electric field outside the cylinder is the sum of the incident electric field and scattered electric field. The electric field inside the object is:

$$E_z^{in} = \hat{z}E_0 \sum_{n=-\infty}^{\infty} j^{-n} a_n J_n(\beta r)e^{jn\phi} \tag{2.14}$$

where J_n and $H_n^{(2)}$ are Bessel and Hankel function of the first kind and the second

kind, respectively. β_0 and β are propagation constant in the air and dielectric, respectively. By applying the boundary conditions we have:

$$E_{in} = E_{out} = E \tag{2.15}$$

$$E = Z_s \times (H_{out} - H_{in}) \tag{2.16}$$

where E_{in}, E_{out}, H_{in} and H_{out} are electric and magnetic fields inside and outside the cylinder. Z_s is the surface impedance of the metasurface based on graphene patches. It can be calculated from eq. (2.17) [84]:

$$Z_s = \frac{D}{\sigma_s(D-g)} - j\frac{\pi}{2\omega\epsilon_0(\frac{\epsilon+1}{2})D\ln\csc(\frac{\pi g}{2D})} \tag{2.17}$$

where D and g are the periodicity and the gap size respectively, ϵ is relative permittivity of the cylinder and σ_s is the conductivity of graphene.

By applying boundary conditions, a matrix equation with unknown coefficients a_n and c_n is obtained. The coefficients a_n and c_n can be achieved by solving this matrix equation. In order to make the scattering of the object to be zero, scattering coefficients c_n should be zero for all n. However, for the cylinders with a radius much smaller than the wavelength, c_0 is the largest coefficient among all other scattering coefficients and have much more contribution in producing the scattered field of the object [83]. Therefore, if c_0 becomes zero, the scattering of the object will be significantly reduced. By equating c_0 to zero, the required surface impedance Z_s versus frequency can be achieved. In the next step, the size of the elements of the metasurface and also the graphene conductivity are determined. In Fig. 2.22(b) scattering width (SW) of the uncloaked and cloaked cylinders are shown. It can be observed that the scattering of the cloaked cylinder at the centre frequency of 3 THz is much smaller than that of the uncloaked one. Figure 2.22(c) and 2.22(d) show uncloaked and cloaked cylinders in presence of incident electric field which indicates that the cloaked cylinder produces much

27
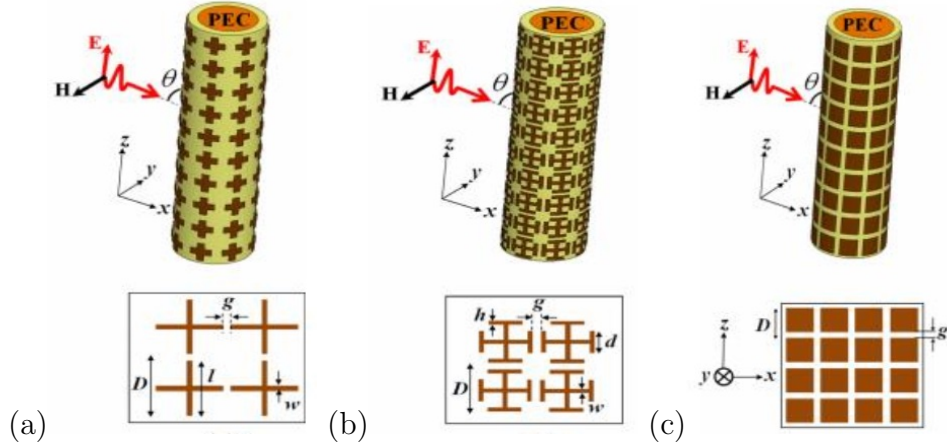
Figure 2.23: Conducting cylinders covered by different metasurfaces (a) cross dipoles (b) Jerusalem crosses, (c) patch array [85].

less perturbation compared to the uncloaked one. From these simulated results, the proper performance of the designed covering metasurface is verified.

In [85], various kinds of metasurfaces have been introduced and their surface impedances have been calculated. Figure 2.23 shows 3 different metasurfaces which are placed on dielectric layers that cover the conducting cylinders. The goal of covering the cylinders with these metasurfaces is reducing their scattering and consequently, making them invisible. Figure 2.24 shows SW of the conducting cylinders uncovered and covered by the metasurfaces introduced in Fig. 2.24. It can be understood that cloaking the cylinders can be achieved with different kinds of metasurfaces.

In [86], two layers of metasurfaces have been used in order to cloak a conducting cylinder for two modes of TE and TM, simultaneously. Figure 2.25(a) shows the cylinder covered by the two metasurfaces and Fig. 2.25(b) shows the radar cross section (RCS) of the uncloaked and cloaked cylinders for both TE and TM modes. Good cloaking performance of the coating metasurfaces can be observed for the two modes.

In [87], an inhomogeneous metasurface for the purpose of increasing cloaking bandwidth has been used. In homogeneous metasurfaces, there is one plasma resonance frequency which is dependent on the size and material of the elements. To create another resonance frequencies, inhomogeneous metasurface with differ-
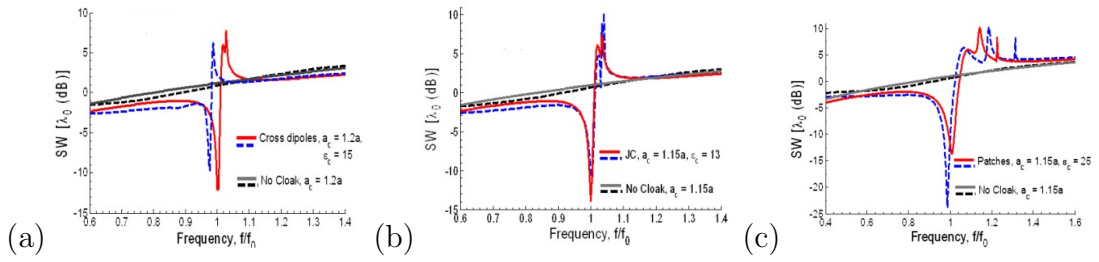
Figure 2.24: SW of the Conducting uncloaked and cloaked cylinders covered by different metasurfaces (a) cross dipoles, (b) Jerusalem crosses, (c) patch array. Solid line represents the analytical results and dashed line shows the simulation results [85].

(a)

(b)
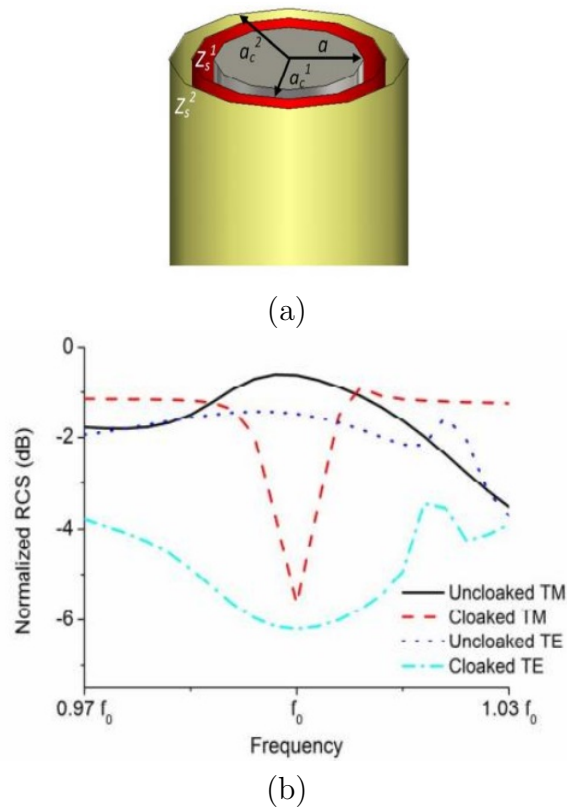
Figure 2.25: (a) Conducting cylinder covered by two metasurfaces, (b) RCS of the uncloaked and cloaked cylinders [86].
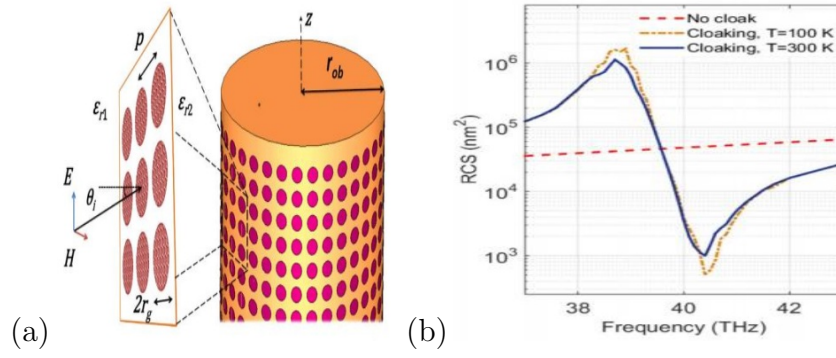
Figure 2.26: (a) A dielectric cylinder covered by a homogeneous metasurface, (b) RCS of uncloaked and cloaked cylinders [87].
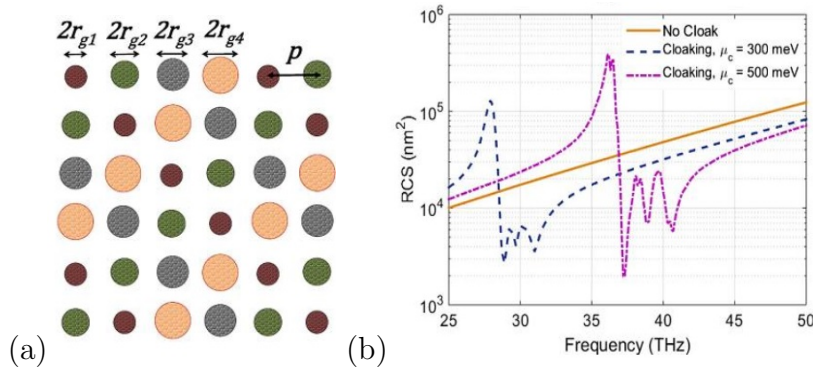
Figure 2.27: (a) the inhomogeneous metasurface consisting of graphene disks with different sizes, (b) RCS of uncloaked and cloaked cylinders [87].

ent elements′ size can be used. Figure 2.26(a) shows a dielectric cylinder covered by a homogeneous metasurface. Fig.2.26(b) illustrates RCS of the uncloaked and cloaked cylinders for two temperatures ($T = 100K$ and $T = 300K$ indicating one resonance frequency for cloaking purpose at 40 THz. Figure 2.27(a) shows an inhomogeneous metasurface consisting of graphene disks with different sizes and Fig. 2.27(b) shows the RCS of the uncloaked and cloaked cylinders. Additional resonances are observed by comparing Fig.2.26(b) and Fig. 2.27(b) resulting in broadband cloaking.

Chapter three

Graphene Based Metasurfaces

3.1   Introduction

Graphene as an ultrathin surface is modeled by a complex surface impedance tensor [88], [89]. Suppose a graphene layer in (x, y) place in the free space. Anisotropic model for conductivity of grapahene is expressed as [90]:

$$\sigma(\omega, \mu_c(E_0), \Gamma, T, B_0) = \hat{x}\hat{x}\ \sigma_{xx} + \hat{x}\hat{y}\ \sigma_{xy} + \hat{y}\hat{x}\ \sigma_{yx} + \hat{y}\hat{y}\ \sigma_{yy} \qquad (3.1)$$

where ω is the angular frequency, Γ is the scattering rate showing losss, T is the temperature, μ_c is the chemical potential, E_0 is electric bias and B_0 is the magnetic bias. Generally, scattering rate can be a function of frequency, temperature and field 's strength. Chemical potential relating to electrical charge density can be controlled by doping or applying bias voltage. Note that, in eq. 3.1, $\sigma_{xx} = \sigma_{yy}$ and $\sigma_{xy} = -\sigma_{yx}$. Therefore, it can be written as:

$$\sigma(\omega, \mu_c(E_0), \Gamma, T, B_0) = \sigma_d I + \sigma_0 J \qquad (3.2)$$

where σ_d and σ_0 are diagonal and off diagonal conductivities, respectively. $I = \hat{x}\hat{x} + \hat{y}\hat{y}$ and $J = \hat{x}\hat{y} - \hat{y}\hat{x}$ are symmetrical and asymmetrical diads, respectively. σ_d and σ_0 is obtained from Kubo formula [91]:

$$\sigma_d = -\frac{ie^2(\omega + 2i\Gamma)}{\pi\hbar^2}\left[\frac{1}{(\omega + 2i\Gamma)^2}\int_0^\infty \left(\frac{dn_f(\epsilon)}{d\epsilon} - \frac{dn_f(-\epsilon)}{d\epsilon}\right)\epsilon\,d\epsilon - \int_0^\infty \frac{n_f(-\epsilon) - n_f(\epsilon)}{(\omega + 2i\Gamma)^2 - 4(\frac{\epsilon}{\hbar})^2}d\epsilon\right]$$
$$(3.3)$$

$$\sigma_0 = -\frac{e^2 v_F^2 e B_0}{\pi\hbar^2}\left[\frac{1}{(\omega + 2i\Gamma)^2}\int_0^\infty \left(\frac{dn_f(\epsilon)}{d\epsilon} - \frac{dn_f(-\epsilon)}{d\epsilon}\right)\epsilon\,d\epsilon + \int_0^\infty \frac{1}{(\omega + 2i\Gamma)^2 - 4(\frac{\epsilon}{\hbar})^2}d\epsilon\right]$$
$$(3.4)$$

where $n_f(\epsilon) = \frac{1}{1+exp[(\epsilon-\mu_c)/(K_BT)]}$ is Fermi-Dirac distribution and $v_F = 10^6$ m/s is Fermi velocity.

In the following, it is supposed that there is no magnetic bias field ($B_0 = 0$). Therefore, according to eq. (3.4), asymmetrical conductivity terms will be omitted and symmetrical terms which are independent of magnetic bias will remain. So, graphene operates as an isotropic material.

In eq. (3.3), the first term relates to in-band contribution and the second term relates to out of band transition. The first term has analytically been obtained as follows [92]:

$$\sigma_{intra} = -j\frac{K_B e^2 T}{\pi\hbar^2(w - 2j\tau^{-1})}\left[\frac{\mu_c}{K_B T} + 2\ln(e^{-\frac{\mu_c}{K_B T}} + 1)\right] \qquad (3.5)$$

the formula has a Drude model form illustrating free electrons' behavior. K_B is the Boltzmann's constant and e is the electron charge.

The second term can not analytically be achieved, but if $K_B T << \mu_c$ and $K_B T << \hbar\omega$, an approximate expression has been obtained in [93] as follows:

$$\sigma_{inter} = \frac{je^2}{4\pi\hbar}\ln(\frac{2|\mu_c| - (w - j\tau^{-1})\hbar}{2|\mu_c| + (w - j\tau^{-1})\hbar}) \qquad (3.6)$$

Figures 3.1(a) and 3.1(b) show the real and imaginary parts of the conductivity of graphene versus frequency. Variation of the conductivity with frequency and chemical potential of graphene can be seen [94].
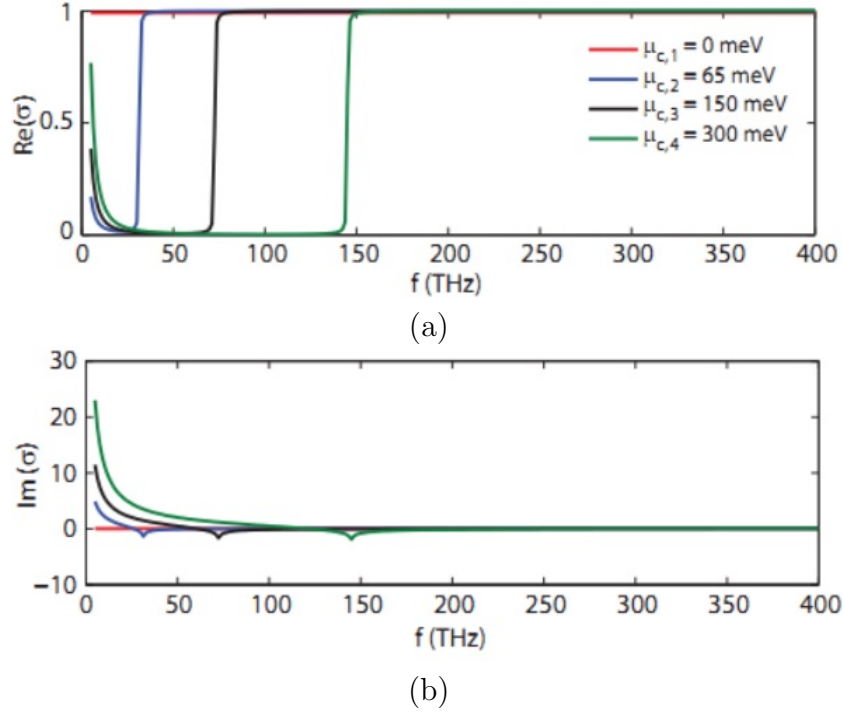
Figure 3.1: (a) Real part, (b) imaginary part of conductivity of graphene versus frequency [94].

3.2 Applications of graphene in metasurfaces

Excellent mechanical characteristics and controllable density of charge carriers in graphene, make it a good candidate for designing tunable and controllable metasurfaces. Graphene has a very controllable optical conductivity in terahertz and middle infrared frequencies. By changing the applied bias voltage of the graphene, surface conductivity and as a result, the permittivity of graphene can be adjusted. Resonance frequency of metasurfaces will be tuned with adjusting surface conductivity of the graphene [95].

In [96], a graphene metasurface was used for phase modulation. The structure of the considered metasurface is shown in Fig. 3.2(a) which consists of two dielectric layers (Si and Sio_2) and a square patch array of aluminum on the top of the substrates. A graphene layer is positioned on the patches. By changing the frequency, the conductivity of graphene will change leading to variation in the reflected phase of the metasurface. It can be understood from Fig. 3.2(b),
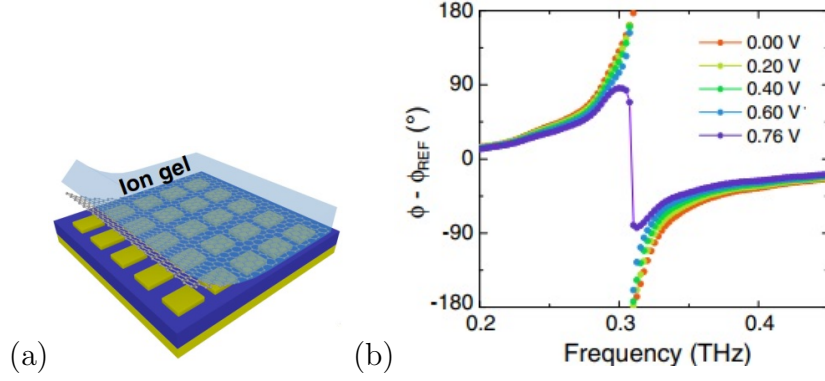
Figure 3.2: (a) Structure of a graphene metasurface for phase modulation, (b) Reflected phase of the metasurface versus frequency for different bias voltage [96].
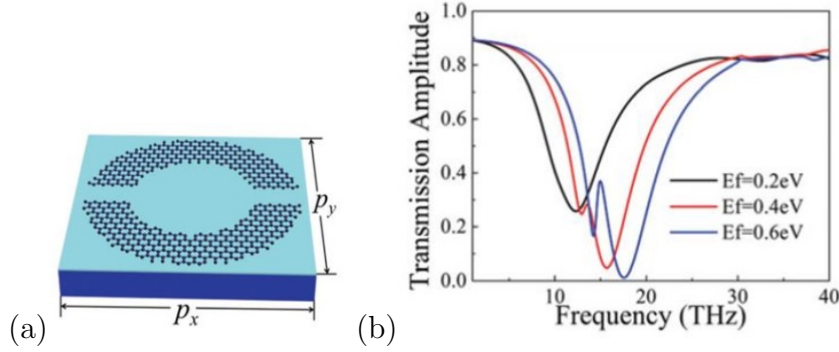
Figure 3.3: (a) Structure of a graphene metasurface consisting of split ring resonator, (b) Transmitted amplitude of the metasurface versus frequency for different Fermi levels [97].

that ± 180 degree-phase modulation has been achieved.

In [97], by putting an array of split ring resonators based on graphene as a metasurface on the top of dielectric substrates (Si and SiO_2), controllable transmitted wave has been achieved with different applied bias voltages. Figure 3.3(a) shows an element of the proposed metasurface. The amplitude of the transmitted wave versus frequency is shown in Fig.3.3(b) for different Fermi levels of graphene. It can be observed that by changing the Fermi level of the graphene, the resonance frequency and minimum transmitted amplitude will vary. The introduced metasurface has been designed for sensing applications.

In [98], controllable wave bending with the desired angle has been achieved using an anisotropic metasurface based on graphene. By changing the bias voltage applied to the graphene, the resonance frequency of the metasurface will change.
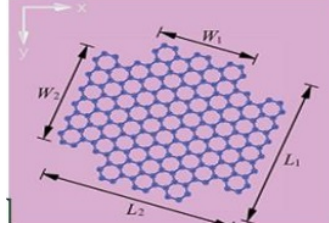
Figure 3.4: Anisotropic metasurface for wave refraction [98]

Therefore, different refraction of the electromagnetic wave can be achieved for different frequencies. Figure 3.4 shows the metasurface designed for wave refraction and Fig. 3.5(a) and Fig. 3.5(b) show transmitted bending waves for 14THz and 16THz, respectively. According to eq. (2.5), the bending angle is not the same for different frequencies. From Fig. 3.5(a) and Fig. 3.5(b), it can be seen that bending angle at 14THz is 49 degrees and at 16THz is 42.8 degrees.

In [99], an element of a metasurface consisting of gold and graphene patches has been designed as an absorber. Position of the gold and graphene patches and also the chemical potential of the graphene have been optimized to achieve maximum absorption bandwidth. Figure 3.6(a) shows the element of metasurface absorber and 3.6(b) illustrates the absorption curve versus frequency for different chemical potential of graphene. It indicates that for the optimized element, 1.95THz bandwidth has been achieved.

In [100], a nonreciprocal isolator has been designed, fabricated and tested using a metasurface based on graphene biased with a magnetic field. As mentioned in the introduction of this chapter, if graphene has a magnetic field bias, the off-diagonal elements of the conductivity matrix, will not be zero. For a right handed and left handed circularly polarized wave, conductivity of graphene is $\sigma_{cw} = \sigma_d + j\sigma_o$ and $\sigma_{ccw} = \sigma_d - j\sigma_o$, respectively. This conductivity difference for the right handed and left handed waves makes magnetized graphene a good choice for designing nonreciprocal devices for circular polarization.

Figure 3.7(a), shows the structure of the proposed nonreciprocal isolator based on a magnetized graphene for circularly polarized incident wave. Three graphene layers separated by polymethyl methacrylate are on Si substrate backed by a
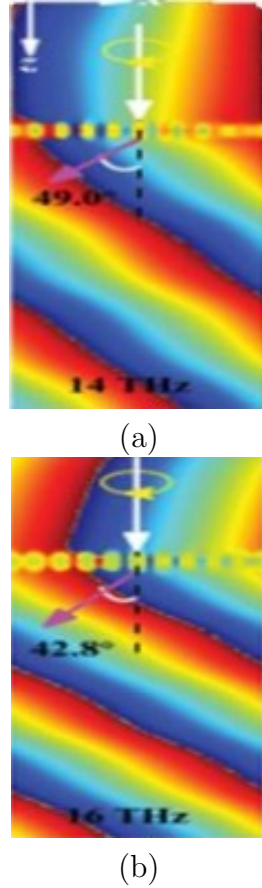
Figure 3.5: Transmitted bending wave at (a) 14THz and (b) 16THz [98].

ground plane. The goal of designing the metasurface illustrated in Figure 3.7(a) is that the right handed circularly polarized incident wave reflects as a left handed circularly polarized wave, while the left handed circularly polarized incident wave is absorbed by the metasurface and does not reflect. In this way, the structure operates as a nonreciprocal isolator. Figure 3.7(b) shows the reflection coefficient for both right handed and left handed circularly polarized impinging wave versus frequency. It can be noticed that at 2.9THz the left handed wave is reflected and the right handed wave is not reflected. At 7.8THz it is vice versa.

In [101], a metasurface consisting of two graphene layers and two dielectric layers for focusing the reflected wave at two frequencies has been introduced. The chemical potential of the graphene in each layer has been optimized to focus the reflected wave at the two desired frequencies. Figure 3.8 shows the dual layer
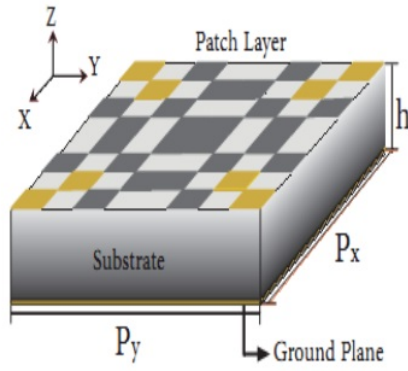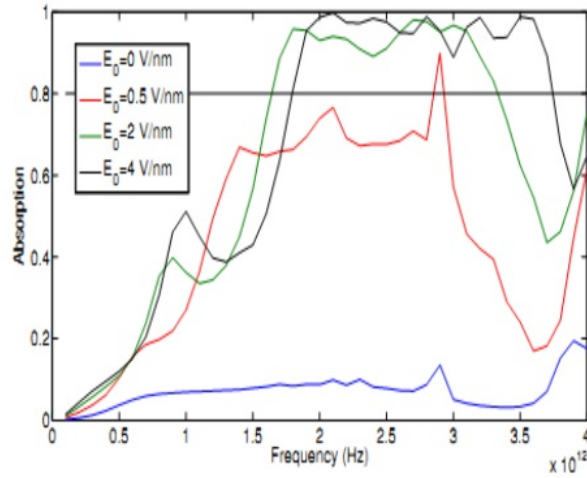
Figure 3.6: (a) An element of a metasurface with gold and graphene patch array on top of a substrate backed by a ground plane, (b) Absorption curves versus frequency for different Fermi levels [99].

metasurface. Figure 3.9 shows the amplitude and phase of the reflected wave versus size of graphene ribbons in the bottom layer at (a) 16THz and in the top layer at (b) 25THz. It indicates a well reflected amplitude for the considered size of the ribbons and 360 degrees reflected phase shift can be achieved. Figure 3.10 shows electric field distribution at (a) 16THz and (b) 25THz. It can be seen that the reflected wave has been focused at the two considered frequencies.
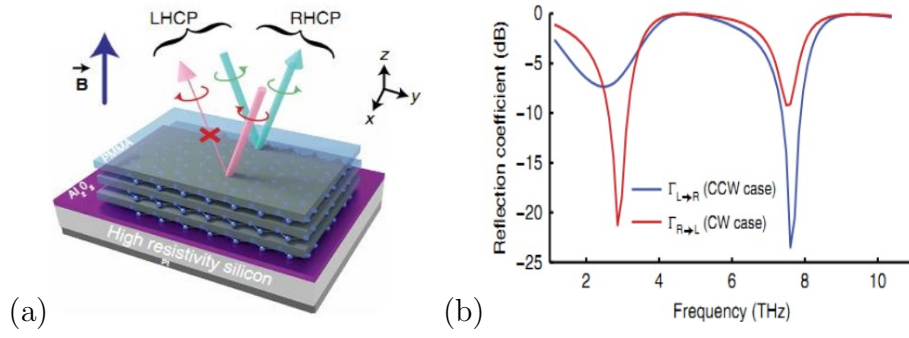
Figure 3.7: (a) Nonreciprocal metasurface element, (b) Reflection coefficient of circularly polarized waves [100].
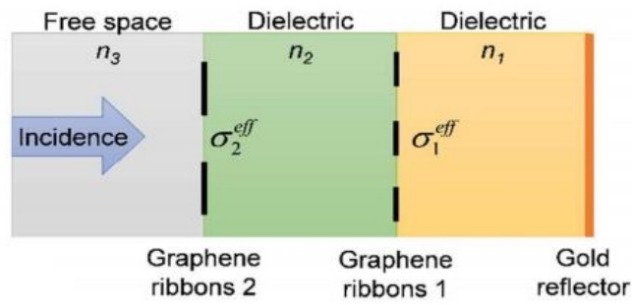
Figure 3.8: The structure of dual layer dual band metasurface lens [101]
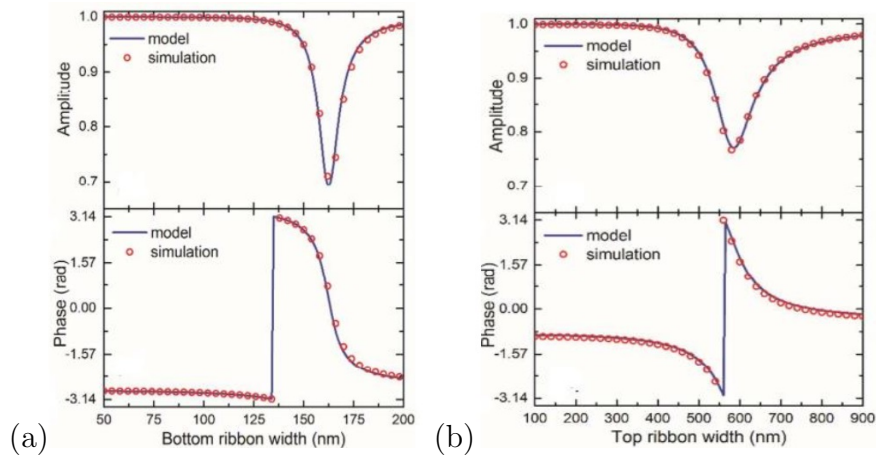
Figure 3.9: Amplitude and phase of the reflected wave versus the size of graphene ribbons in the bottom layer at (a)16THz and in the top layer at (b)25THz [101].
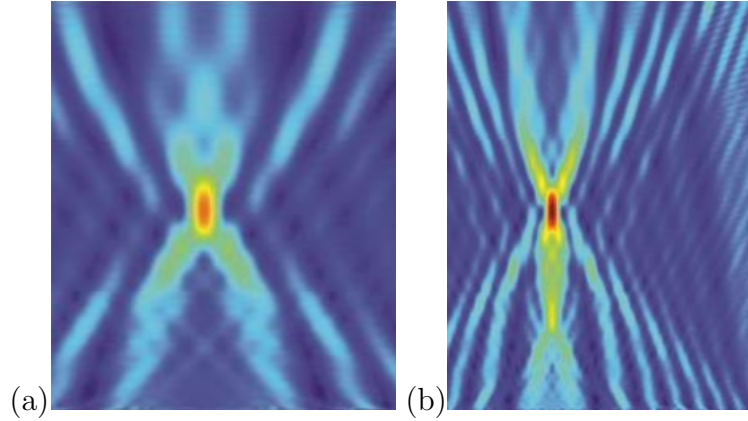
Figure 3.10: Electric field distribution at (a)16THz and (b)25THz [101].

In [102], the design of a sinusoidally modulated graphene based leaky-wave antenna with beam scanning capabilities at a fixed frequency has been proposed. The antenna is composed of a graphene sheet transferred onto a back-metalized substrate and a set of polysilicon DC gating pads located beneath it as shown in Fig. 3.11. In order to generate a leaky-mode, the graphene surface reactance is sinusoidally modulated via changing the surface impedance of the graphene by applying different DC bias voltages to the different gating pads. Figure 3.12, depicts the relationship between the bias voltage and the graphene reactance. Depending on the number of the pads, different scanning beam angles can be obtained. The main beam angle can be dynamically controlled by adjusting the applied bias voltages to the different pads. Figure 3.13 shows the radiation pattern of the designed leaky wave antenna at 2 THz for different numbers of the pads. It is proved that the radiation pattern of the antenna is able to scan a large angle at a fixed frequency.
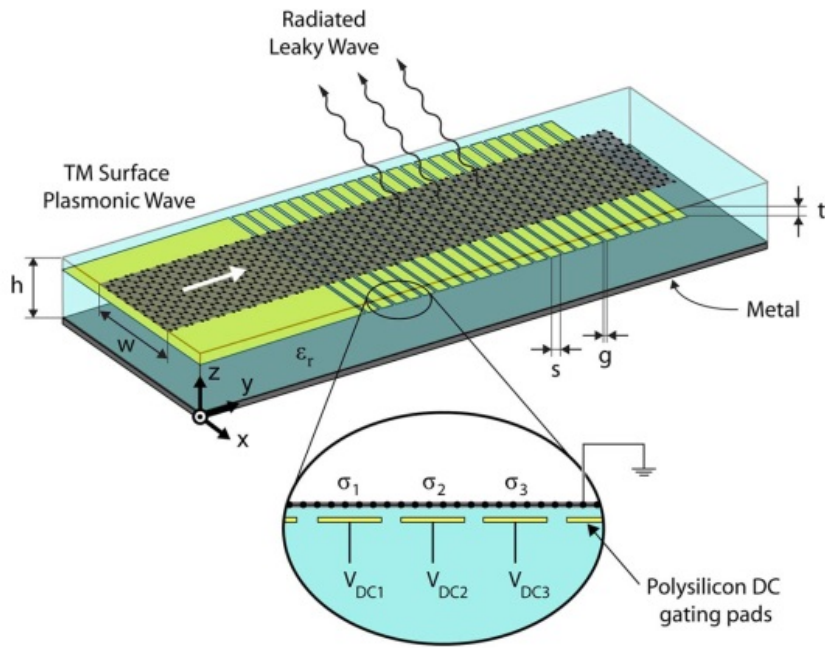
Figure 3.11:   The structure of sinusoidally modulated graphene based leaky-wave antenna [102].
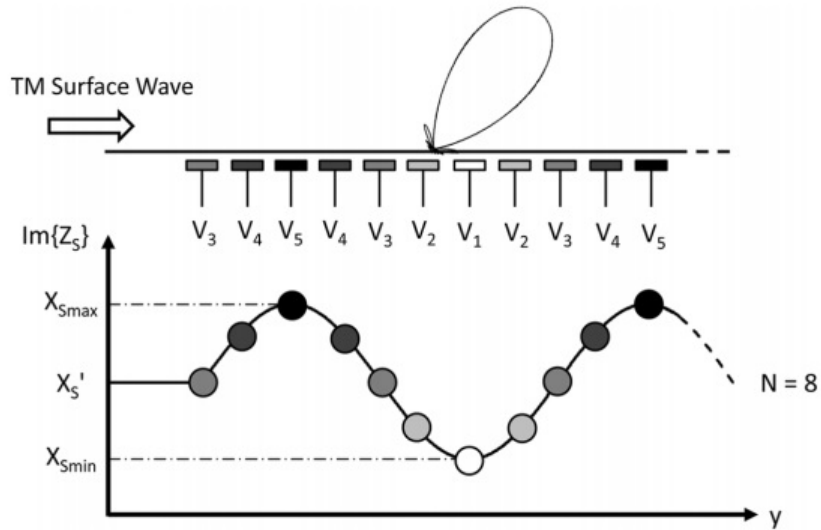
Figure 3.12:   Reactance of the graphene versus bias voltage [102].
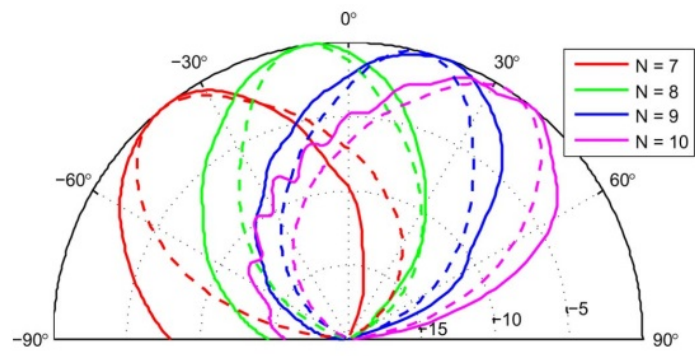
Figure 3.13:   The radiation pattern of the designed leaky wave antenna at 2 THz for different numbers of the pads [102].

Chapter four

Designing Graphene Based Metasurfaces for Scattering Manipulation of Electromagnetic Wave

4.1 Cloaking and scattering manipulation

4.1.1 Introduction

Cloaking has attracted great interest in recent years [68], [103]. Different techniques have been introduced to achieve cloaking such as transformation optics [20], [104], transmission line method [105], [106], carpet cloaking [107], [108] and plasmonic cloaking [109], [110]. Mantle cloaking based on the scattering cancellation method is one of the most important methods showing a remarkable performance and comfortable fabrication [111], [112]. In this method, the object is covered by a very thin metasurface which produces an anti phase field and therefore cancels the scattering from the object [113].

The majority of researches related to mantle cloaking has been carried out with consideration of a TM_z polarized normal incident plane wave as an incident wave. This is because the normal incidence situation is simpler than oblique one and TM_z polarized plane wave produces more scattering than TE_z polarized

wave, when illuminates on a cylinder [114]. However, in some applications the cylinder is exposed to an oblique incidence or a TE_z polarized impinging wave whose scattering can not be neglected. In section. 4.1.2, mantle cloaking of a dielectric cylinder under the illumination of TM_z polarized oblique incidence is investigated. There is no any closed form expression for the required surface impedance to achieve invisibility of a cylinder under the illumination for oblique incidence in the literature.

The required surface impedance to obtain this purpose for arbitrary incident angles is derived in this section. Graphene monolayer is utilized as a covering metasurface to realize the required surface impedance because of its tunability characteristics [115]. The analytical and simulation results related to finite and infinite cylinders agree very well. They show significant scattering reduction of the cylinders under illumination of oblique incident waves. Furthermore, it is illustrated that by adjusting the chemical potential of graphene, the designed graphene monolayer is able to cloak the considered cylinder for different desired incident angles. In section 4.1.2 dual polarized metasurface based mantle cloak is designed to cloak a dielectric cylinder under illumination of TE_z and TM_z polarized plane waves. Graphene strips are proposed to cover the cylinder. By optimizing the structure and graphene characteristics, a good reduction for radar cross section (RCS) of the cylinder illuminated by TE_z and TM_z and also circularly polarized plane wave is achieved. Tunable dual polarized mantle cloaking is obtained by adjusting the surface impedance of the graphene based metasurface with applying different bias voltages.

Other scattering manipulation of objects, can also be achieved by a metasurface. For example, the scattered field of a cylinder can be transformed into that of another cylinder by designing a metasurface with proper surface impedance. In section 4.1.3 it is supposed to transform the scattered field of a dielectric cylinder to one of another cylinder with the same material but different radius. This purpose can be achieved by covering the given cylinder with properly designed metasurface. The surface impedance of the metasurface is obtained by equating

45

the scattering coefficients of the covered and target cylinders. Scattering manipulation for a conducting cylinder can also be achieved with this method, but in this case, a dielectric layer should be placed between the conducting cylinder and the metasurface in order to avoid short circuit [?].

4.1.2 Mantle cloaking of dielectric cylinder under illumination of TM_z polarized oblique incidence

Oblique incidence assumption for obtaining the required surface impedance of the metasurface

Figure 4.1 shows a dielectric cylinder with radius a and relative permittivity of ϵ covered by a graphene metasurface. It is supposed that a TM_z polarized plane wave obliquely incidents to the cylinder with angle of θ_i relative to the z axes. The electric field of the incident field (E^i) can be written as follows:

$$E^i = E_0(\hat{x}\cos\theta_i + \hat{z}\sin\theta_i)e^{-j\beta_0(x\sin\theta_i - z\cos\theta_i)} \qquad (4.1)$$

For applying the first boundary condition (Continuity of tangential electric field) it is necessary to know the z component of the incident electric field, scattered electric field (E^s) and the electric field inside the cylinder (E^{in}). A plane wave can be expressed in terms of cylindrical wave functions using the relation which was derived in [83] as follows:

$$e^{-j\beta x} = \sum_{n=-\infty}^{\infty} j^{-n} J_n(\beta_0 r)e^{jn\phi} \qquad (4.2)$$

where J_n is Bessel function of the first kind. Therefore, (E_z^i) and (E_z^{in}) are written as the sum of infinite Bessel functions:

$$E_z^i = E_0 \sin\theta_i e^{(j\beta_0 z\cos\theta_i)} \sum_{n=-\infty}^{\infty} j^{-n} J_n(\beta_0 r\sin\theta_i)e^{jn\phi} \qquad (4.3)$$

46
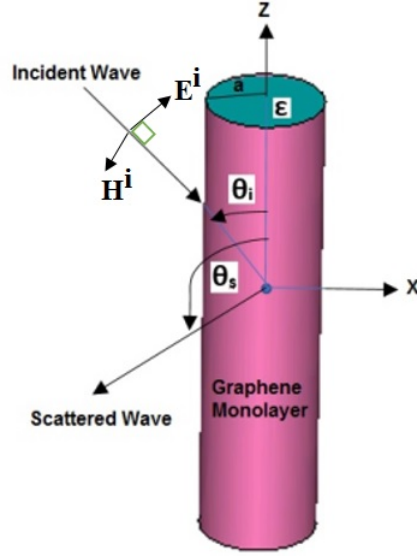
Figure 4.1:   Dielectric cylinder under illumination of oblique incidence.

$$E_z^{in} = E_0 \sin\theta_2 \; e^{(j\beta z \cos\theta_2)} \sum_{n=-\infty}^{\infty} j^{-n} a_n J_n(\beta r \sin\theta_2) e^{jn\phi} \qquad (4.4)$$

where θ_2 is the angle that the incident wave enters the cylinder. The z component of the scattered electric field (E^s) can be written as an infinite sum of Hankel functions [83].

$$E_z^s = E_0 \sin\theta_s \; e^{(-j\beta_0 z \cos\theta_s)} \sum_{n=-\infty}^{\infty} j^{-n} c_n H_n^{(2)}(\beta_0 r \sin\theta_s) e^{jn\phi} \qquad (4.5)$$

where β_0 and β are the propagation constants in the air and in the object. $H_n^{(2)}$ is Hankel function of the second type. a_n and c_n are unknown coefficients which can be determined by applying boundary conditions. The boundary condition related to the continuity of tangential electric field at the metasurface is:

$$E_z^i + E_z^s = E_z^{in} \text{ at r} = \text{a} \qquad (4.6)$$

which gives:

47

$$\sin\theta_i \sum_{n=-\infty}^{\infty} J_n(\beta_0 a\sin\theta_i) + \sin\theta_i \sum_{n=-\infty}^{\infty} c_n H_n^{(2)}(\beta_0 a\sin\theta_i) = \sin\theta_2 \sum_{n=-\infty}^{\infty} a_n J_n(\beta a\sin\theta_2)$$

$$(4.7)$$

phase matching gives:

$$\theta_s = \pi - \theta_i, \theta_2 = \sin^{-1}\sqrt{1 - (\frac{\beta_0}{\beta}\cos\theta_i)^2} \qquad (4.8)$$

The boundary condition which relates the tangential electric and magnetic fields to the surface impedance of the metasurface can be written in a tensorial form, as follows:

$$\hat{r} \times E^{in} = \overline{\overline{Z}}_s \hat{r} \times (H^i + H^s - H^{in}) = \overline{\overline{Z}}_s J_s \Big|_{r=a} \qquad (4.9)$$

where H denotes the magnetic field, J_s is the current density at the surface and $\overline{\overline{Z}}_s$ is the surface impedance tensor of the metasurface [114]. Equation 4.9 can be written as a matrix equation as follows:

$$\begin{bmatrix} Z_s^{zz} & Z_s^{z\phi} \\ Z_s^{\phi z} & Z_s^{\phi\phi} \end{bmatrix} \begin{bmatrix} J_z \\ J_\phi \end{bmatrix} = \begin{bmatrix} E_z \\ E_\phi \end{bmatrix} \qquad (4.10)$$

In the case of normal incidence, the electric field has just the z component, and by neglecting cross polarization coupling, the surface impedance (Z_s) can be considered as a scalar quantity while for oblique incidence the matrix equation (4.10) transforms into two scalar equations. The level of cross polarization coupling for oblique incidence is higher than that for normal incidence. However, utilizing a simple homogeneous metasurface, the cross polarized coupling can be reduced [116], and therefore the off-diagonal elements of the surface impedance matrix will be neglected, i.e. $Z_s^{z\phi} = Z_s^{\phi z} = 0$. As a consequence, matrix Eq. (4.10) will be expressed as two scalar equations as follows:

$$Z_s^{zz} J_z = E_z \tag{4.11}$$

and

$$Z_s^{\phi\phi} J_\phi = E_\phi \tag{4.12}$$

Equation (4.11) is similar to the boundary condition for normal incidence and the other equation is the result of supposing anisotropic metasurface. Both Z_s^{zz} and $Z_s^{\phi\phi}$ should be determined in order to design the metasurface for achieving the purpose of mantle cloaking of a dielectric cylinder under oblique illumination of TM_z polarized wave. Equation (4.11) leads to:

$$E_z^{in} = Z_s^{zz} \left(H_\phi^i + H_\phi^S - H_\phi^{in} \right) \tag{4.13}$$

With relation between E_z and H_ϕ [83]:

$$H_\phi = \frac{1}{jw\mu \sin_\theta^2} \frac{\partial E_z}{\partial r} \tag{4.14}$$

So eq. (4.11) results in:

$$\sin\theta_2 \sum_{n=-\infty}^{\infty} A_n J_n(\beta a \sin\theta_2) = \frac{Z_s^{zz}}{jw\mu} [\beta_0 \sum_{n=-\infty}^{\infty} J_n'(\beta_0 a \sin\theta_i) + \beta_0 \sum_{n=-\infty}^{\infty} C_n H_n'^{(2)}(\beta_0 a \sin\theta_s)$$

- $\beta \sum_{n=-\infty}^{\infty} A_n J_n'(\beta a \sin\theta_2)]$ (4.15)

On the other hand, eq. (4.12) gives:

$$E_\phi^{in} = Z_s^{\phi\phi} \left(H_z^i + H_z^s - H_z^{in} \right) \tag{4.16}$$

The z component of the magnetic field is zero because of assuming TM_z polarized incident wave (H_z=0). So, the right hand of eq. (4.16) is zero. The left side of the equation $E_\phi^{(in)}$ is:

$$E_\phi^{(in)} = jE_0 \frac{\cot\theta_2}{\beta r} e^{j\beta z \cos\theta_2} \sum_{n=-\infty}^{\infty} nj^{-n+1} a_n J_n(\beta r \sin\theta_2) e^{jn\phi} \tag{4.17}$$

Because mantle cloaking of a cylinder with small radius is under investigation ($\beta a \ll \lambda_0$), the first harmonic ($n = 0$) has much higher contribution in the scattered field of the cylinder than the others; therefore, higher order harmonics of the scattering field can be neglected [117]. For $n = 0$, it gives $E_\phi^{in} = 0$, so Eq. (4.16) is true for every $Z_s^{\phi\phi}$. For simplicity, it is considered that $Z_s^{\phi\phi}$ is equal to Z_s^{zz} indicating an isotropic metasurface, then we have:

$$Z_s^{\phi\phi} = Z_s^{zz} = Z_s \tag{4.18}$$

By solving Eqs. (4.7) and (4.15) the following matrix equation is obtained:

$$
\begin{bmatrix}
-\sin\theta_2 \sum J_n(\beta a \sin\theta_2) & \sin\theta_i \sum H_n^{(2)}(\beta_0 a \sin\theta_s) \\
\sin\theta_2 \sum J_n(\beta a \sin\theta_2) + \frac{Z_s}{j\omega\mu}\frac{\beta}{\sin\theta_2}\sum J_n'(\beta a \sin\theta_2) & -\frac{Z_s}{j\omega\mu}\frac{\beta_0}{\sin\theta_s}\sum H_n'^{(2)}(\beta_0 a \sin\theta_s)
\end{bmatrix}
\begin{bmatrix} a_n \\ c_n \end{bmatrix}
$$
$$
= \begin{bmatrix} -\sin\theta_i \sum J_n(\beta_0 a \sin\theta_i) \\ \frac{Z_s}{j\omega\mu}\frac{\beta_0}{\sin\theta_i}\sum J_n'(\beta_0 a \sin\theta_i) \end{bmatrix} \tag{4.19}
$$

and c_n is achieved by:

$$
c_n = \frac{\begin{vmatrix}
-\sin\theta_2 \sum J_n(\beta a \sin\theta_2) & -\sin\theta_i \sum J_n(\beta_0 a \sin\theta_i) \\
\sin\theta_2 \sum J_n(\beta a \sin\theta_2) + \frac{Z_s}{j\omega\mu}\frac{\beta}{\sin\theta_2}\sum J_n'(\beta a \sin\theta_2) & \frac{Z_s}{j\omega\mu}\frac{\beta_0}{\sin\theta_i}\sum J_n'(\beta_0 a \sin\theta_i)
\end{vmatrix}}{|A|}
$$
$$\tag{4.20}$$

where A is the 2×2 matrix in eq. (4.19). As it was mentioned, we investigate a small-radius cylinder so the first harmonic of the scattering field has the most important role in the scattered field. Therefore, by equating c_0 to 0, the scattering of the object will significantly be reduced. Equating c_0 to 0 Z_s is obtained as:

$$Z_s = \frac{j\eta_0 \sin\theta_i \sin\theta_2 J_0(\beta_0 a \sin\theta_i) J_0(\beta a \sin\theta_2)}{\sqrt{\epsilon_r}\sin\theta_i J_0(\beta_0 a \sin\theta_i) J_1(\beta a \sin\theta_2) - \sin\theta_2 J_0(\beta a \sin\theta_2) J_1(\beta_0 a \sin\theta_i)} \tag{4.21}$$

where η_0 is the intrinsic impedance of the air. The covering metasurface should have a surface impedance as calculated in eq. (4.21) to cloak a dielectric cylinder with dielectric constant of ϵ and radius of a which is obliquely illuminated by a TM_z polarized wave with incident angle of θ_i. Graphene monolayer is proposed as a covering metasurface to make the cylinder undetectable. The reason of choosing graphene metasurface is its simplicity. It is isotropic and homogeneous which leads to a lower cross polarization according to [109]. It is also tunable which means by applying different bias voltages it is possible to achieve tunable cloaking [91]. Kubo formula models the graphene conductivity which is a sum of interband and intraband terms [92]:

$$\sigma_{intra} = -j \frac{K_B e^2 T}{\pi \hbar^2 (w - 2j\tau^{-1})} \left(\frac{\mu_c}{K_B T} + 2\ln(e^{-\frac{\mu_c}{K_B T}} + 1) \right) \tag{4.22}$$

$$\sigma_{inter} = \frac{je^2}{4\pi\hbar} \ln \left(\frac{2|\mu_c| - (w - j\tau^{-1})\hbar}{2|\mu_c| + (w - j\tau^{-1})\hbar} \right) \tag{4.23}$$

where K_B is Boltzmanns constant, T is the temperature, e is the electron charge, μ_c is the chemical potential, τ is the relaxation time and $\hbar$ is the reduced Planks constant. Graphene characteristics should be chosen to achieve the required surface impedance.

Results and discussions

Infinite cylinder

Scattering width of a cylinder can be written as [1] [83]:

$$\sigma_{2-D} = \lim_{r \to \infty} 2\pi r \left(\frac{|H^s|^2}{|H^i|^2} \right) \tag{4.24}$$

the total SW will be achieved by the integral over the whole space angle which can be calculated calculated from the following equation [118]:

---

[1]We use H instead of E, because when $r \to \infty$ the magnetic field has just one component

$$\sigma_{2-D}(T) = \frac{1}{4\pi} \int \sigma_{2-D} \, d\Omega \tag{4.25}$$

The expression for the total SW $\sigma_{2-D}(T)$ of a cylinder which is illuminated by TM_z polarized oblique incidence is obtained as follows:

$$\sigma_{2-D}(T) = \frac{4}{\beta_0 \sin \theta_i} \sum_{n=-\infty}^{\infty} |c_n|^2 \tag{4.26}$$

It is supposed to cloak a dielectric cylinder with radius of $a = 15\mu$m and dielectric constant of $\epsilon = 4$ under illumination of a TM_z polarized plane wave. Two centre frequencies of 1 and 1.5 THz and two incident angles of 45° and 60° are investigated to show the tunability of the designed graphene metasurface regarding to frequency and incident angle. The radius of the cylinder at 1 THz is $\frac{\lambda_0}{20}$ which satisfies small radius condition required for the approximation used in analytical derivation. According to eq. (4.21) the required surface impedance for incident angle of 45° is 673j Ω at 1 THz and 449j Ω at 1.5 THz and for incident angle 60° is 692j Ω at 1 THz and 461j Ω at 1.5 THz. To achieve the required values for the surface impedance of graphene, its characteristics are chosen as: $\tau = 1$ ps, $T = 300$ K, μ_c for incident angle of 45° is 0.0775 eV at 1 THz and 0.179 eV at 1.5 THz and for incident angle of 60° is 0.0745 eV at 1 THz and 0.174 eV at 1.5 THz. Figure 4.2 shows analytical and numerical results for SW of uncloaked and cloaked cylinders obliquely illuminated by a TM_z polarized incidence wave with incident angles of 45° and 60°. Numerical results are achieved by simulation with CST Microwave Studio commercial software [119] and analytical results are obtained by applying (4.26). The result indicates a significant reduction of scattering of the covered cylinder with the designed graphene metasurface. Moreover, it can be concluded that by adjusting the chemical potential of graphene, cloaking will be achieved for different frequencies and different incident angles. It can also be seen that simulation results agree with analytical ones.

Figure 4.3 shows the SW reduction (the ratio of total SW of the coated cylinder to that of the bare cylinder) - in dB - for different incident angles at 1 THz.
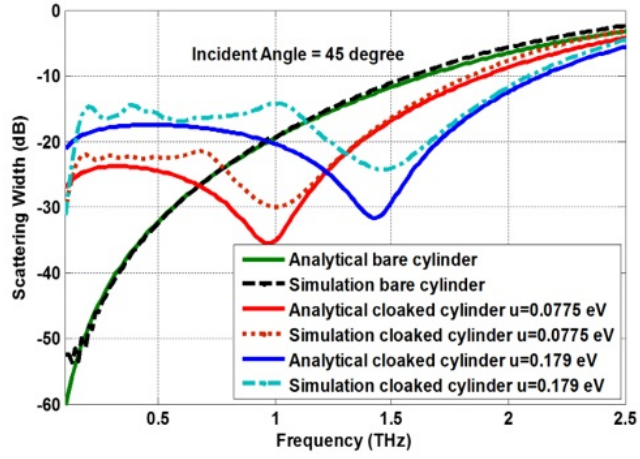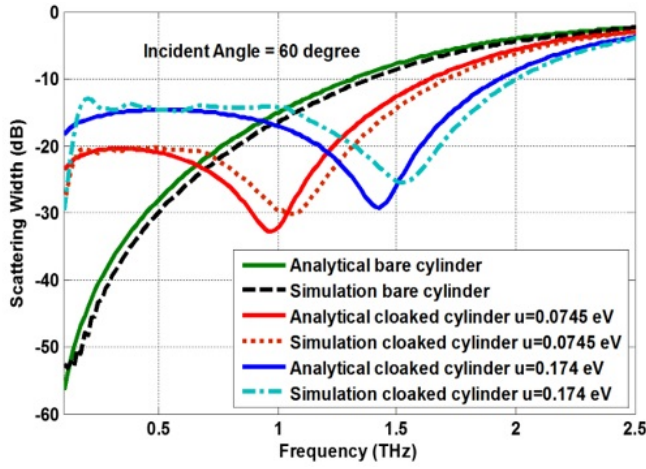
Figure 4.2: Scattering width of the bare and cloaked cylinders for the incident angle of (a) 45° and (b) 60°.

Looking at the curves in figure 4.3, it is understood that for incident angles near to the normal incidence 90°, the SW reduction is more than that for the smaller incident angles. The most important reason is the cross-polarized mutual coupling which has a higher level for the small incident angles. Comparison between Figs. 4.2(a) and 4.2(b) also proves this claim. For the incident angle of 60°, SW reduction from analytical and simulation calculations is almost the same, while for the incident angle of 45° there is about 6dB difference between analytical and simulation results. The reason is that in simulation, the mutual coupling is considered, however in the analytical formulation it is not. Another reason is neglecting E_ϕ^s for cylinders with small radii. In the formula of E_ϕ^s, there is a
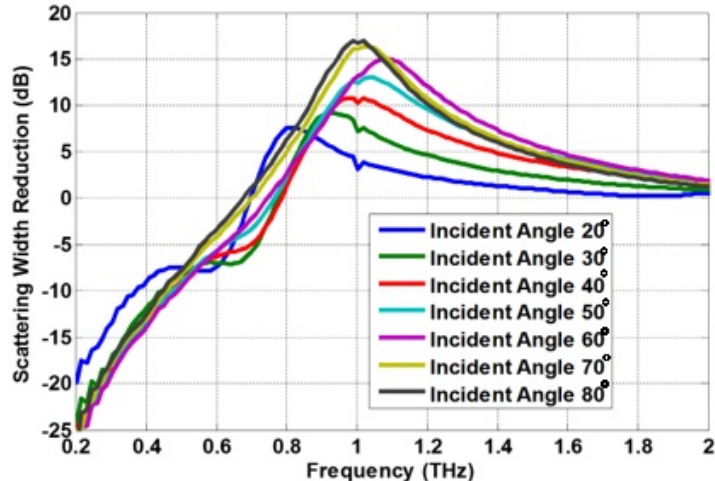
Figure 4.3: Scattering width reduction for different incident angles.

factor $\cot \theta_s$ as in E_ϕ^{in} in Eq. (4.17) which is higher for smaller angles. Therefore, considering this field as zero, has more effect on the accuracy of smaller angles.

It is worth noting that, the required surface impedances are purely imaginary, while graphene has some losses described by a small real part of the surface impedance. However, the real part is much smaller compared to the imaginary part. For instance, the surface impedance of the graphene at 1 THz to achieve invisibility for the incident angle of 45° is $(106.6 + j672.7)$ Ω. Increasing the relaxation time of the graphene leads to a lower loss and as a consequence, to a higher SW reduction [120]. But we continue our investigation with a relaxation time of 1 ps because of fabrication difficulties which raise with higher values of τ.

In [121], Foster's theorem has been referred which indicates that the reactance of any passive element will increase with frequency. However the required reactance of the covering metasurface to achieve cloaking of a dielectric cylinder decreases with frequency which results in a narrow bandwidth cloaking. In the above mentioned reference, non-foster dispersion has been realized using an active metasurface with lumped elements resulting in an invisibility with broad bandwidth.

Distribution of the electric fields for the uncloaked and cloaked cylinders with the radius of 30μm $(\lambda_0/10)$ is depicted in Fig. 4.4 for incident angles of 30° and
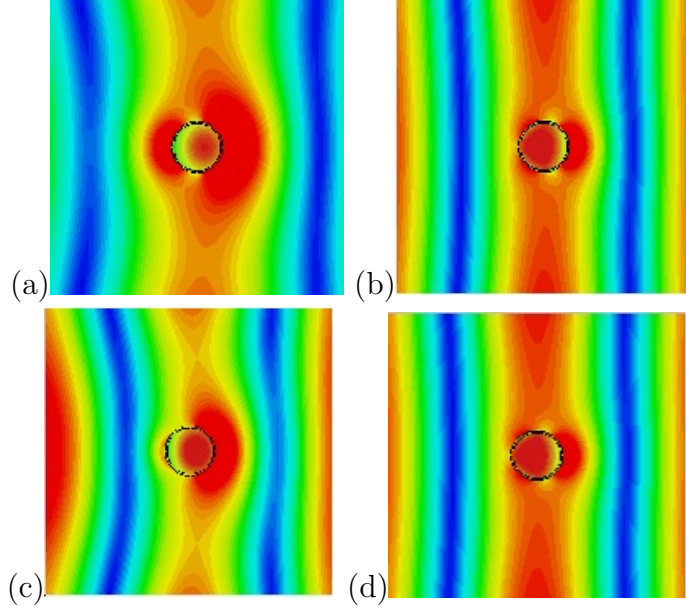
Figure 4.4: Electric field distribution for the (a) uncloaked and (b) cloaked cylinders with the incident angle of 30° and (c) uncloaked and (d) cloaked cylinders with the incident angle of 45°

45°. It indicates that the impinging plane wave passes the cloaked cylinder with very low perturbation while the incident wave will not remain a plane wave after passing the uncloaked cylinder.

Finite cylinder

The eq. (4.21) has been achieved for an infinite cylinder. However, it will be shown that the closed form expression can also be used for a finite cylinder by applying further optimization. In this section, a finite dielectric cylinder with height of $h = 240$ μm and radius of $a = 30\mu$m and $\epsilon = 4$ is investigated. The cylinder is obliquely illuminated by a TM_z polarized wave with the incident angle of 45° and 80°. The considered cylinder is covered with an optimized graphene monolayer to achieve invisibility for oblique incidence. There is not any exact formula for 3-D RCS in the literature, but in [83], [122], an approximate formula which relates the 3-D RCS to the 2-D SW is presented:

$$\sigma_{3-D} \simeq \sigma_{2-D} \frac{2h^2}{\lambda_0} \sin^2 \theta_i \qquad (4.27)$$

55
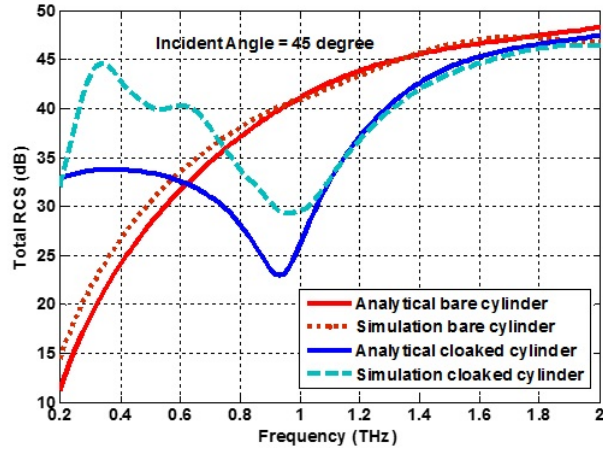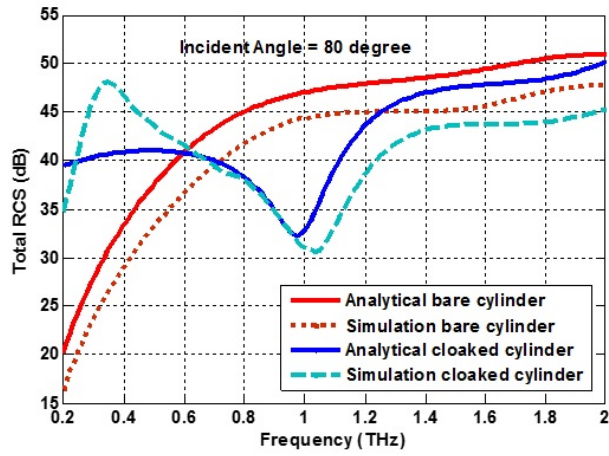
Figure 4.5: Total RCS of the bare and cloaked cylinders for the incident angle of (a) 45° and (b) 80°.

RCS of the uncloaked and cloaked cylinders under the illumination of oblique incidence with incident angles of 45° and 80° are calculated using eq. (4.27) and the analytical results are compared with the simulation results showing acceptable agreement. The results show a remarkable reduction in the total RCS of the cloaked cylinders. Far-field RCS of the covered and uncovered cylinders under oblique illumination of a TM_z polarized wave with incident angles of 45° and 80° are presented in the polar system in Fig. 4.6. It indicates the RCS reduction of the cloaked cylinder for the two considered incident angles for all observing angles. The results are obtained by simulation with CST Microwave Studio and HFSS [123]. The two results agree very well.
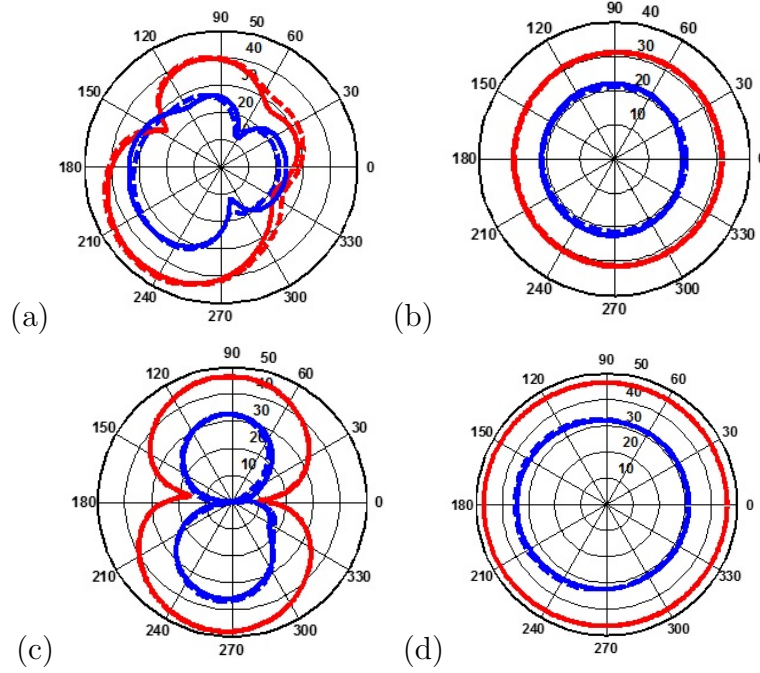
Figure 4.6: Far field results for the RCS of the cylinder with the incident angle of (a) and (b) 45° and (c) and (d) 80° in polar system for the observation angle of (a) and (c) constant $\phi = 0°$ and (b) constant $\theta = 45°$ and (d) constant $\theta = 80°$. Blue: Cloaked, Red: Uncloaked. Dashed line: CST, Solid line: HFSS

Another investigation has been done for a finite cylinder in this section. An array of inclined cylinders with the radius of 30 μm are placed in the aperture of a horn antenna. The cylinders scatter the wave inside the antenna which causes high reflection at the input of the horn antenna. This will also change the radiation pattern of the antenna. To reduce the antenna's blockage, The cylinders are cloaked with an optimized graphene metasurfaces. Figure 4.7 shows the amplitude of the reflection coefficient from the antenna in the presence of the cloaked and uncloaked cylinders. The cylinders have (a) 60° and (b) 80° slop in order to satisfy the oblique incidence condition. Huge reduction can be noticed in the reflection coefficient of the horn antenna in the presence of cloaked cylinders compared with uncloaked ones.
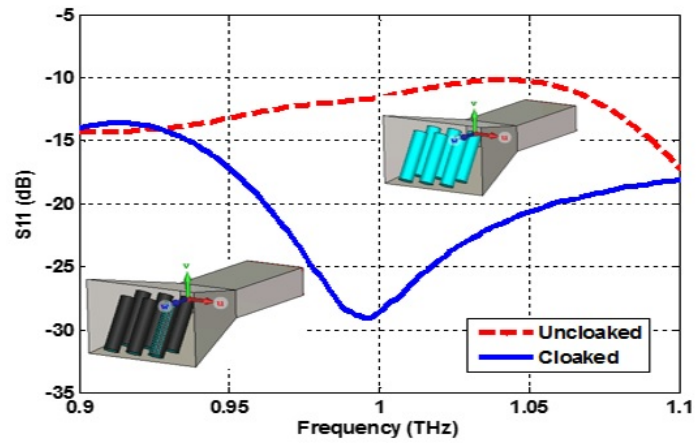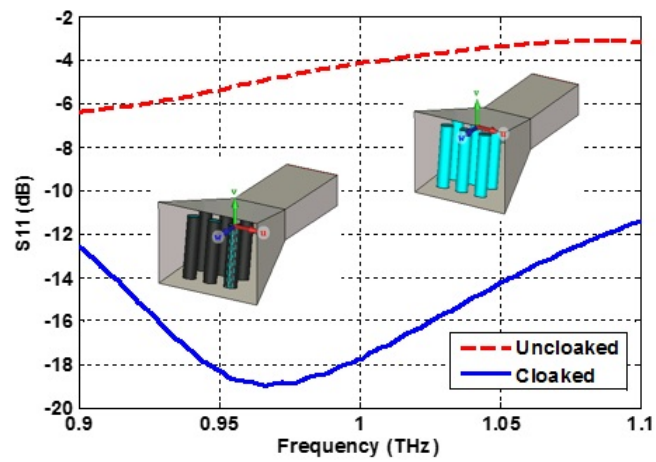
Figure 4.7: Reflection amplitude of the horn in the presence of uncloaked and cloaked cylinders with the slope of (a) 60° and (b) 80°

4.1.3 Designing a tunable dual polarized mantle cloaking utilizing graphene strips

A dielectric cylinder illuminated by TE and TM polarized plane waves is shown in Fig. 4.8. The goal is to design a tunable dual polarized mantle cloak based on a graphene-strips metasurface. The tangential electric and magnetic fields for the two considered polarizations are written as below:

$$E_i = \hat{z} \ E_0 \ \sum_{n=-\infty}^{\infty} j^{-n} J_n(\beta_0 r) \ e^{jn\phi} \tag{4.28}$$

$$E_s = \hat{z} \ E_0 \ \sum_{n=-\infty}^{\infty} j^{-n} \ c_{n(TM)} \ H_n^{(2)}(\beta_0 r) \ e^{jn\phi} \tag{4.29}$$

$$E_{in} = \hat{z} \ E_0 \ \sum_{n=-\infty}^{\infty} j^{-n} \ a_{n(TM)} \ J_n(\beta r) \ e^{jn\phi} \tag{4.30}$$

$$H_i = \hat{z} \ H_0 \ \sum_{n=-\infty}^{\infty} j^{-n} J_n(\beta_0 r) \ e^{jn\phi} \tag{4.31}$$

$$H_s = \hat{z} \ H_0 \ \sum_{n=-\infty}^{\infty} j^{-n} \ c_{n(TE)} \ H_n^{(2)}(\beta_0 r) \ e^{jn\phi} \tag{4.32}$$

$$H_{in} = \hat{z} \ H_0 \ \sum_{n=-\infty}^{\infty} j^{-n} \ a_{n(TE)} \ J_n(\beta r) \ e^{jn\phi} \tag{4.33}$$

where J_n and $H_n^{(2)}$ are Bessel function of the first type and Hankel function of the second type. β_0 and β are wave numbers in free space and in the cylinder. Subscripts i, s and in represent incident, scattered and the field inside the object, respectively. The relationships between electric and magnetic fields are [83]:

$$H_{\phi(TM)} = \frac{1}{jw\mu} \frac{\partial E_{z(TM)}}{\partial r} \tag{4.34}$$

$$E_{\phi(TE)} = -\frac{1}{jw\epsilon} \frac{\partial H_{z(TE)}}{\partial r} \tag{4.35}$$
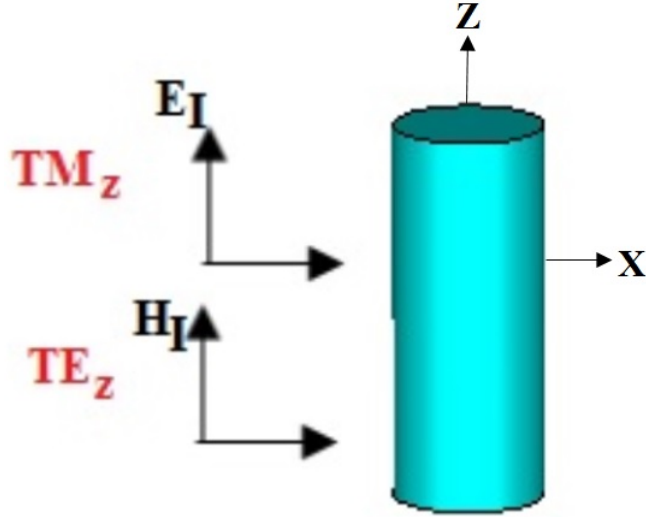
Figure 4.8: Dielectric cylinder under TE and TM polarized illumination of incident waves

By applying boundary conditions, scattering coefficients for the TE polarization $c_{n(TE)}$ and for the TM polarization $c_{n(TM)}$ can be achieved.

In [44], it was shown that different surface impedances are required to achieve invisibility for simultaneous TE and TM polarizations, therefore an isotropic metasurface is not able to cloak a dielectric cylinder for both polarizations. Instead, an anisotropic metasurface should cover the cylinder so that it is possible to design the surface impedance for each direction, independently. A tunable anisotropic metasurface based on graphene strips is proposed to achieve the tunable dual polarized cloaking for the dielectric cylinder. Figure 4.9 shows the structure of the introduced metasurface. Tensorial surface impedance for the considered metasurface is [124]:

$$z_{zz} = z_s \, \frac{p}{a} \tag{4.36}$$

$$z_{xx} = z_s \, \frac{a}{p} + \frac{g}{p \, \sigma_c} \tag{4.37}$$

$$\sigma_c = \frac{j\omega\epsilon_0 p}{\pi} \, \ln\csc(\frac{\pi g}{2p}) \tag{4.38}$$

60
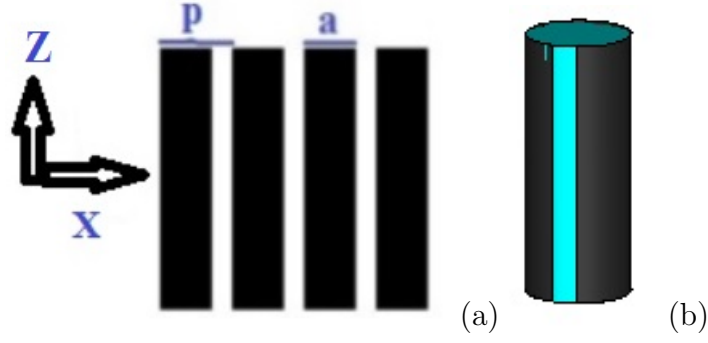
Figure 4.9: (a) Structure of graphene strips, (b) A dielectric cylinder coated by graphene strips.

where p and a are periodicity and width of the strips, respectively, $g = p - a$ is the gap distance between two strips and z_s is the surface impedance of graphene. The conductivity of graphene has been modeled by Kubo formula [92], which is the sum of *intra* and *inter* parts.

Designing the considered metasurface includes the following steps:

1. Calculating the required surface impedance of the covering metasurface for cloaking a dielectric cylinder which is normally illuminated by a TM_z polarized wave (z_{zz}) from eq. (4.39) [76]:

$$z_{zz} = \frac{2}{\omega a_1 \epsilon_0 (\epsilon_r - 1)} \tag{4.39}$$

where a_1 and ϵ_r are radius and dielectric constant of the cylinder, respectively.

2. Obtaining the required surface impedance of the metasurface for cloaking a dielectric cylinder illuminated by TE_z polarized wave (z_{xx}). Since closed form expression for the required surface impedance has not been achieved in the literature, this should be obtained by optimization.

3. Choosing the characteristics of graphene and calculating its surface impedance (z_s).

4. Using eq. (4.36) to calculate the ratio of p/a.

5. Calculating σ_c using eq. (4.38).

6. The periodicity of the strips (p) can be calculated using eq. (4.37) and by knowing the ratio of p/a, strip width (a) will be obtained.

61
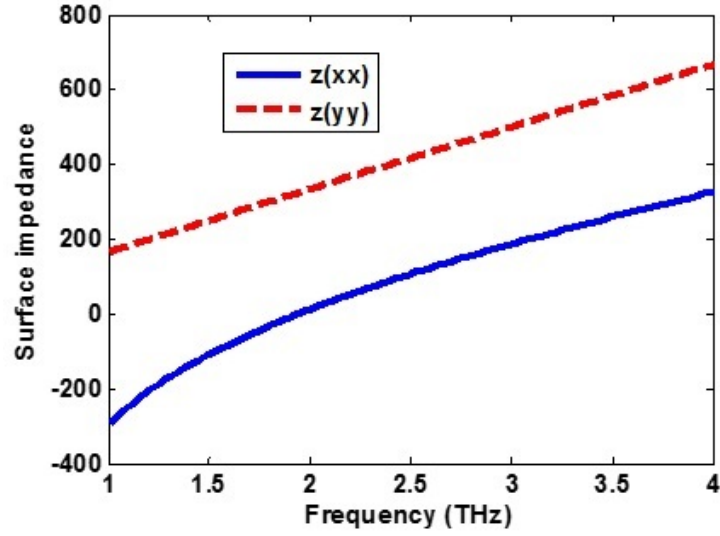
Figure 4.10: The surface impedance tensor elements z_{xx} and z_{zz} for the optimized parameters of the proposed structure.

The anisotropic metasurface has been designed to cloak a dielectric cylinder with dielectric constant of $\epsilon_r = 4$ and radius of $a_1 = 10\mu$m under the illumination of TE and TM polarized plane waves at $f_r = 2.5$THz. The obtained required surface impedance for TE and TM polarizations are as follows: $z_{xx} = 234$ jΩ and $z_{zz} = 404$ jΩ. The characteristics of graphene are chosen as follows: $T = 300$K, $\tau = 1$ps and $\mu_c = 0.4$eV which results in a graphene surface impedance of $z_s = j333.7\Omega$. According to the proposed procedure, $p=24\mu$m and $a=19.2\mu$m are obtained. The number of strips which cover the cylinder should be integer so further optimization is needed for this design. Optimized z_{xx} and z_{zz} are plotted in Fig. 4.10. They indicate that the required values are achieved with this structure at 2.5THz.

RCSs of the bare and coated cylinders are shown in Fig. 4.11 which indicates a simultaneous scattering decrease for both TM and TE polarizations at 2.5THz. It can also be observed that the level of scattering reduction for the incident wave with TM_z polarization is much more than that of the TE_z polarization. According to [114], the scattering coefficient of the first harmonic is much larger than that of the other of harmonics and by equating it to zero, a great RCS decrease will be achieved, while for the TE polarization, the three first harmonics have the same
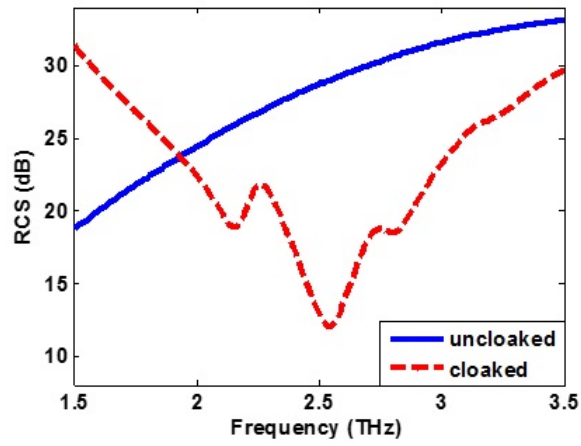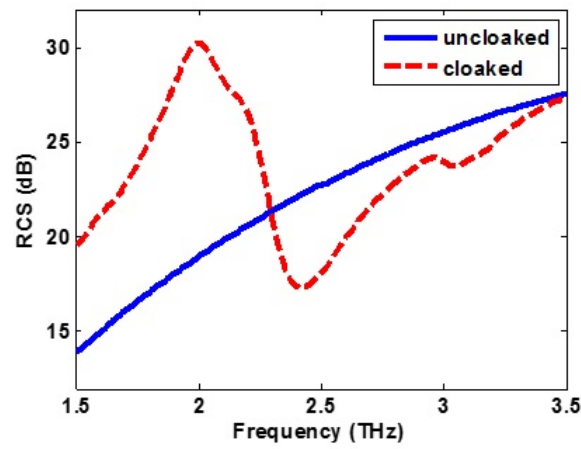
Figure 4.11: RCS of uncloaked and cloaked cylinders with anisotropic metasurface for (a) TM polarized incident wave and (b) TE polarized incident wave.
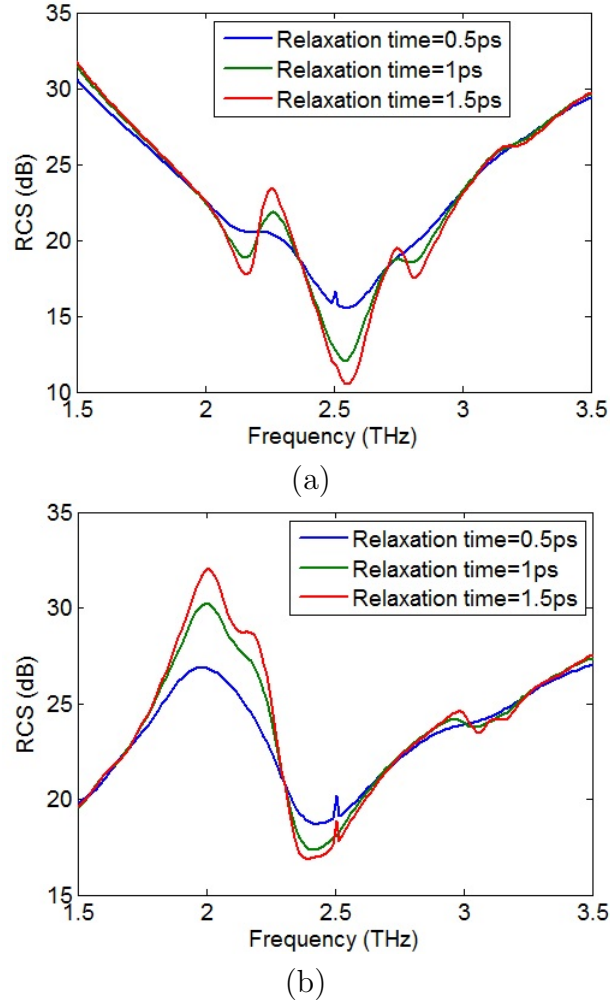
Figure 4.12: RCS of the cloaked cylinders for different amounts of the relaxation time of graphene for (a) TM, (b) TE polarizations.

order of magnitude.

Effect of the relaxation time of graphene on the cloaking performance has been studied. Figure 4.12 shows the RCS of the cloaked cylinder for different relaxation times of graphene for TE and TM polarizations. It reveals that higher relaxation time results in better cloaking performance and lower RCS of the cylinder for both polarizations. The reason is that higher relaxation time leads to lower loss of graphene.

Figure 4.13 shows that by adjusting the chemical potential of graphene, cloaking frequency can be tuned. It is illustrated that by changing the chemical potential to 0.25eV and 0.55eV the cloaking frequency shifts to 2.1THz and 2.8THz,
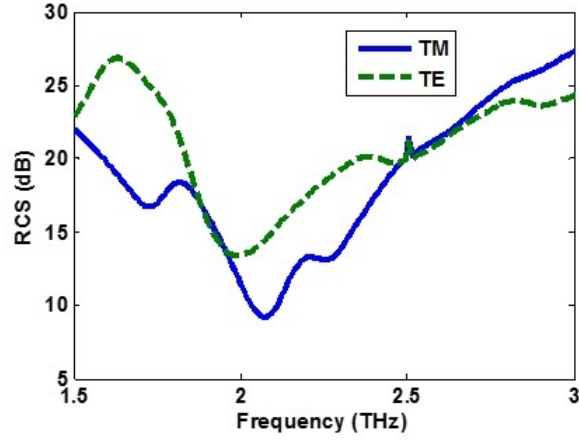
(a)
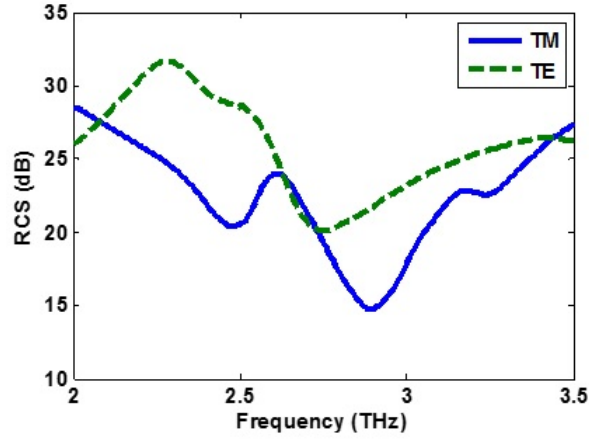
(b)

Figure 4.13: RCS of uncloaked and cloaked cylinders with anisotropic metasurface for TM and TE polarizations with the chemical potential of (a) 0.25eV and (b) 0.55eV.

respectively. Figure 4.14 shows electric field distribution for the uncloaked and cloaked cylinders under illumination of TE and TM polarized plane waves. It can be seen that for both polarizations, the plane wave passes the cloaked cylinders with a small perturbation. Figure 4.15 shows distribution of the electric field at 2.1THz and 2.8THz for cloaked cylinders under illumination of TE and TM polarizations. It indicates that the incident waves can be considered as plane waves after passing the cylinders which means the scattering from the cylinders can be neglected at these frequencies.

RCS results in polar system for TM polarization in $\phi = 0°$ plane and TE polarization in $\theta = 0°$ plane obtained by CST and HFSS are shown in Fig. 4.16.

65
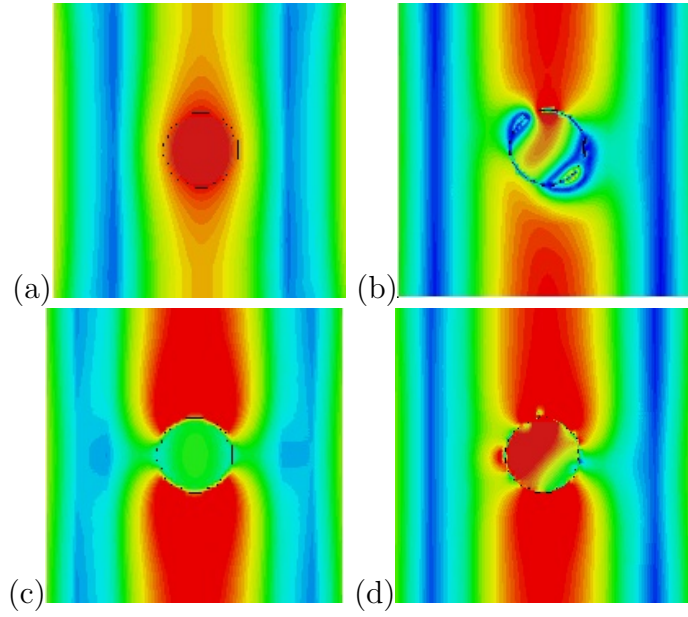
Figure 4.14: Electric field distribution for the (a) uncloaked and (b) cloaked cylinders for TM polarization and (c) uncloaked and (d) cloaked cylinders for TE polarization.
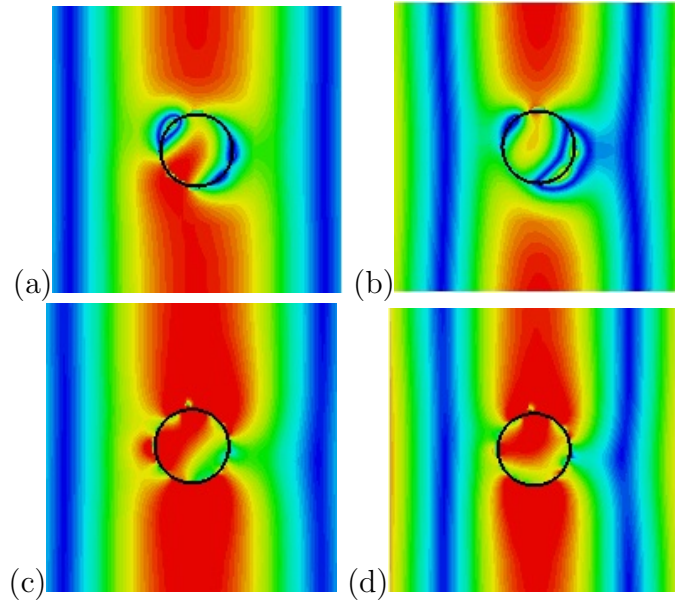
Figure 4.15: Electric field distribution for the cloaked cylinders for (a) and (b) TM polarization, (c) and (d) TE polarization. (a) and (c) at 2.1THz, (b) and (d) at 2.8THz.
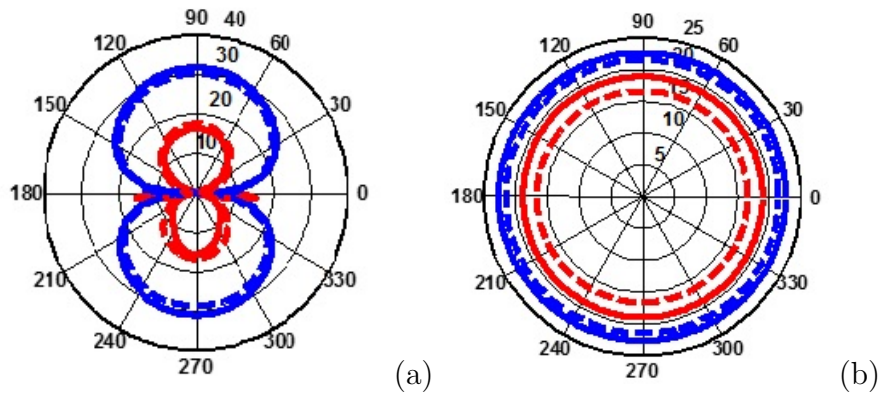
Figure 4.16:   Polar plot of RCS related to cloaked and uncloaked cylinders for (a) TM polarized incident wave in $\phi = 0°$ plane and for (b) TE polarized incident wave in $\theta = 0°$ plane. Blue: uncloaked, Red: cloaked, Dashed line: CST, Solid line: HFSS.
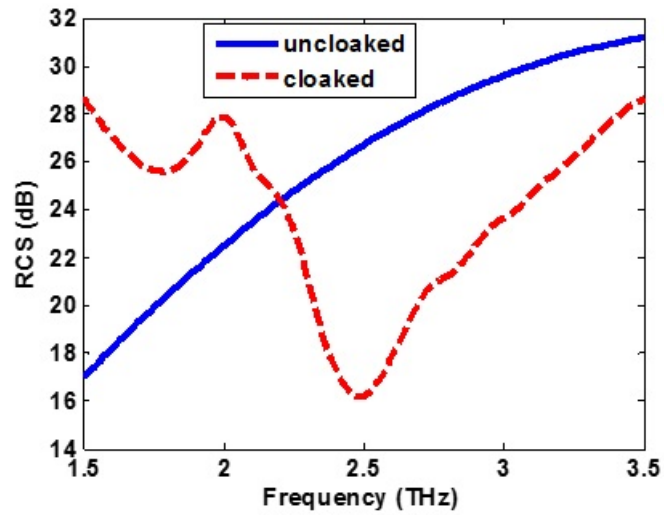
Figure 4.17:   RCS of cloaked and uncloaked cylinders under illumination of circular polarized waves.

67
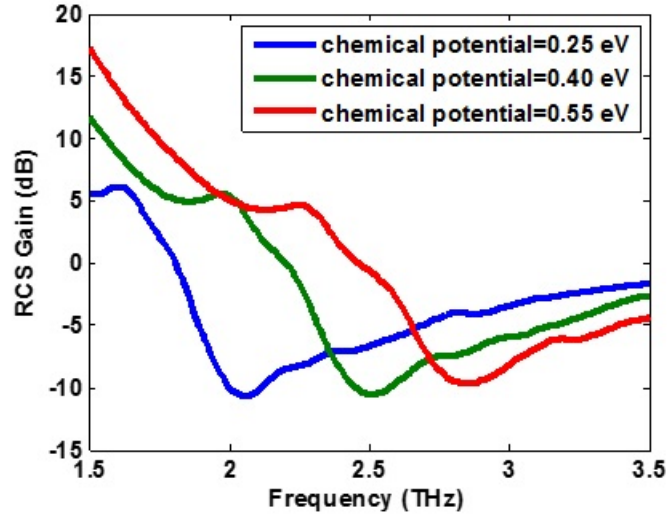
Figure 4.18: RCS of cloaked and uncloaked cylinders under the illumination of circularly polarized waves.

It illustrates the RCS reduction for every observation angle in both polarizations. Furthermore, good agreement is observed between CST and HFSS results.

Figure 4.17 shows the RCS reduction of the cloaked cylinder at 2.5THz under the illumination of a circularly polarized incident wave which is a combination of TE and TM polarized waves. Figure 4.18 depicts the tunability of the designed mantle cloak for circular polarization.

4.1.4 Scattering manipulation of dielectric and conducting cylinders under illumination of TM_z polarized plane waves

The analytical Investigation of the problem for a dielectric cylinder

Our goal is to transform the scattering property of a dielectric cylinder by covering it with a properly designed metasurface, to one of another dielectric cylinder with the same dielectric constant but different radius. Figure 4.19 shows the principle of the considered goal. The given dielectric cylinder, the covered one and target one are shown in Fig. 4.19(a), (b) and (c), respectively. The cylinders are illuminated by a plane wave with TM_z polarization. For tunability purposes, graphene

68
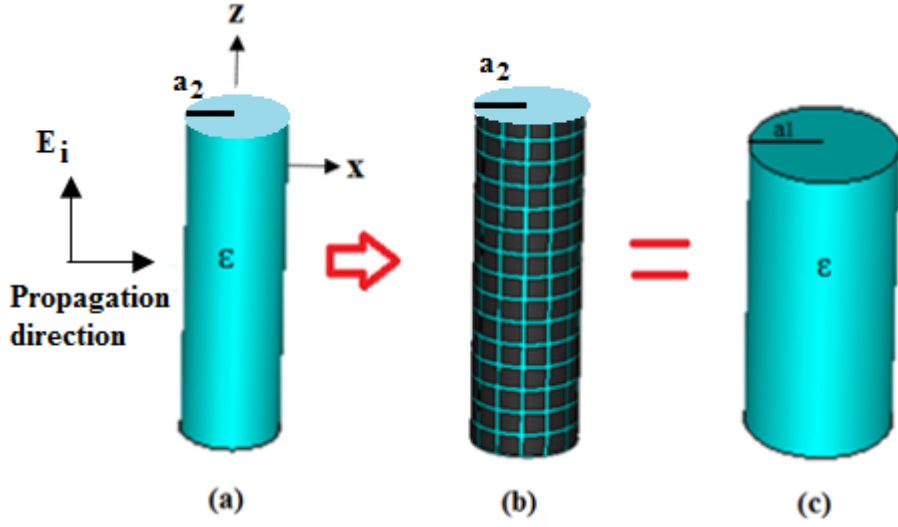
Figure 4.19: Structures of (a) given, (b) coated and (c) target dielectric cylinders.

is considered as the covering metasurface. However, a graphene monolayer can not satisfy the considered goal, because as it will be shown, for achieving this purpose, both inductive and capacitive surface reactances are needed, while graphene is inductive in THz regime. Therefore, a nanostructured graphene metasurface is considered to cover the cylinder to achieve scattering manipulation, as its surface reactance has both inductive and capacitive [84]. The scattering width of the covered cylinder should be equal to that of the target one in order to have the same scattering properties.

In the first step, the target cylinder with a radius of $a_2 = 7\mu$m under illumination of a TM_z polarized plane wave is investigated. The electric field of the incident wave can be written as follows:

$$E_i = \hat{z} \ E_0 \ \sum_{n=-\infty}^{\infty} j^{-n} J_n(\beta_0 r) \ e^{jn\phi} \tag{4.40}$$

The scattered field is written as:

$$E_s = \hat{z} \ E_0 \ \sum_{n=-\infty}^{\infty} j^{-n} \ c_n \ H_n^{(2)}(\beta_0 r) \ e^{jn\phi} \tag{4.41}$$

The electric field inside the object is expressed as:

$$E_{in} = \hat{z} \, E_0 \sum_{n=-\infty}^{\infty} j^{-n} \, a_n \, J_n(\beta r) \, e^{jn\phi} \tag{4.42}$$

The continuity of tangential electric and magnetic fields is applied at $r = a_1$.

$$E_z^1 = E_z^2 \tag{4.43}$$

$$H_\phi^1 = H_\phi^2 \tag{4.44}$$

where apex 1 and 2 correspond to the air and the cylinder, respectively. Scattered electric field and the electric field inside the cylinder for the covered cylinder with the radius of $r = a_2$ are the same as (4.41) and (4.42) but with a'_n and c'_n coefficients. The boundary condition of tangential electric field's continuity and tangential magnetic field's discontinuity as the result of assuming the covering metasurface is applied at $r = a_2$.

$$E_z^1 = E_z^2 \tag{4.45}$$

$$Z_s \, (H_\phi^1 - H_\phi^2) = E_z \tag{4.46}$$

where Z_s is the surface impedance of the nanostructured graphene metasurface. By solving the boundary condition equations, scattering coefficients for the target cylinder (c_n) and for the coated cylinder (c'_n) is obtained as :

$$c_n = \frac{J_n(\beta a_1)J'_n((\beta_0 a_1) - \sqrt{\epsilon}J_n(\beta_0 a_1)J'_n((\beta a_1)}{\sqrt{\epsilon}J'_n(\beta a_1)H_n^{(2)}(\beta_0 a_1) - J_n(\beta a_1)H_n^{(2)'}((\beta_0 a_1)} \tag{4.47}$$

$$c'_n = \frac{\frac{Z_s}{j\eta_0}J_n(\beta a_2)J'_n(\beta_0 a_2) - J_n(\beta_0 a_2)(J_n(\beta a_2) + \frac{Z_s}{j\eta}J'_n(\beta a_2))}{-\frac{Z_s}{j\eta_0}J_n(\beta a_2)H_n^{(2)'}(\beta_0 a_2) + H_n^{(2)}(\beta_0 a_2)(J_n(\beta a_2) + \frac{Z_s}{j\eta}J'_n((\beta a_2))} \tag{4.48}$$

where η_0 and η represent the Intrinsic impedances in the air and in the cylinder. It is assumed that the cylinders have small radius so the scattering coefficient of the first harmonic is much larger than that of the others.

the scattering coefficients for the first harmonic are achieved as follows:

$$c_0 = j \frac{\pi(\beta_0 a_1)^2 (1 - \epsilon)}{2\epsilon(\beta_0 a_1)^2 ln(\beta_0 a_1) + 4} \tag{4.49}$$

$$c_0' = \frac{\pi(w Z_s \epsilon_0 (\epsilon - 1) - 2j)}{\frac{4jZ_s}{\omega\mu a_2} + 4\ln(\beta_0 a_2) + 2jZ_s\omega\epsilon_0\epsilon a_2 \ln(\beta_0 a_2)} \tag{4.50}$$

Therefore to transform the SW of a cylinder to one of another it is enough to equate c_0 to $c_0\prime$. By solving this equation, the required surface impedance to achieve scattering manipulation for the dielectric cylinder is obtained as follows:

$$Z_s = j \frac{-2\omega\mu a_2[(\beta_0 a_1)^2(\epsilon \ln\left(\frac{a_1}{a_2}\right) + \ln(\beta_0 a_2)) + 2]}{\beta_0^2(1 - \epsilon)[\epsilon a_1^2 a_2^2 \beta_0^2 \ln\left(\frac{a_1}{a_2}\right) + 2(a_2^2 - a_1^2)]} \tag{4.51}$$

The analytical Investigation of the problem for a conducting cylinder

A conducting cylinder with a radius a_2 under the illumination of a TM_z polarized plane wave is shown in Fig. 4.20(a). The goal is to transform its SW to that of another cylinder with a radius of a_1 as shown in Fig. 4.20(b). The purpose can be achieved by covering the cylinder with a dielectric layer with the radius of a_c and a metasurface illustrated in Fig. 4.20(c). For the target cylinder, the electric field for the incident and scattered waves are the same as equations (4.40) and (4.41). For the covered cylinders, these fields are the same but electric field inside the dielectric layer is :

$$E_{in} = \hat{z} \ E_0 \sum_{n=-\infty}^{\infty} j^{-n} \left(a_n' \ J_n(\beta r) + b_n' \ Y_n(\beta r)\right) e^{jn\phi} \tag{4.52}$$

where J_n and Y_n are the Bessel functions of the first and second kind. By applying boundary conditions at $r = a_1$ for the target cylinder and at $r = a_c$ for the coated cylinders, the scattering coefficients for the two cylinders will be achieved as follows:

$$c_n = \frac{-J_n(\beta_0 a_1)}{H_n^{(2)}(\beta_0 a_1)} \tag{4.53}$$
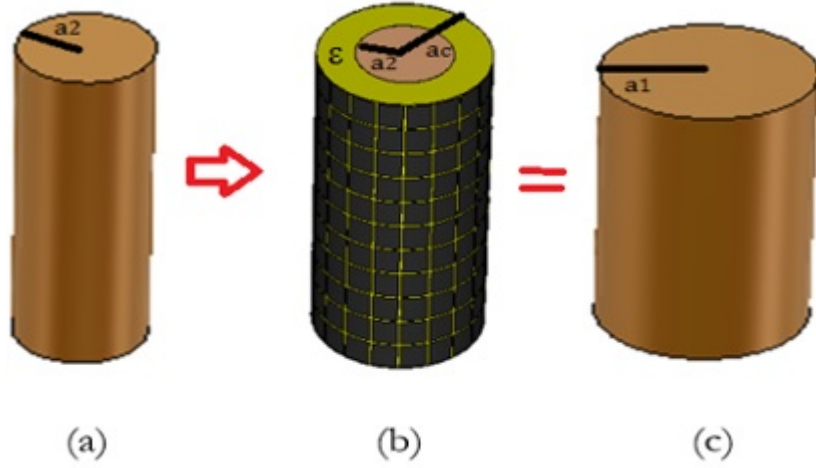
Figure 4.20: Structures of (a) given, (b) coated and (c) target conducting cylinders.

$$c'_n = ((J_n(\beta a_c) - \frac{J_n(\beta a_2)}{Y_n(\beta a_2)} Y_n(\beta a_c))(\frac{Z_s}{j\eta_0} J'_n(\beta_0 a_c) - J_n(\beta_0 a_c)) - \frac{Z_s}{j\eta}(J_n(\beta_0 a_c))$$

$$(J'_n(\beta a_c) - \tfrac{J_n(2)Y'_n(\beta a_c)}{Y_n(\beta a_2)})) \times ((J_n(\beta a_c) - \tfrac{J_n(\beta a_2)}{Y_n(\beta a_2)} Y_n(\beta a_c))(H_n^{(2)}(\beta_0 a_c) - \tfrac{Z_s}{j\eta_0} H_n^{(2)\prime}(\beta_0 a_c)) +$$
$$\tfrac{Z_s}{j\eta} H_n^{(2)}(\beta_0 a_c)(J'_n(\beta a_c) - \tfrac{J_n(\beta a_2)Y'_n(\beta a_c)}{Y_n(\beta a_2)}))^{(-1)} \quad (4.54)$$

The first harmonic of these coefficients are:

$$c_0 = \frac{-\pi}{\pi - 2j\ln(\beta_0 a_1)} \tag{4.55}$$

$$c'_0 = \frac{\pi\omega\mu a_c[Z_s\beta_0 a_c(\ln(\beta a_c) + \ln(\beta a_c)(\epsilon - 1))] + 2\eta_0\pi Z_s}{4j\eta_0 Z_s \ln(\beta a_2) + \ln(\beta a_2)\ln(\beta a_c)\omega\mu a_c[4\eta_0 + 2j\epsilon Z_s\beta_0 a_c] - 4\eta_0\omega\mu a_c\ln(\beta_0 a_c)\ln(\beta a_c)} \tag{4.56}$$

Equating them, the required surface impedance is obtained as:

$$Z_s = j\frac{2\eta_0\omega\mu a_c \ln(\frac{a_c}{a_2})[-2\ln(\beta_0 a_c) + M]}{-\omega\mu a_c \beta_0 a_c[M\ln(\beta a_c) + \ln(\beta a_2)(\epsilon - 1)) - 2\epsilon\ln(\beta a_2)\ln(\beta_0 a_c)] + 2\eta_0(2\ln(\beta a_2) - M)} \tag{4.57}$$

where $M = \sqrt{\pi^2 + 4(\ln(\beta_0 a_1))^2}$

Metasurface Design

Based on the results achieved for the required surface impedance, nanostructured graphene metasurfaces are designed to cover the cylinders to change their scattering. The structure of the proposed graphene based metasurface is shown in Fig. 4.21. The surface impedance of the graphene nanopatches is calculated by [84]:

$$Z_s = \frac{P}{\sigma_s(P - g)} - j\frac{\pi}{2\omega\epsilon_0(\frac{\epsilon+1}{2})P\ln\csc(\frac{\pi g}{2P})} \tag{4.58}$$
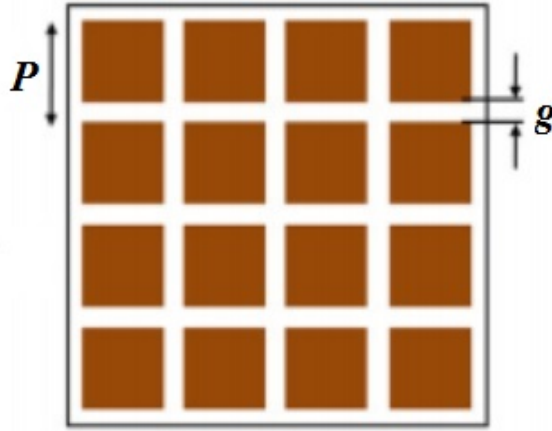
Figure 4.21: The structure of nanostructured graphene metasurface

Where ϵ is the dielectric constant of the dielectric layer, P is the periodicity of the graphene patches, g is the gap distance between the patches and σ_s is the surface conductivity of the graphene.

The goal is to change the scattering properties of a given dielectric cylinder with radius of $a_2 = 7$ μm and relative permittivity of $\epsilon = 4$ into that of target dielectric cylinders with the same material and the radii of $a_1=14$ μm (case d_1)

73

and a_1=3.5 μm (case d_2) at f=3 THz. A metasurface based on graphene patches is designed for both cases with different chemical potentials. The required surface impedances are achieved using the eq. (4.51) as $Z_s = -j517\Omega$ for the case d_1 and $Z_s = j761\Omega$ for the case d_2. Dimensions of the metasurface structure and also, the characteristics of graphene are optimized to realize the required surface impedances as follows: P=3.365 μm, g=0.59 μm, T=300 K and τ=1.5 ps, $\mu_c = $ 0.66 eV for the case d_1 and 0.14 eV for the case d_2.

As the next example, we tried to transform the SW of a conducting cylinder with a radius of $a_2 = 9$ μm to that of other cylinders with a radius of a_1 =18 μm (case m_1) and a_1 =4.5 μm, (case m_2) at f=3 THz. The dielectric layer which covers the cylinder has a radius of $a_c = 16$ μm and the dielectric constant of $\epsilon = 2$. The required surface impedance to transform the SW of the conducting cylinder with a radius of 9 μm to that of another cylinder with a radius of 18 μm is achieved as Z_s = -j180 Ω and to that of another cylinder with radius 4.5 μm is obtained as Z_s = -j185 Ω. T=300 K, P=11.17 μm, g=2.5 μm, τ=1.9 ps, $\mu_c = 0.64$ eV for the case m_1 and 0.78 eV for the case m_2 are chosen for the nanostructured graphene metasurface. A summary of the optimized parameters for the designed metasurfaces for dielectric and metallic cylinders are illustrated in the table. 4.1

Table 4.1: Summary of the parameters of the designed metasurfaces

		μ_c(ev)	D(μm)	g(μm)	T(k)	τ(ps)
Dielectric	Case d_1	0.66	3.365	0.59	300	1.5
	Case d_2	0.14				
Metallic	Case m_1	0.64	11.17	2.5	300	1.9
	Case m_2	0.78				

Results and Discussions

SW of an infinite cylinder is calculated as [83]:

$$Total\ SW = \frac{4}{\beta_0} \sum_{n=-\infty}^{\infty} |C_n|^2 \qquad (4.59)$$

where β_0 is the propagation constant in free space, and c_n, is the nth scattering coefficient.

The SW of the given, target and covered dielectric cylinders for the cases d_1 and d_2 are shown in Figs. 4.22 and 4.23, respectively. It can be seen that the SW of the given cylinder has become the same as of the target cylinder for both cases. Moreover, analytical and numerical results show good agreement.

Figures 4.24 and 4.25 show the distribution of electric fields for the given, target and covered dielectric cylinder for both cases. It can be seen that the surrounding electric fields of the covered cylinders become similar to that of the target cylinders.
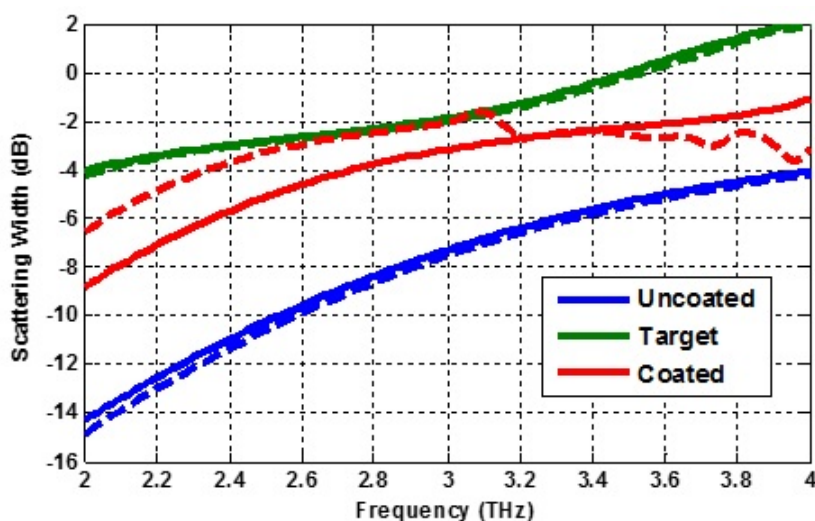
Figure 4.22: Total scattering width of the given, coated and target dielectric cylinders for the case d_1. Solid line: Analytical, Dashed line: Numerical

Fig. 4.26 presents the total RCS of the cylinders obtained by CST Microwave Studio [119] in polar system for $\phi = 90°$ and $\theta = 90°$ planes. It is proved that scattering manipulation is achieved even for a finite dielectric cylinder for all observing angles.

Figures 4.27 and 4.28 depict the SW of the given, target and coated conducting
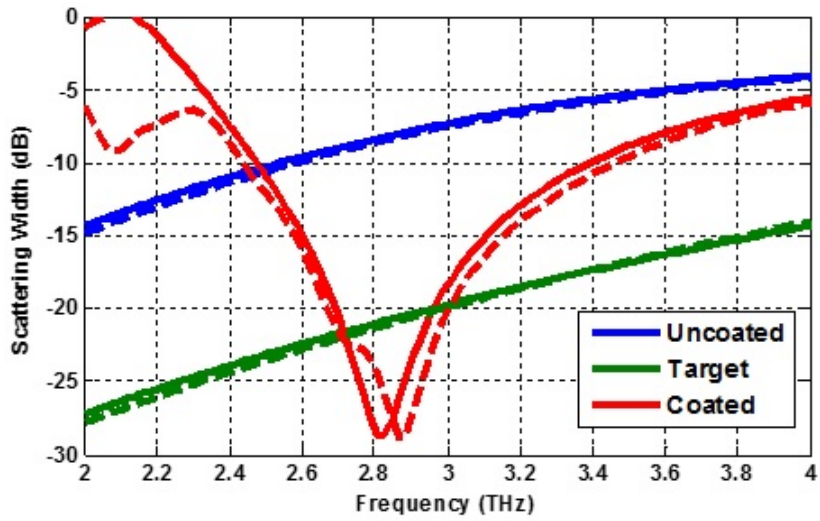
Figure 4.23: Total scattering width of the given, coated and target dielectric cylinders for the case d_2. Solid line: Analytical, Dashed line: Numerical
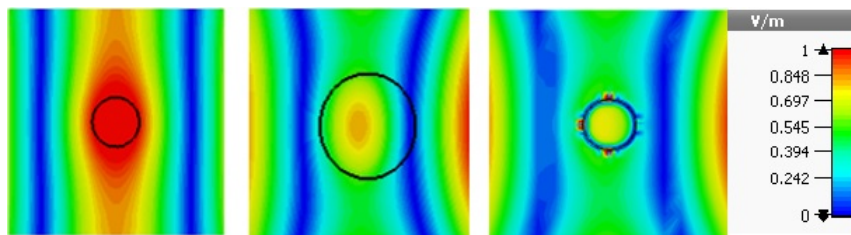
Figure 4.24: Amplitude distribution of electric field surrounding the (a) given, (b) target and (c) coated dielectric cylinders for the case d_1.
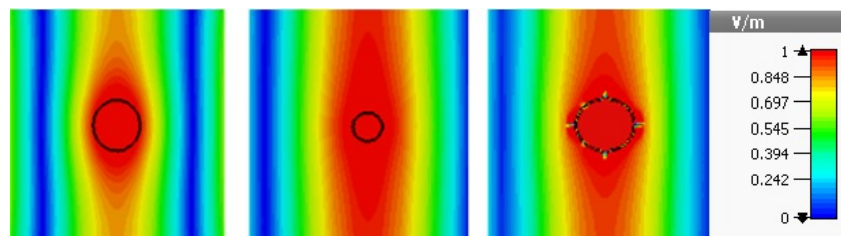
Figure 4.25: Amplitude distribution of electric field surrounding the (a) given, (b) target and (c) coated dielectric cylinders for the case d_2

76
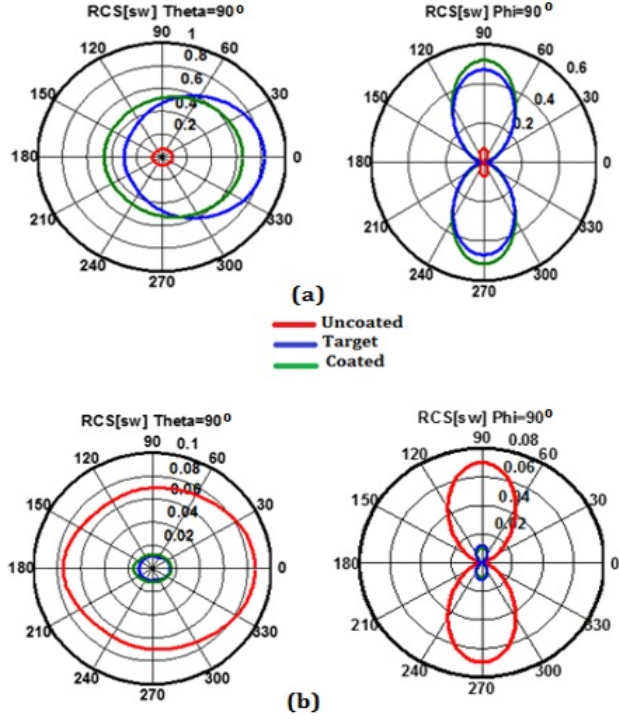
Figure 4.26: Polar RCS patterns of dielectric cylinders for $\theta = 90°$ and $\phi = 90°$ at 3 THz for a) case d_1 and b) case d_2.

cylinders indicating the transformation of the SW of the given cylinder to that of the target one at 3THz.

Perturbation of the incident wave after passing the cylinders for both cases are shown in Figs. 4.29 and 4.30. Transforming the scattering properties of the given dielectric cylinders is concluded.

Figure 4.31 shows total RCS of the cylinders in the polar system in $\phi = 0°$ and $\theta = 90°$ at the center frequency for both cases. It can be observed that 3D RCS of the target and coated cylinders are almost the same for all observing angles.
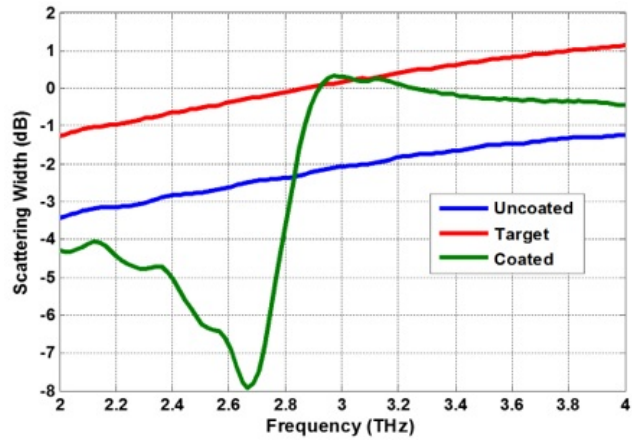
Figure 4.27: Numerical result for total scattering width of the given, coated and target conducting cylinders for the case m_1.
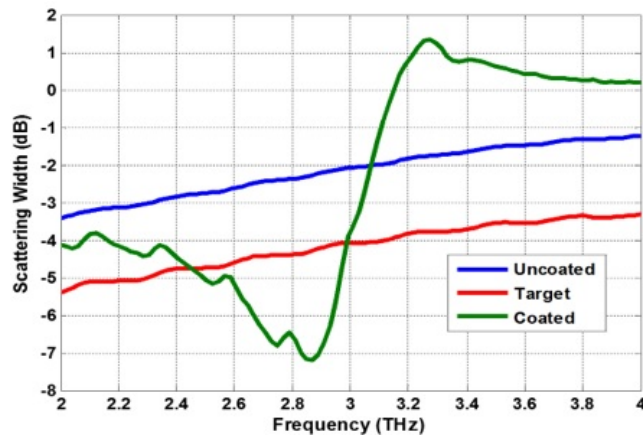
Figure 4.28: Numerical result for total scattering width of the given, coated and target conducting cylinders for the case m_2.
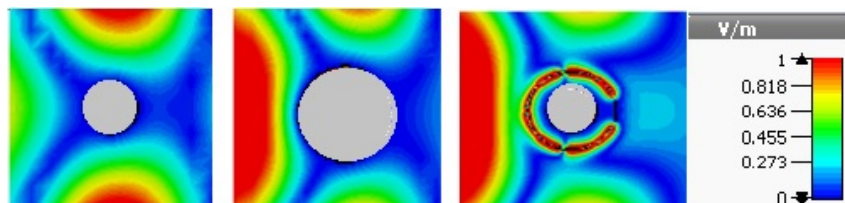
Figure 4.29: Amplitude distribution of electric fields surrounding the (a) given, (b) target and (c) coated conducting cylinders for the case m_1.
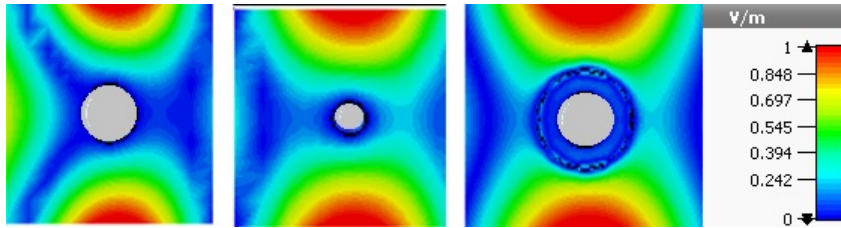
Figure 4.30: Amplitude distribution of electric fields surrounding the (a) given, (b) target and (c) coated conducting cylinders for the case m_2.
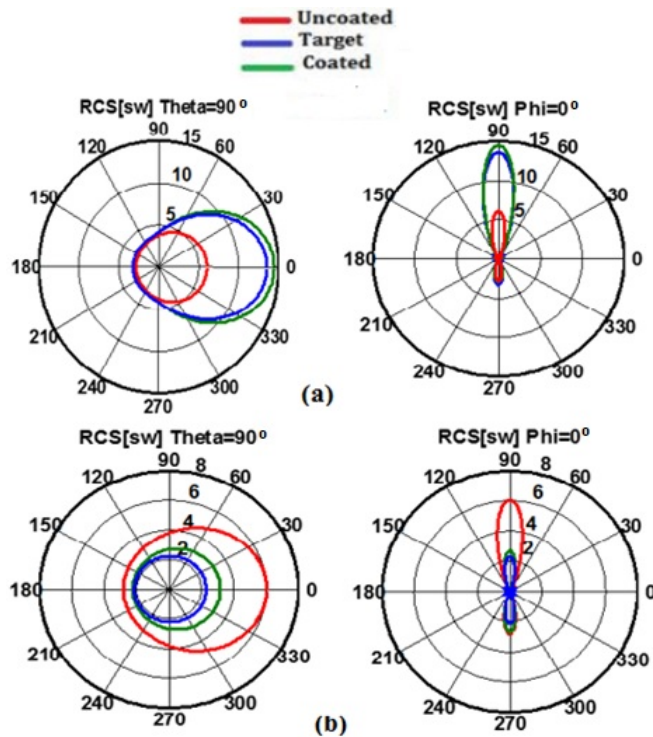
Figure 4.31: Polar RCS patterns of conducting cylinders for $\theta = 90°$ and $\phi = 90°$ at 3THz for a) case m_1 and b) case m_2.

79

4.2 Design of reconfigurable metasurface lens based on graphene split ring resonators

4.2.1 Introduction

One of the most novel methods to focus electromagnetic waves is utilizing meta-material based lenses. However, these kinds of lenses are bulky and their implementation is difficult [125]. Furthermore, they are highly sensitive to the loss [126]. Recently, metasurfaces based lenses, have been designed for focusing electromagnetic waves. They are ultra thin and can be easily fabricated [127]. In [128], the concept of Pancharatnam-Berry (PB) was introduced for the first time to manipulate circularly polarized plane waves. Utilizing this concept allows us to design various applications such as: polarization converters [129], focusing mirrors [130] and flat lenses [131].

In this section, a reconfigurable lens based on graphene metasurface which operates as a converging/diverging lens for a circularly polarized impinging wave is designed. The transmitted wave will be a circularly polarized one with opposite handedness and its phase is controlled by P-B phase concept. Unit cells of the proposed metasurface consist of two graphene split ring resonators on two sides of a substrate. The required phase shift is achieved by proper ring 's rotation. As mentioned in section 2, the requirements for the P-B conditions are having the same transmitted amplitude and 180° phase difference for two orthogonal linearly polarized impinging waves. The element structure and graphene characteristics are optimized to satisfy these conditions at a desired frequency. By changing the chemical potential of graphene, the operating frequency and focusing point can be adjusted as it will be illustrated in this section.
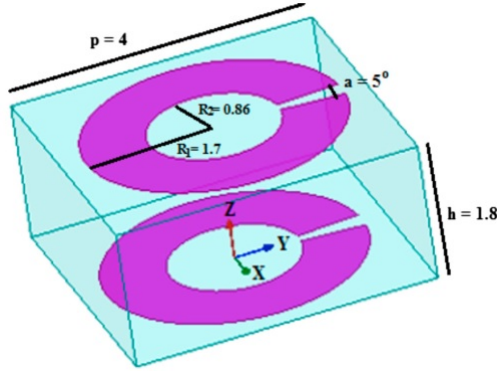
Figure 4.32: Structure of the unit cell of the metasurface lens (values are in μm).

4.2.2 Designing of the element of metasurface lens

The structure of the proposed graphene based element as building blocks of the reconfigurable metasurface lens is shown in Fig. 4.32. The elements consists of a dielectric substrate with dielectric constant of 2.25 and two split ring resonators printed on both sides of it. The geometric parameters which have been optimized to achieve the requirement of PB conditions at 21THz are presented in Table 4.2. Where p is the periodicity of the unit cell, R_1 is the outer radius of the ring, R_2 is the inner radius of the ring, a is the opening angle of the ring and h is the height of the dielectric layer. Furthermore, the characteristics of graphene are chosen as: $T = 300K$, $\tau = 2ps$ and $\mu_c = 1.6eV$. According to [132]- [134], these values are physible. It is worth noting that, to obey PB conditions the designed element for this purpose should be anisotropic to create 180° phase difference for transmitted waves which are obtained from the two linearly polarized incident waves. The graphene based metasurface lens has the advantage of having a wide tunability by adjusting the chemical potential of graphene [135].

Table 4.2: Optimized parameters of the ring resonator

P	R_1	R_2	a	h
4 μm	1.7 μm	0.86 μm	5°	1.8 μm

To show the satisfaction of PB phase requirements, the transmission properties of the considered element is investigated using CST Microwave Studio [119] and
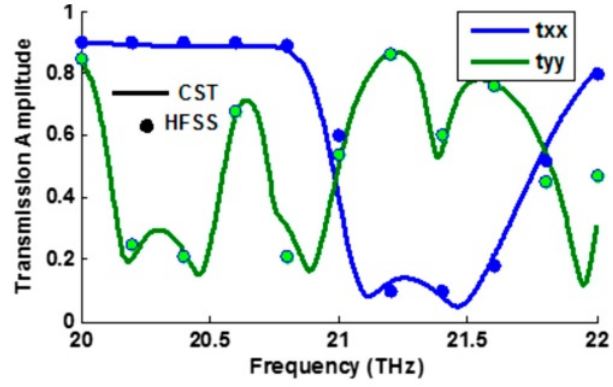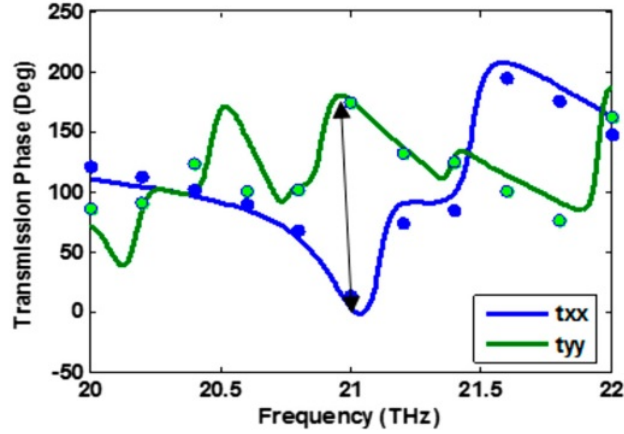
Figure 4.33: Transmitted (a) amplitude and (b) phase for orthogonal linearly polarized incident wave for $\mu_c = 1.6eV$.

HFSS [123]. Figure 4.33, depicts the amplitude and phase of the transmitted wave for two linearly polarized incident plane waves in two orthogonal directions. It indicates that t_{xx} and t_{yy} have the same amplitude with 180° phase difference at 21THz. Good agreement between CST and HFSS results is observed. Besides, the transmission amplitude and phase of the wave in the case of circularly polarized plane wave incidence, is shown in Fig. 4.34, verifying the PB phase concept. As it was predicted, the transmitted wave has circular polarization with opposite handedness to that of the impinging one (the amplitude of the cross polarized wave is much higher than that of the co–polar one and a transmission phase equal to twice of the rotation angle of the element is achieved). Figure 4.34(b) shows good agreement between theory and simulation results.
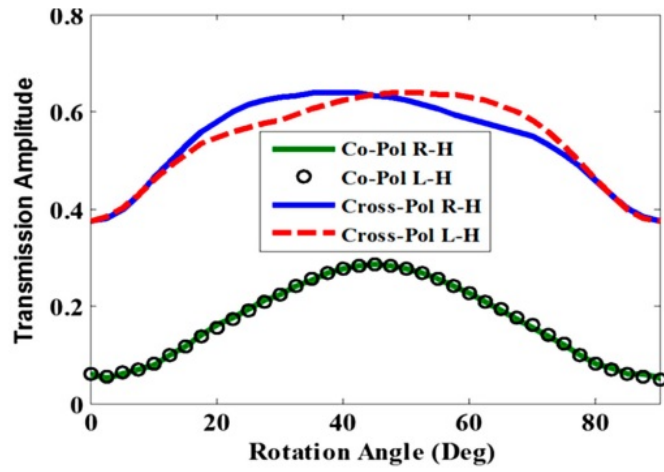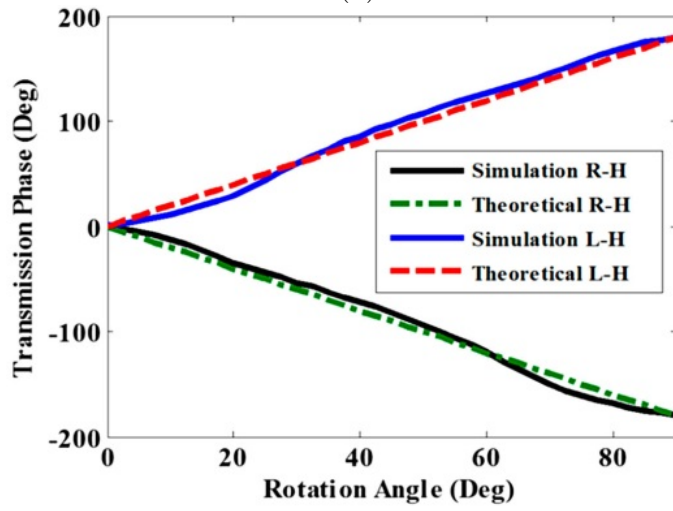
Figure 4.34: Transmitted (a) amplitude and (b) phase for cross circularly polarized incident wave versus rotation angle of the elements.

Table 4.3: Required phase shifts for 21 and 19.63 THz at the two different focal points.

Element number	Required phase shift (°) at $f = 21$ THzFocal point $= 28$ µm	Required phase shift (°) at $f = 19.63$ THzFocal point $= 26$ µm
1	0	0
2	7.1	7.2
3	28.2	28.3
4	62	62.1
5	107	106.7
6	161.4	160.3
7	223.5	221.1
8	292	287.7
9	365.6	358.8

To show that the tunability of the designed element is feasible, the chemical potential of graphene is changed from 1.6 eV to 1.4 eV which leads to the operating frequency shift from 21 THz to 19.63 THz in Fig. 4.35 and according to eq. 2.6, the focal length (the distance between focal point and the metasurface) will change. Table. 4.3 reports the required phase shift for 9 elements based on their distance to the origin. It indicates that the required phase shift at 21THz for the focal length of 28μm is almost the same as he required phase shift at 19.63 THz for the focal length of 26μm. Therefore, it can be concluded that the considered metasurface consisting of the designed elements will operate as a reconfigurable focusing lens at 21 THz with focal length of 28μm and at 19.63 THz for the focal length of 26μm (with graphene chemical potentials of 1.6 eV and 1.4 eV, respectively). If the meatsurface lens is designed based on the required phase shift at 21 THz, then the maximum phase error will be 6.8degrees at 19.63 THz. As, the transmitted phase related to each element is twice of its rotation angle regardless to frequency, it is understood that a metasurface consisting of elements with rotation angles designed at 21 THz, will operate properly at 19.63 THz, since the required phase shift at the two frequencies is almost the same.
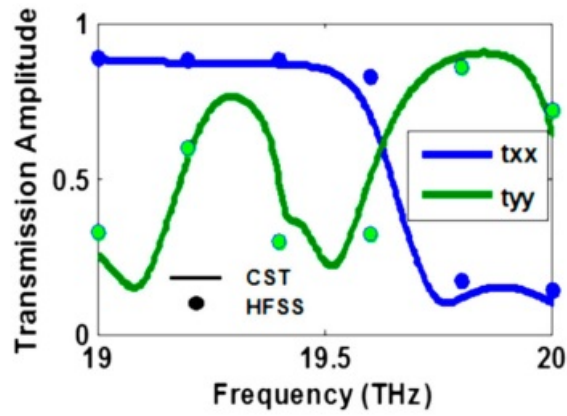
(a)
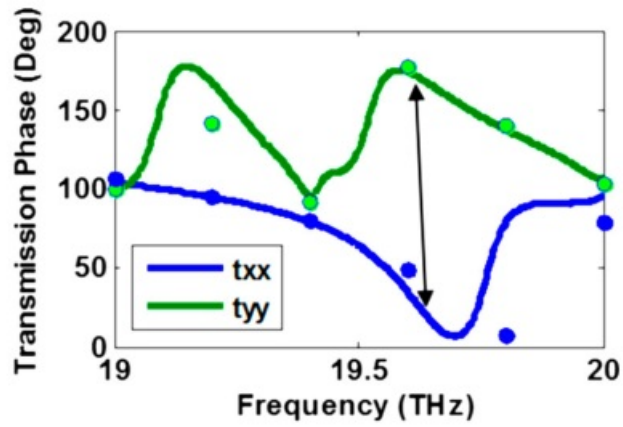
(b)

Figure 4.35: Transmitted (a) amplitude and (b) phase for orthogonal linearly polarized incident wave for $\mu_c = 1.4eV$.

4.2.3   Metasurface lens design and results

Figure 4.36 shows a super cell of the proposed metasurface lens consisting of 18 elements which are symmetrically placed relative to the origin with counter-clockwise rotations. The rotation angle of the elements has been designed using eq. (2.6). The super cell is repeated periodically in the y direction to realize a flat lens. The goal is to focus the left handed circularly polarized incident wave with opposite handedness in the focal point of 28μm at 21 THz.

| Phase shift (°) | 0 | 7.1 | 28.2 | 62 | 107 | 161.4 | 223.5 | 292 | 365.5 |
| Rotation angle (°) | 0 | 3.55 | 14.1 | 31 | 53.5 | 80.7 | 111.75 | 146 | 182.75 |
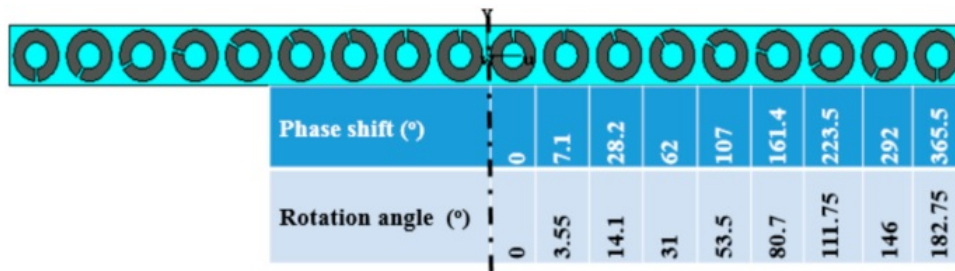
Figure 4.36: Structure of the supper cell of the metasurface lens and the required phase shifts.

Note that for a left handed circularly polarized incident wave, the elements should rotate in counter-clockwise direction for focusing purpose, because in this case an increasing phase shift is required to compensate the phase difference $k_0 d$, where k_0 is the phase constant in free space and d is the distance of each element to the focal point. For clockwise-rotated elements, the R/L curves of Figure 4.34(b) must be reversed, so the elements with clockwise rotation is used for focusing purpose when a right-handed circularly polarized wave incident on the metasurface.

Finally, the designed metasurface lens is illuminated by a left handed circularly polarized plane wave. The transmitted electric energy density at 21 THz which is obtained by CST Microwave Studio is shown in Fig. 4.37. The transmitted electric energy density at 19.63 THz with different chemical potential depicts in Fig. 4.38. The figure indicates that the transmitted wave focused in different focal point which represents reconfigurability of the designed metasurface lens.

Furthermore, the transmitted electric field as a result of illumination of a
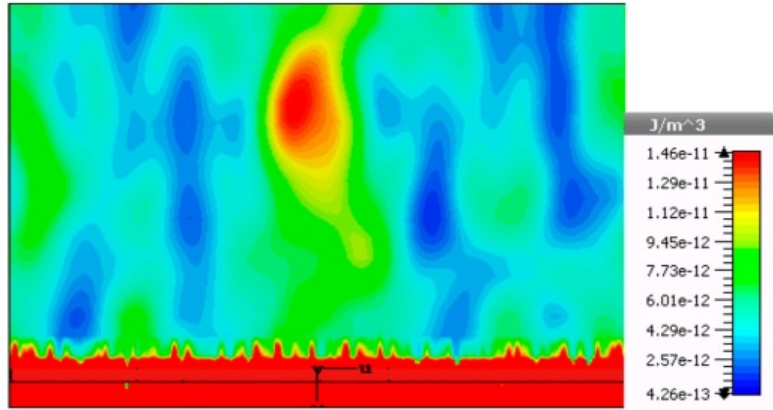
Figure 4.37: Transmitted electric energy density at 21 THz.
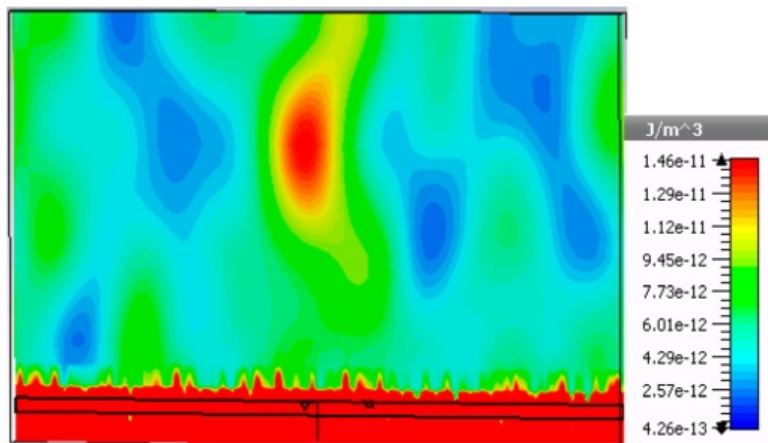
Figure 4.38: Transmitted electric energy density at 19.63 THz.
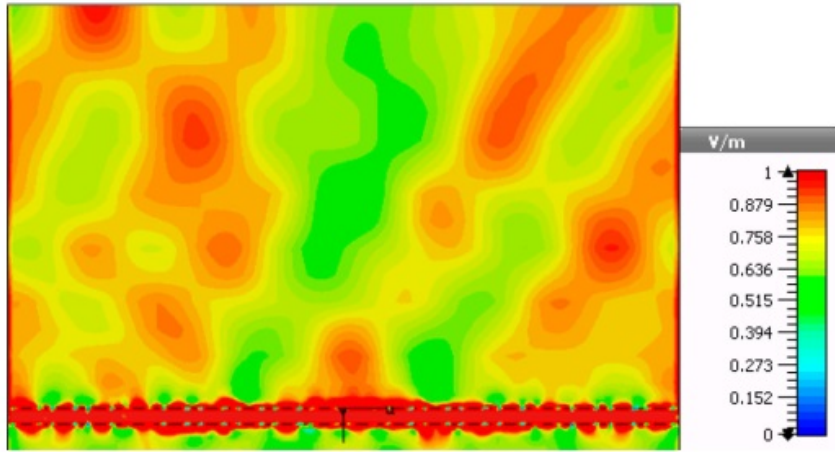
Figure 4.39: Amplitude of the transmitted electric field at 21 THz for diverging purpose.

right handed circularly polarized plane wave is illustrated in Fig. 4.39. It can be concluded that changing the handedness of the incident plane wave results in a diverging transmitted wave instead of converging one [56]. The reason is that for a right handed circularly polarized incident wave in contrary to a left handed one, the transmitted phase increases by increasing the rotation angle of the elements (see Fig. 4.34(b)).

4.3 Designing a tunable polarization converter

4.3.1 Introduction

Polarization is an important characteristic of electromagnetic waves [136]. Polarization conversion of electromagnetic waves is necessary for some applications such as sensing, imaging, and communications [137], [138]. There are several conventional techniques to change the wave polarization which includes using birefringence materials and optical gratings [139], [140]. Unfortunately, these methods usually need bulky structures [136]. Recently, metamaterial and metasurfaces have attracted significant attention because of their new profile properties in realizing different applications, for instance: negative refraction, invisible

cloaking and sub-diffraction imaging [141]- [143]. Several polarization converters based on metamaterials and metasurfaces have been designed from microwave frequencies to visible regime [144], [145].

In this section, a tunable polarization converter based on graphene metasurface is presented. The linear polarization of the reflected wave from the proposed structure rotates 90 degrees regarding to the incident wave. Furthermore, by changing the chemical potential of graphene, polarization conversion frequency can be tuned.

4.3.2 Designing a tunable polarization converter

The proposed metasurface as a polarization converter is shown in Fig. 4.40. It consists of a graphene cut wire on a dielectric substrate with a dielectric constant of 2.25 backed by a ground plane. The cut wire allows excitation of a dipolar oscillation P with parallel and perpendicular components to the electric field of the impinging plane wave [146]. The perpendicular component of P produces a reflected wave with cross polarization relative to the incident wave. By optimizing the considered element, the amplitude of the cross polarized reflected wave will be much higher than that of the co-polarized one. Therefore, the proposed structure performs as a reflective polarization converter. Optimized parameters of the metasurface structure and properties of graphene are obtained as follows: the periodicity $p = 2\mu$m, $L = 1.9\mu$m, $W = 0.4\mu$m, $h = 1\mu$m , chemical potential of graphene $\mu_c = 0.9$ eV and relaxation time of graphene $\tau = 3$ps.

4.3.3 Results and discussion

The designed metasurface is illuminated by a x polarized plane wave. Figure 4.41 presents the amplitude of the reflected wave for co- and cross polarization components obtained by CST Microwave Studio [119]. It indicates that the amplitude of the reflection coefficient for the y polarization is 0.7 and for the x polarization is 0.3 which shows a clear polarization rotation from x to y direction
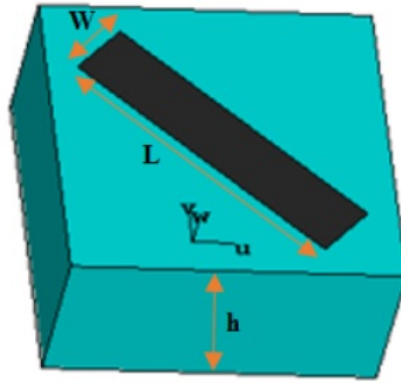
Figure 4.40: Structure of the proposed unit cell of the polarization converter.
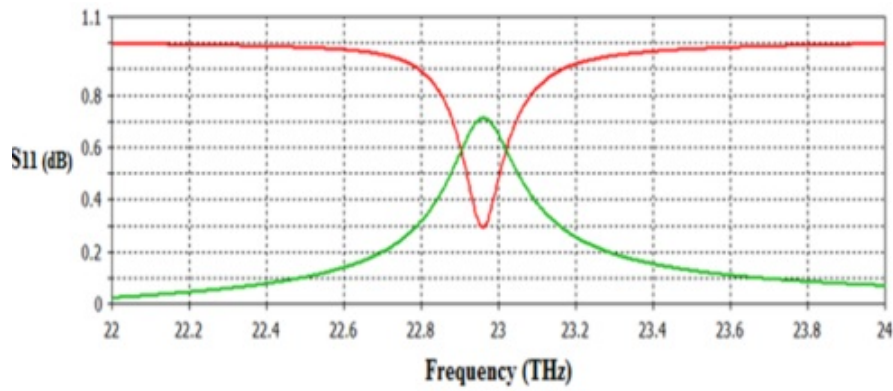
Figure 4.41: Amplitude of the reflected wave for co and cross polarization. Red: Co-, Green: Cross-polarization.

in reflective mode. Figure 4.42 illustrates that by changing the chemical potential of the graphene from 0.9 eV to 0.85 eV and 0.95 eV, the operating frequency of the designed polarization converter will shift to 22.3THz and 23.5 THz, respectively. Therefore, the considered graphene metasurface operates as a tunable polarization converter in reflective mode.
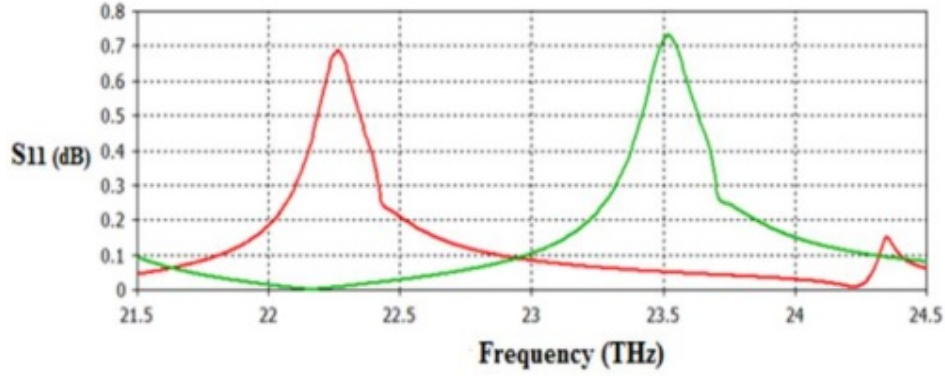
Figure 4.42: Amplitude of the reflected wave for cross polarization with different chemical potential. Red: $\mu_c = 0.85 eV, Green : \mu_c = 0.95 eV$.

4.4 Designing a graphene based leaky wave antenna loaded by a dielectric slab for gain improvement

4.4.1 Introduction

Leaky wave antennas, as low profile and high gain radiating structures have attracted great interests, in recent years. They are able to be integrated into different devices [147]. They present unique properties such as scanning of the main radiation beam with frequency [148]. A large number of investigations have been performed relating to the radiation performance of these antennas [149]-[151]. Beam distortion and narrow bandwidth are two disadvantages of leaky wave antennas. Various configurations have been introduced to overcome these drawbacks [152]- [153]. In [154], a sinusoidally-modulated surface impedance has been presented to achieve a higher gain.

The purpose of this section, is to improve the gain of a sinusoidally modulated graphene based leaky wave antenna by loading it with a dielectric slab. The height and distance of the slab to the antenna is optimized to achieve the considered goal.
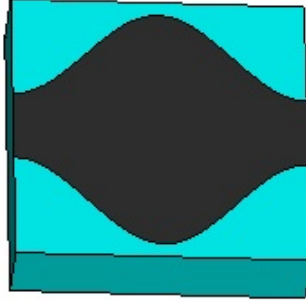
Figure 4.43: The unit cell of the leaky wave antenna.

Table 4.4: The optimized parameters of the structure ′s element and properties of the graphene.

P	h	T	μ_c	τ
80 μm	20 μm	300° K	0.5 eV	0.1 Ps

4.4.2   Designing graphene based leaky wave antenna

The structure of the unit cell of the proposed leaky wave antenna is shown in Fig. 4.43. The unit cell consists of a sinusoidally modulated graphene based metasurface on a dielectric substrate with relative permittivity of $\epsilon_r = 3.8$. It has been optimized to achieve broadside main beam radiation at 2.55 THz. The main beam angle of a leaky wave antenna is obtained as follows [155].

$$\theta_0 = \cos^{-1}(\beta/k_0) \tag{4.60}$$

where k_0 is the propagation constant in the free space. It indicates that in order to have a leaky wave antenna based on the designed metasurface, the propagation constant in the antenna should be less than that in the air [156].

The optimized parameters of the structure ′s element and properties of the graphene are presented in Table. 4.4.

where p is the periodicity of the element, h is the height of the substrate, T is the temperature, μ_c is the chemical potential of graphene and τ is relaxation time of graphene. The surface impedance of the graphene with the considered values will be $Z_s = (169.95 + j\ 272.38)\ \Omega$.

The element is simulated with CST Microwave Studio [119] and its scattering
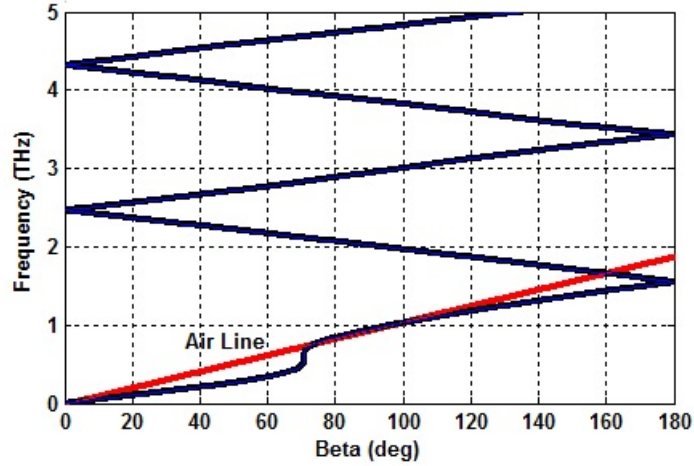
Figure 4.44: Dispersion diagram of the leaky wave antenna.

parameters (S_{ij}) have been achieved. Using the following expression, propagation constant versus frequency is obtained [156].

$$\beta = Im[\frac{\cosh^{-1}\left(\frac{S_{12}S_{21}+((1+S_{11})(1-S_{22}))}{2S_{21}}\right)}{p}]\qquad(4.61)$$

The dispersion diagram is reported in Fig. 4.44. It can be observed that, the diagram at the operating frequency (2.55 THz) is above the air line which represents a leaky mode. Furthermore, at the considered frequency, β is zero, which corresponds to a broadside main beam.

Figure 4.45(a) illustrates the structure of the proposed leaky wave antenna and Fig. 4.45(b) presents the radiation pattern of the antenna at 2.3 THz, 2.55 THz and 2.9 THz obtained by HFSS [123]. It indicates that the main beam 's angle at 2.3 THz is -20degree, at 2.55 THz is in broadside and at 2.9 THz is 20degrees which are in agreement with the dispersion diagram.

4.4.3 Improving gain of the leaky wave antenna by loading a dielectric slab

For improving the gain of the designed leaky wave antenna, a dielectric slab with the same relative permittivity as of the substrate is loaded to it as shown in Fig. 4.46. The height of the dielectric slab and its distance to the substrate have been
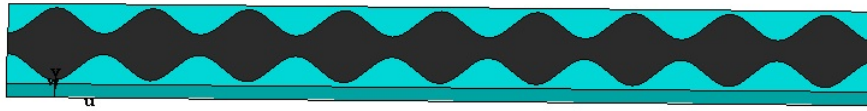
(a)
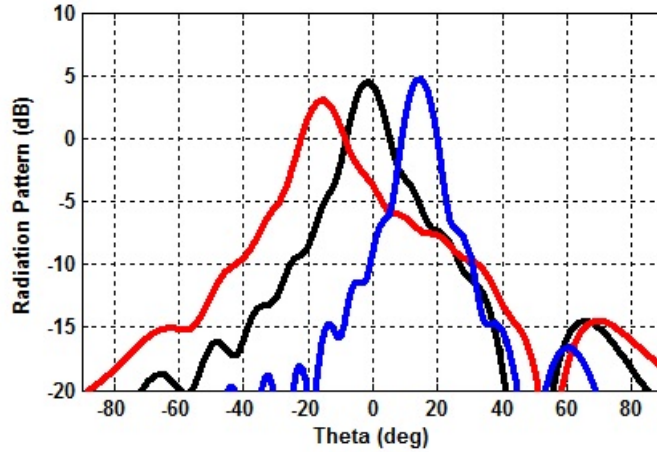
(b)

Figure 4.45: a) Structure of the designed leaky wave antenna. (b) Radiation pattern of the antenna. black: 2.55 THz, red: 2.3 THz, blue: 2.9 THz.

optimized to obtain the maximum gain for the loaded leaky wave antenna ($h_2 = 10\mu$m and $d = 20\mu$m). Figure 4.47 compares the distribution of the electric field distribution of the leaky wave antenna with and without the slab.

It can be observed that in the antenna loaded by the slab shown in Fig. 4.47(b), the electromagnetic wave propagates a longer distance on the surface of the antenna than in the unloaded one. The reason is that when the wave radiates into the air, hits the dielectric slab and some part of it will reflect back to the antenna. This part propagates along the surface again and radiate to the air and again some part of it reflects after incidence to the slab. This procedure continues and leads to trapping the wave between the dielectric substrate and slab. There-fore, a larger part of the antenna contributes to the radiation process compared to the unloaded antenna which causes a good improvement in aperture efficiency and gain of the antenna. The radiation pattern of the loaded leaky wave antenna at 2.55 THz for the broadside main beam is illustrated in Fig. 4.48. By com-paring Fig. 4.45(b) and Fig. 4.48, it can be understood that gain enhancement is achieved with loaded dielectric slab in the broadside direction. Figure 4.49

94
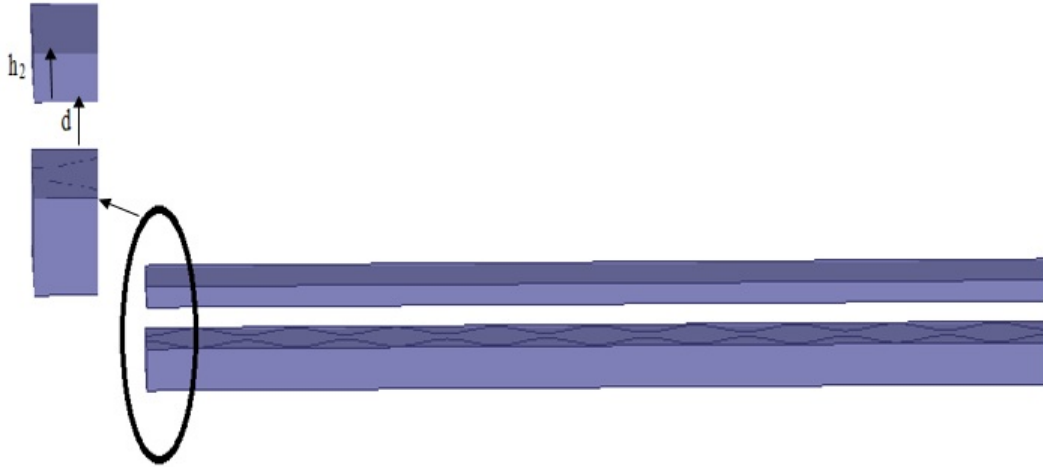
Figure 4.46: The structure of the leaky wave antenna loaded by a dielectric slab.
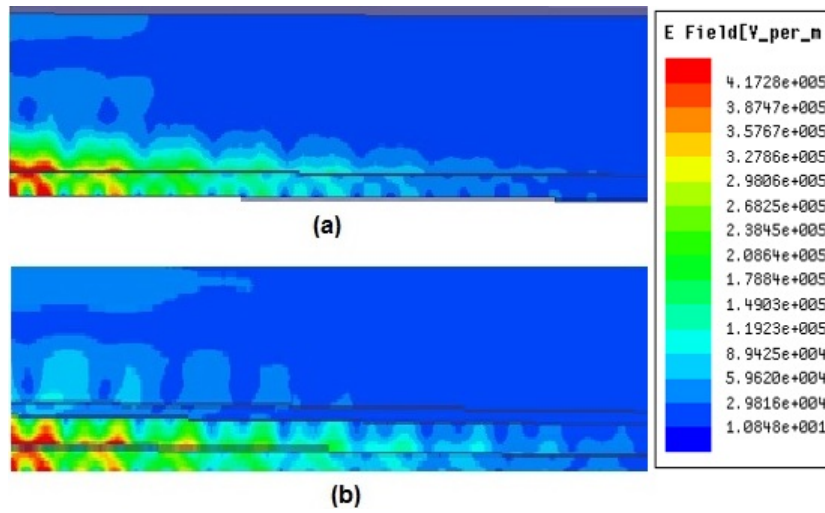
Figure 4.47: Electric field distribution of the leaky wave antenna from the side view. (a) without slab. (b) with slab.
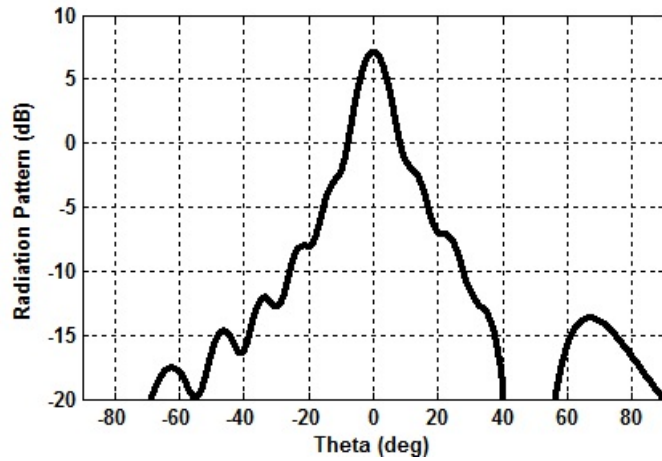
Figure 4.48: Radiation pattern of the leaky wave antenna loaded with the dielectric slab.
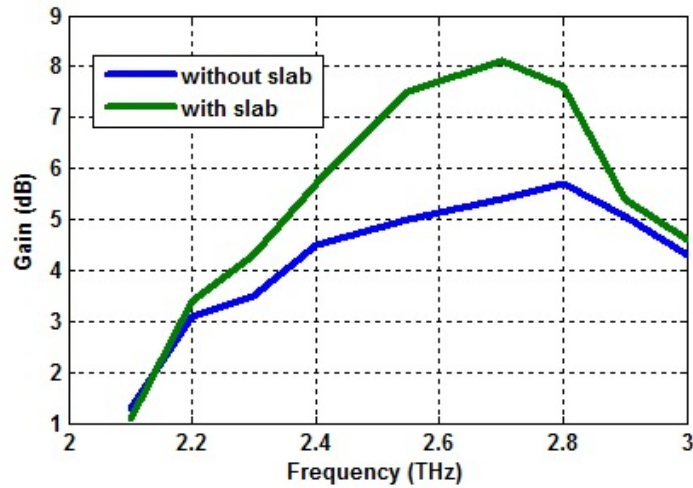
Figure 4.49: Gain of the leaky wave antenna with and without the dielectric slab.

compares the gain of the loaded and unloaded designed leaky wave antennas versus frequency. It indicates a noticeable gain improvement for the loaded antenna from 2.2 THz to 3 THz. The figure presents a more gain enhancement for the frequencies related to near to broadside main beam angle.

4.5 Synthesis of Graphene and Biasing

Two main methods are considered for synthesis of graphene which are explained in the following:

4.5.1 Exfoliation and Cleavage

In this method, graphene is produced from a pure graphite sheet. Exfoliation and cleavage with chemical and mechanical energy break week bonds and separate out graphene sheets [157].

4.5.2 Thermal Chemical Vapor Deposition Techniques

Graphene synthesis with thermal chemical vapor deposition (CVD), has been presented in 2006 [158]. In this study, camphor was used on Ni foils to produce graphene. Firstly, camphor was evaporated at 180 degrees and pyrolyzed at 700 to 850 degrees with argon. After cooling, graphene sheets were produced on the Ni foils.

Fabrication of the graphene layer cloak around a cylinder is possible. Since graphene is mechanically flexible it is feasible to wrap the graphene based metasurface around each arbitrary object [120].

4.5.3 Graphene Biasing Methods

Several different techniques have been introduced for biasing the graphene. In [159], three methods of selfbiasing are shown. In [160], polysilicon pads are used under graphene to apply DC voltage. Another technique which is named ion-gel gated graphene transistor is presented in [161].

For biasing the graphene layer in our desined configurations, the structure in Fig. 4.50 is suggested. One metallic contact is put on graphene and the other one is put on top of the cylinder acting as a ground and a voltage supply is connected to the contacts. By changing the biasing voltage, the chemical potential of the graphene can be adjusted.
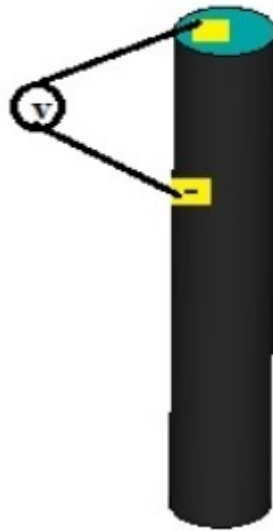
Figure 4.50: The suggested structure for biasing the cloaked cylinder.

Chapter five

Conclusion

In the first chapter of the thesis, metasurfaces and their applications were introduced briefly and the goal of this thesis was presented. The next two chapters dedicated to an introduction to metasurfaces and applications of graphene in metasurfaces for electromagnetic waves manipulation. Several metasurfaces based on graphene were designed and the analytical approaches were presented in detail in chapter four.

Mantle cloaking of a dielectric cylinder under oblique illumination of an incident TM_z plane wave was studied and the required surface impedance for the covering metasurface was achieved to make the considered cylinder invisible when it is exposed to the oblique incidence. Results for radar cross section (RCS) of both infinite and finite cloaked and uncloaked cylinders obtained analytically and numerically were presented. The results have indicated significant scattering reduction for the covered cylinders with a properly designed metasurfaces based on graphene. They also show good agreement between analytic and simulated results. Moreover, it was shown that by changing the chemical potential of graphene, tunable mantle cloaking was achieved for different frequencies and different incident angles.

A metasurface based on graphene strips was designed to cover a dielectric cylinder in order to make it invisible under illumination of TE and TM polarized plane waves. Using the surface impedance tensor for the considered metasurface, it was possible to control the surface impedance in x and z directions independently and therefore mantle cloaking for the two polarizations could be achieved

simultaneously. Numerical results obtained with CST Microwave Studio have showed RCS reduction for the cloaked cylinder with this method. Tunable dual polarized mantle cloaking was obtained by changing the chemical potential of graphene with different applied bias voltages.

Scattering manipulation of dielectric and conducting cylinders was investigated analytically. The required surface impedances to transform the scattering characteristics of the original cylinders to those of the cylinders with smaller or larger radii were achieved by equating the first scattering coefficients of the covered cylinders with that of the target cylinders. The results for RCS of the given, coated and target cylinders show that at the center frequency, the scattering of the covered cylinders is the same as of the target cylinders. Moreover, the electric field distribution around the covered and target cylinders are similar, verifying the correct analytical approach.

A reconfigurable metasurface lens based on graphene split ring resonators was presented. The unit cell of the metasurface was designed based on the P-B phase concept for circular polarization. The circularly polarized transmitted wave was focused at the considered focal point with different handedness to the incident plane wave. By adjusting the chemical potential of graphene, the operation frequency and the focal point could be controlled.

A tunable polarization converter based on graphene wires was proposed. It rotates the linear polarization of the incident wave in reflective mode. The result for the amplitude of the reflected wave shows that 70 % of the power of the x polarized impinging wave transforms to the y polarized wave. The operation frequency was adjusted by changing the chemical potential of the graphene.

A graphene based leaky wave antenna was presented. The unit cell of the antenna was designed according to the desired operation frequency and the main beam angle using the dispersion diagram. The gain of the antenna was improved by loading a dielectric slab on top of it. This slab causes the radiated wave to reflect back to the surface of the leaky wave antenna and reradiates again, making the effective size of the antenna larger and therefore the gain increases.

5.1 Publications

5.1.1 Journal papers

1. Zahra Hamzavi- Zarghani, Alireza yahaghi, Ladislau Matekovits. Reconfigurable Metasurface Lens Based on Graphene Split Ring Resonators Using Panacharatnam-Berry Phase Manipulation, Journal of Electromagnetics and Applications, Jan 2019.

2. Zahra Hamzavi-Zarghani, Alireza Yahaghi, Ladislau Matekovits. Dynamically Tunable Scattering Manipulation of Dielectric and Conducting Cylinders Using Nanostructured Graphene Metasurfaces IEEE Access. Vol. 7. Jan 2019.

3. Zahra Hamzavi-Zarghani, Alireza Yahaghi, Ladislau Matekovits and Ali Farmani. Tunable Mantle Cloaking Utilizing Graphene Metasurface for Terahertz Sensing Applications. Optics Express. Vol 27. 2019.

4. Zahra Hamzavi-Zarghani, Alireza Yahaghi, Ladislau Matekovits. Electrically Tunable Mantle Cloaking Utilizing Graphene Metasurface for Oblique Incidence International Journal of Electronics and Communications. (Revised)

5.1.2 Conference papers

1. Zahra Hamzavi-Zarghani, Alireza Yahaghi, Arman Bordbar. Analytical Design of Nanostructured Graphene Metasurface for Controllable Scattering Manipulation of Dielectric Cylinder, 26th Iranian conference on electrical engineering. (ICEE,2018).

2. Zahra Hamzavi- Zarghani, Alireza Yahaghi, Ladislau Matekovits. Tunable Lens Based on Graphene Metasurface for Circular Polarization International conference of electromagnetics in advanced applications. Sep. 2018.

3. Zahra Hamzavi- Zarghani, Alireza Yahaghi, Ladislau Matekovits. Tunable Polarization Converter Based on Graphene Metasurfaces IEEE RADIO International Conference. Oct. 2018.

4. Zahra Hamzavi- Zarghani, Alireza Yahaghi, Ladislau Matekovits. Analyti-

cal Design of a Metasurface Based Mantle Cloak for Dielectric Cylinder Under Oblique Incidence International Symposium on Telecommunications (IST), Dec. 2018.

5. Zahra Hamzavi- Zarghani, Ladislau Matekovits Alireza Yahaghi,. Improved Gain Graphene Based Leaky Wave Antenna Loaded by Dielectric Slab in THz Regime 13th European Conference on Antennas and Propagation. EuCAP 2019.

6. Zahra Hamzavi- Zarghani, Alireza Yahaghi, Ladislau Matekovits,.Vertical strips as mantle cloak of a dielectric cylinder under oblique incidence, International Conference on Electromagnetics in Advanced Applications (ICEAA 2019).

7. Zahra Hamzavi- Zarghani, Alireza Yahaghi, Ladislau Matekovits,.Mantle Cloaking of a Dielectric Cylinder under Oblique Incidence with Metasurfaces, PhotonIcs Electromagnetics Research Symposium (PIERS 2019).

5.2 Suggestions for future studies

1. Designing multifunction metasurfaces operating in both transmission and reflection modes

2. Designing multi band metasurface lenses and polarization converters

3. Using other 2-D tunable materials such as black phosphorus in metasurface structures

4. Designing broadband and multi band mantle cloaks with optimization algorithms

References

[1] J. Cheng, F. Fan and Sh. Chang, *Recent progress on graphene-functionalized metasurfaces for tunable phase and polarization control*, Nanomaterials. **9** (2019) 398.

[2] A.K. Geim and K.s. Novoselov, *The rise of graphene*, Nanomaterials. **6** (2007) pp. 183191.

[3] S. Savo, D. Shrekenhamer and W,J. Padilla, *Liquid Crystal Metamaterial Absorber Spatial Light Modulator for THz Applications*, Adv. Opt. Maters. **2** (2014) pp. 275279.

[4] N. Raeis-Hosseini and J. Rho, *Metasurfaces based on phase-change material as a reconfigurable platform for multifunctional devices*, Materials. **10** (2017) 1046.

[5] Z.C. Chen *et al.,*, *Realization of variable three-dimensional terahertz metamaterial tubes for passive resonance tunability*, Adv. Mater. **24** (2012) OP143OP147.

[6] L. Ju *et al.,*, *Graphene plasmonics for tunable terahertz metamaterials*, Nat. Nanotechnol. **6** (2011) pp. 630634.

[7] S.H. Lee *et al.,*, *Switching terahertz waves with gate-controlled active graphene metamaterials*, Nat. Mater. **11** (2012) 936.

[8] Y. Yao *et al.,*, *Broad Electrical Tuning of Graphene-Loaded Plasmonic Antennas*, Nano Lett. **13** (2013) pp. 12571264.

[9] Y. Yao *et al.,*, *Electrically tunable metasurface perfect absorbers for ultrathin mid-infrared optical modulators*, Nano Lett. **14** (2014) pp. 65266532.

[10] Z. Li, E. Palacios, S. Butun and K. Aydin, *Visible-freq metastructures for broadband anomalous reflection and high efficiency spectrum splitting*, Nano Lett. **15** (2015) 3.

[11] N. Engheta, R. Ziolkowski, *Metamaterial physics and engineering explorations*, John Wiley and sons, In: Handbook, NJ. (2006).

[12] J. Valentine, S. Zhang, T. Zentgraf, E. Ulin-Avi la, D. A. Genov, G . Bartal, and X. Zhang, *Three-dimensional optical metamaterial with a negative refractive index*, Nature.. **455** (2008) pp. 376379.

[13] V. M. Shalaev, *Optical negative-index metamaterials*, Nat. Photonics. **1** (2007) pp. 4148.

[14] J. B. Pendry, *Negative refraction makes a perfect lens*, Phys. Rev. Lett. **85** (2000) 3966.

[15] N. Fang, H. Lee, C. Sun, and X. Zhang, *Sub-diffraction-limited optical imaging with a silver superlens*, Science. **308** (2005) 5721.

[16] S. Inampu di and V. A. Podolskiy, *Diffractive imaging route to subwavelength pixels*, Appl. Phys. Lett. **102** (2013) 241115.

[17] A. Forouzmand, H. M. Bernety, and A. B. Yakovlev, *Graphene-loaded wire medium for tunable broadband subwavelength imaging*, Phys. Rev. B. **92** (2015) 085402.

[18] X. Zhang and Z. Liu, *Superlenses to overcome the diffraction limit*, Nat. Mat. **7** (2008) pp. 435441.

[19] B. Edwards, A. Al, M. G. Silveirinha, and N. R. Engheta, *Experimental verification of plasmonic cloaking at microwave frequencies with metamaterials*, Phys. Rev. Lett. **103** (2009) 153901.

[20] J. B. Pendry, D. Schurig, and D. R. Smith, *Controlling electromagnetic fields*, Science. **312** (2006) 5781.

[21] U. Leonhardt, *Optical conformal mapping*, Science. **312** (2006) 5781.

[22] D. Schurig, J. J. Mock, B. J. Justice, S. A. Cummer, J. B. Pendry, A. F. Starr, and D. R. Smith, *Metamaterial electromagnetic cloak at micro-wave frequencies*, Science. **314** (2006) 5801.

[23] C. Holloway, E. F. Kuester, J. Gordon, J. OHara, J. Booth, and D. Smith, *An overview of the theory and applications of metasurfaces: The two-dimensional equivalents of metamaterials*, IEEE Antennas Propag. Mag. **54** (2012) 2.

[24] K. Achouri, M. Salem, and Ch. Caloz, *General metasurface synthesis based on susceptibility tensors*, IEEE Trans. Antennas Propag. **63** (2015) 7.

[25] J. Cheng, D. Ansari, and H. Mosallaei, *Wave manipulation with designer dielectric metasurfaces*, Opt. Lett. **39** (2014) 21.

[26] B. Memarzadeh and H. Mosallaei, *Array of planar plasmonic scatterers functioning as light concentrator*, Opt. Lett. **13** (2011) 21.

[27] M. Veysi, C. Guclu, O. Boyraz, and F. Capolino, *Thin anistropic metasurfaces for simultaneous light focusing and polarization manipulation*, J. Opt. Soc. Am. B. **32** (2015) 2.

[28] A. Silva, F. Monticone, G. Castaldi, V. Galdi, A. Al, and N. Engheta, *Performing mathematical operations with metamaterials*, Science. **343** (2014) 6167.

[29] M. Farmahini-Farahani, J. Cheng, and H. Mosallaei, *Metasurfaces nanoantennas for light processing*, J. Opt. Soc. Am. B. **30** (2013) 9.

[30] Y. Yang, W. Wang, P. Moitra, I. I. Kra vchenko, D. P. Briggs, and J. Valentine, *Dielectric meta-reflectarray for broadband linear polarization conversion and optical vortex generation*, Nano Lett. **14** (2014) 3.

[31] Y. Zhao and A. Alu, *Tailoring the dispersion of plasmonic nanorods to realize broadband optical metawaveplate*, Nano Lett. **13** (2013) 3.

[32] N. Yu, P. Genevet, M. A. Kats, F. Aieta, J.-P. Tetienn e, F. Capasso, and Z. Gaburro, *Light propagation with phase discontinuities: generalized laws of reflection and refraction*, Science. **334** (2011) 6054.

[33] X. J. Ni, N. K. Emani, A. V. Kildishev, A. Boltasseva, and V. M. Shalaev, *Broadband light bending with plasmonic nanoantennas*, Science. **335** (2012) 427.

[34] 25. X. Ni, S. Ishii, A. V. Kildishev, and V. M. Shalaev, *Ultra-thin, planar, Babinet-inverted plasmonic metalenses*, Light: Science Application. **2** (2013) e27.

[35] A. Pors, M. G. Nielsen, R. L. Eriksen, and S. I. Bozhevolnyi, *Broadband focusing flat mirrors based on plasmonic gradient meta-surfaces*, Nano Lett. **13** (2013) 2.

[36] S. Sun, Q. He, S. Xiao, Q. Xu, X. Li, and L. Zhou, *Gradient-index meta-surfaces as a bridge linking propagating waves and surface waves*, Nat. Mater. **11** (2012) pp. 426-431.

[37] G. Li, M. Kang, S. Chen, S. Zhang, E. Y. B. Pun, K. W. Cheah, and J. Li, *Spin-enabled plasmonic metasurfaces for manipulating orbital angular momentum of light*, Nano Lett. **13** (2013) 9.

[38] J. Lin, P. Genevet, M. A. Kats, N. Antoniou, and F. Capasso, *Nanostructured holograms for broadband manipulation of vector beams*, Nano Lett. **13** (2013) 9.

[39] L. Huang, X. Chen, H. Mhlenb ernd, H. Zhang, S. Chen, B. Bai, Q. Tan, G. Jin, K.-W. Cheah, C.-W. Qiu, J. Li, T. Zen tgraf, and S. Zhang, *Three-dimensional optical holography using a plasmonic metasurface*, Nat. Commun. **4** (2013) 2808.

[40] M. Farmahini Farahani and H. Mosallaei, *Functional graded-index metasurfaces for IR radiation and guiding*, IEEE Trans. Nanotechnol. **14** (2015) 1.

[41] J. Cheng and H. Mosallaei, *Optical metasurfaces for beam scanning in space*, Opt. Lett. **39** (2014) 9.

[42] M. Farmahini Farahani and H. Mosallaei, *A birefringent reflectarray meta-surface for beam engineering in infrared*, Opt. Lett. **38** (2013) 4.

[43] J. Soric, A. Monti, A. Toscano, F. Bilotti, and A. Al, *Multiband and wideband bilayer mantle cloaks*, IEEE Trans. Antennas Propag. **63** (2015) 7.

[44] A. Monti, J. Soric, A. Al, A. Toscano, F. Bilotti, *Anisotropic mantle cloaks for TM a nd TE scattering reduction*, IEEE Trans. Antennas Propag. **63** (2015) 4.

[45] H. Chen, A. Taylor and N. Yu, *A review of metasurfaces: physics and applications*, physics.optics. **79** (2016) 076401.

[46] N. F. Yu, P. Genevet, M. A. Kats, F. Aieta, J. P. Tetienne, F. Capasso and Z. Gaburro, *Light Propagation with phase discontinuities: generalized laws of reflection and refraction*, Science. **334** (2011) 6054.

[47] X. J. Ni, N. K. Emani, A. V. Kildishev, A .Boltasseva and V. M. Shalaev, *Broadband light bending with plasmonic nanoantennas*, Science. **335** (2012) 427.

[48] X. Q. Zhang, Z .Tian, W. S. Yue, J. Q. Gu, S. Zhang, J. G. Han and W. L. Zhang, *Broadband terahertz wave deflection based on C-shape complex metamaterials with phase discontinuities*, Advanced Material. **25** (2013) 33.

[49] J. Zheng, X. Zhang, L. Liu, Q. Li, L. Singh, J. Han, E. Yan and W. Zhang, *Tailoring terahertz propagation by phase and amplitude control in metasurface*, Infrared Milli Terahz Waves. **38** (2017) 9.

[50] S. Sun, K .Y. Yang, C. M. Wang, T. K. Juan, W. T. Chen, C. Y. Liao, Q. He, S. Xiao, W. T. Kung, G. Y. Guo, L. Zhou and D. P. Tsai, *High-efficiency broadband anomalous reflection by gradient meta-surfaces*, Infrared Milli Terahz Waves. **12** (2012) 12.

[51] S. Sun, Q. He, S. Xiao, Q. Xu, X. Li and L. Zhou, *Gradient-index meta-surfaces as a bridge linking propagating waves and surface waves*, Nature Materials. **11** (2012) pp.429-431.

[52] A. Grbic and R. Merlin, *Near-field focusing plates and their design*, IEEE Trans. Antennas Propag. **56** (2008) 10.

[53] M. M. Salary, M. Nazari and H. Mosallaei, *Robust technique for computation of scattering and absorption of light by array of nanowires on layered substrate*, J. Opt. Soc. Am. B. **32** (2015) 12.

[54] F. Aieta, P. Genevet, M. A. Kats, N, Yu, R. Blanchard, Z. Gaburro and F. Capasso, *Aberration-free ultrathin flat lenses and axicons at telecom wavelengths based on plasmonic metasurfaces*, Nano Letters. **12** (2012) 9.

[55] Q. Yang, J. Gu, D. Wang, X. Wang, Z. Tian, C. Ouyang, R. Singh, J. Han and W. Zhang, *Efficient flat metasurface lens for terahertz imaging*, Opt. Express. **22** (2014) 21.

[56] A. Forouzmand, S. Tao, S. Jafar-Zanjani, J. Cheng, M. M. Salary and H. Mosallaei, *Double split-loop resonators as building blocks of metasurfaces for light manipulation: bending, focusing, and flat-top generation*, J. Opt. Soc. Am. **33** (2016) 7.

[57] B, Walther, C. Helgert, C. Rockstuhl, F. Setzpfandt, F. Eilenberger, E. B. Kley, F. Lederer, A. Tuennermann and T Pertsch, *Spatial and spectral light shaping with metamaterials*, Advanced Materials. **24** (2012) 47.

[58] X. Ni, A. V. Kildishev and V. M. Shalaev, *Metasurface holograms for visible light*, Nature Communications. **4** (2013) 2807.

[59] N .Yu, F. Aieta, P. Genevet, M. A. Kats, Z. Gaburro and F. Capasso, *A broadband, background-free quarter-wave plate based on plasmonic metasurfaces*, Nano Letters. **12** (2012) 12.

[60] N. K. Grady, J. E. Heyes, D. R. Chowdhury, Y. Zeng, M. T. Reiten, A. K. Azad, A. J. Taylor, D. A. R. Dalvit and H. T. Chen, *Terahertz metamaterials for linear polarization conversion and anomalous refraction*, Science. **340** (2013) 6138.

[61] Y. J. Chiang and T. J. Yen, *A composite-metamaterial-based terahertz-wave polarization rotator with an ultrathin thickness, an excellent conversion ratio, and enhanced transmission*, Applied Physics Letters. **102** (2013) 011129.

[62] F. Yang and M. Zh, Lei, *Parity-time symmetric cloak with isotropic modulation*, J. Phys. D: Appl. Phys. **49** (2016) 21LT01.

[63] ZH. Chen *et al.*, *A multidirectional cloak for visible light*, J. Phys. D: Appl. Phys. **51** (2018) 155106.

[64] E. Shokatit, N. Granpayeh and M. Danaeifar, *Wideband and multi-frequency infrared cloaking of spherical objects by using the graphene-based metasurface*, Appl. Opt. **56** (2017) 11.

[65] G. Labate, A. Alù and L. Matekovits, *Surface-admittance equivalence principle for nonradiating and cloaking problems*, Phys. Rev. A. **95** (2017) 6.

[66] A. Ospanova, G. Labate, L. Matekovits and A. A. Basharin, *Multipolar passive cloaking by nonradiating anapole excitation*, Sci. Rep. **8** (2018) 12514.

[67] A. Monti *et al.*, *Overcoming mutual blockage between neighboring dipole antennas using a low-profile patterned metasurface*, IEEE Antennas Wirel. Propag. Lett. **11** (2012) pp. 1414 - 1417.

[68] R. Fleury and A. Alù, *Cloaking and invisibility: A review*, Forum Electromagn. Res. Methods Appl. Technol. (FERMAT). **147** (2014) pp. 171-202.

[69] M. Danaeifar, M. Kamyab and A. Jafargholi, *Broadband cloaking with transmission-line networks and metamaterial*, Int. J. RF Microw. C. E. **22** (2012) 6.

[70] P. Y. Chen, J. C. Soric and A. Alù, *Invisibility and cloaking based on scattering cancellation*, Adv. Mater. **24** (2012) 44.

[71] A. Alù and N. Engheta, *Achieving transparency with plasmonic and metamaterial coatings*, Phys. Rev. E. **72** (2005) 1.

[72] A. Alù and N. Engheta, *Cloaking and transparency for collections of particles with metamaterial and plasmonic covers*, Opt. Express. **15** (2007) 12.

[73] F. Bilotti, S. Tricarico and L. Vegni, *Plasmonic metamaterial cloaking at optical frequencies*, IEEE Trans. Nanotechnol. **9** (2010) 1.

[74] A. Monti, F. Bilotti and A. Toscano, *Optical cloaking of cylindrical objects by using covers made of coreshell nanoparticles*, Opt. Express. **36** (2011) 23.

[75] A. Alù and N. Engheta, *Plasmonic and metamaterial cloaking: Physical mechanisms and potentials*, J. Opt. A Pure Appl. Opt. **10** (2008) 9.

[76] A. Alù, *Mantle cloak: Invisibility induced by a surface*, Phys. Rev. B. **80** (2009) 24.

[77] P. Y. Chen and A. Alù, *Mantle cloaking using thin patterned metasurfaces*, Phys. Rev. B. **84** (2011) 20.

[78] P. Y. Chen, F. Monticone and A. Alù, *Suppressing the electromagnetic scattering with an helical mantle cloak*, IEEE Antennas Wireless Propag. Lett. **112** (2011) pp. 15981601.

[79] Y. R. Padooru, A. B. Yakovlev, P. Y. Chen and A. Alù, *Line-source excitation of realistic conformal metasurface cloaks*, J. Appl. Phys. **112** (2012) 10.

[80] G. Labate, S. K. Podilchak, and L. Matekovits, *Closed-form harmonic contrast control with surface impedance coatings for conductive objects*, Appl. Opt. **56** (2017) 36.

[81] L. Matekovits and T. S Bird *Width-modulated microstrip-line based mantle cloaks for thin single- and multiple cylinders*,IEEE Trans. Antennas Propag. **62** (2014) 5.

[82] P. Y. Chen, J. Soric, Y. R. Padooru, H. M. Bernety, A. B. Yakovlev and A. Alù, *Nanostructured graphene metasurface for tunable terahertz cloaking*, New Journal of Physics. **15** (2013) 123029.

[83] A. Balanis *Advanced Engineering Electromagnetics* Hoboken, NJ, USA: Wiley, 1989.

[84] Y. R. Padooru *et al.*, *Dual capacitive-inductive nature of periodic graphene patches: Transmission characteristics at low-THz frequencies*, Phys. Rev. B. **87** (2013) 115401.

[85] Y. R. Padooru, A. B. Yakovlev, P. Y. Chen and A. Alù, *Analytical modeling of conformal mantle cloaks for cylindrical objects using sub-wavelength printed and slotted arrays*, J. Appl. Phys. **112** (2012) 034907.

[86] A. Monti, L. Tenuti, G. Oliveri, A. Alù, A. Massa, A. Toscano and F. Bilotti, *Design of Multi-Layer Mantle Cloaks*, 8th International Congress on Advanced Electromagnetic Materials in Microwaves and Optics Metamaterials, (2014).

[87] M. Danaeifar and N. Granpayeh, *Wideband invisibility by using inhomogeneous metasurfaces of graphene nanodisks in the infrared regime*, J. Opt. Soc. Am. B. **33** (2016) 8.

[88] V. P. Gusynin and S. G. Sharapov, *Transport of dirac quasiparticles in graphene: Hall and optical conductivities*, Phys. Rev. B. **73** (2006) 24.

[89] V. P. Gusynin, S. G. Sharapov, and J. P. Carbotte, *Unusual microwave response of dirac quasiparticles in graphene*, Phys. Rev. Lett. **96** (2006) 25.

[90] G. W. Hanson, *Dyadic greens functions for an anisotropic, non-local model of biased Graphene*, IEEE Trans. Antennas Propag. **56** (2008) 3.

[91] V. P. Gusynin, S. G. Sharapov, and J. P. Carbotte, *Magneto-optical conductivity in graphene*, Journal of Physics: Condensed Matter. **19** (2007) 2.

[92] G. W. Hanson, *Dyadic greens functions and guided surface waves for a surface conductivity model of graphene*, J. Appl. Phys. **103** (2008) 064302.

[93] V. P. Gusynin, S. G. Sharapov, and J. P. Carbotte, *Sum rules for the optical and hall conductivity in graphene*, Phys. Rev. B. **75** (2007) 165407.

[94] A. Vakil, *Transformation optics using graphene: one-atom-thick optical devices based on graphene*, Presented to the faculties of the University of Pennsylvania in partial fulfillment of the requirements for the degree of Doctor of Philosophy, 2012.

[95] N. K. Emani, A. V. Kildishev, V. M. Shalaev and A. Boltasseva, *Graphene: a dynamic platform for electrical control of plasmonic resonance*, Nanophotonics. **4** (2015) 1.

[96] Z. Miao, Q. Wu, X. Li, Q. He, K. Ding, Z. An, Y. Zhang and L. Zhou, *Widely tunable terahertz phase modulation with gate-controlled graphene metasurfaces*, Physical Review X. **5** (2015) 4.

[97] W. Tang, L. Wang, X. chen, C. Liu, A. Yu and W. Lu, *Dynamic metamaterial based on the graphene split ring high-Q Fano-resonnator for sensing applications*, Nanoscale. **8** (2016) 33.

[98] H. Cheng, Ch. Chen, P. Yu, W. Liu, Z. Li, J. Li, B. Xie and J. Tian, *Dynamically Tunable Broadband Infrared Anomalous Refraction Based on Graphene Metasurfaces*, Advanced Optical Materials **3** (2015) 12.

[99] E. Torabi, A. Fallahi and A. Yahaghi, *Evolutionary optimization of graphene-metal metasurfaces for tunable broadband terahertz absorption*, IEEE Trans. Antennas Propag. **65** (2017) 3.

[100] M. Tamagnone, C. Moldovan, et al, *Near optimal graphene terahertz non-reciprocal Isolator*, Nat. Commun. **7** (2016) 11216.

[101] W. Ma *et al.*, *Dual-band light focusing using stacked graphene metasurfaces*, ACS Photonics. **4** (2017) pp. 1770-1775.

[102] M. Esquius-Morote, J. S. Gmez-Daz and J. Perruisseau-Carrier *Sinusoidally modulated graphene leaky-wave antenna for electronic beamscanning at THzl* , IEEE Trans. Antennas Propag. **4** (2014) 1.

[103] M. Selvanayagam and G. V. Eleftheriades, *An active electromagnetic cloak using the equivalence principle*, IEEE Antennas and Wireless Propagation Letters. **11** (2012) 12261229.

[104] D. Schurig, J. J. Mock, B. J. Justice, S. A. Cummer, J. B. Pendry, A. F. Starr, and D. R. Smith, *Metamaterial Electromagnetic Cloak at Microwave Frequencies*, Science. **314** (2006) 5801.

[105] M. Danaeifar, M. Kamyab and A. Jafargholi, *Broadband Cloaking with Transmission Line Networks and Metamaterials*, International Journal of RF and Microwave Computer-Aided Engineering. **22** (2012) 6.

[106] P. Alitalo *et al.*, *Transmission-Line Networks Cloaking Objects From Electromagnetic Fields*, IEEE Trans. Antennas Propag. **56** (2008) 2.

[107] J. Li and J. B. Pendry, *Hiding under the carpet: A new strategy for cloaking*, Phys. Rev. Lett. **101** (2008) 203901.

[108] Z. Sharifi and Z. Atlasbaf, *New procedure to design low radar cross section near perfect isotropic and homogeneous triangular carpet cloaks*, J. Opt. Soc. Am. A. **33** (2016) 10.

[109] A. Alu, D. Rainwater, and A. Kerkhoff, *Plasmonic cloaking of cylinders: ' finite length, oblique illumination and cross-polarization coupling* , New J. Phys. **12** (2010) 10.

[110] M. Danaeifar, M. Booket and N. Granpayeh, *Optical invisibility of cylindrical structures and homogeneity effect on scattering cancellation method* , Electronics Letters. **52** (2016) 1.

[111] F. F. Qin, Z. Z. Liu, Q. Zhang, H. Zhang, and J. J. Xiao, *Mantle Cloaks Based on the Frequency Selective Metasurfaces Designed by Bayesian Optimization*, Sci Rep. **8** (2018) 14033.

[112] A. Vitiello *et al.*, *Waveguide characterization of S-Band microwave mantle cloaks for dielectric and conducting objects*, Sci Rep. **6** (2016) 19716.

[113] S. Vellucci, A. Monti, M. Barbuto, A. Toscano and F. Bilotti, *Satellite applications of electromagnetic cloaking*, IEEE Trans. Antennas Propag. **65** (2017) 9.

[114] J. C. Soric, P. Y. Chen, A. Kerkhoff, D. Rainwater, K. Melin and A. Alu, *Demonstration of an ultralow profile cloak for scattering suppression of a finite-length rod in free space*, New Journal of Physics. **15** (2013) 033037.

[115] A. Farmani, M. Miri, and M. H. Sheikhi, *Design of a High Extinction Ratio Tunable Graphene on White Graphene Polarizer*, IEEE Photonics Technology Letters. **30** (2018) 2.

[116] Y.R. Padooru *et al.*, *Design of a high extinction ratio tunable graphene on white graphene polarizer*, IEEE Photonics Technology Letters. **30** (2018) 2.

[117] S. Vellucci *et al.*, *Scattering manipulation and camouflage of electrically small objects through metasurfaces*, Phys. Rev. Appl. **7** (2017) 3.

[118] A. Monti *et al.*, *Anisotropic mantle cloaks for TM and TE scattering reduction*, IEEE Trans. Antennas Propag. **63** (2015) 4.

[119] CST Microwave Studio. (ver. 2017).

[120] A. Forouzmand and A. B. Yakovlev, *Electromagnetic cloaking of a finite conducting wedge with a nanostructured graphene metasurface*, IEEE Trans. Antennas Propag. **63** (2015) 5.

[121] P. Y. Chen, A. B. Yakovlev, C. Argyropoulos and A. Alù, *Broadening the cloaking bandwidth with non-foster metasurfaces*, Phys. Rev. Lett. **111** (2013) 233001.

[122] F. Bilotti, S. Tricarico and L. Vegni, *Electromagnetic cloaking devices for TE and TM polarizations*, New J. Phys. **10** (2008) 11.

[123] HFSS. Version 2015.

[124] S. A. H. Gangaraj, T. Low, A. Nemilentsau and G. W. Hanson, *Directive surface plasmons on tunable two-dimensional hyperbolic metasurfaces and black phosphorus: Greens function and complex plane analysis*, IEEE Trans. Antennas Propag. **65** (2017) 3.

[125] Q. Yang, J. Gu *et al.*, *Efficient flat metasurface lens for terahertz imaging*, Opt Express. **22** (2014) 21.

[126] X. Zhang and Z. Liu, *Superlenses to overcome the diffraction limit*, Nat Mat. **7** (2008) pp. 435441.

[127] X. Chen *et al.*, *Longitudinal multifoci metalens for circularly polarized light*, Adv. Optical Mater. **3** (2015) 9.

[128] Z. Bomzon *et al.*, *Space-variant Pancharatnam-Berry phase optical elements with computer-generated subwavelength gratingst*, Opt. Lett. **27** (2002) 13.

[129] Y. Zhao and A. Alù, *Manipulating light polarization with ultrathin plasmonic metasurfaces*, Phys Rev B. **84** (2011) 205428.

[130] A. Pors *et al.*, *Focusing flat mirrors based on plasmonic gradient metasurfaces*, Nano Lett. **13** (2013) 2.

[131] F. Aieta *et al.*, *Aberration-free ultrathin flat lenses and axicons at telecom wavelengths based on plasmonic metasurfaces*, Nano Lett. **201** (2011) 12.

[132] A. Forouzmand and A.B. Yakovlev, *Tunable dual-band subwavelength imaging with a wire medium slab loaded with nanostructured graphene metasurfaces*, AIP Adv. **201** (2015) 5.

[133] G.W. Hanson *et al.*, *Quantum plasmonic excitation in graphene and loss-insensitive propagation*, Phys Rev A. **92** (2015) 013828.

[134] P.Y. Chen, M. Farhat and H. Bac, *Graphene metascreen for designing compact infrared absorbers with enhanced bandwidth*, Nanotechnology. **26** (2015) 164002.

[135] A. Farmani, M. Miri and M.H. Sheikhi, *Analytical modeling of highly tunable giant lateral shift in total reflection of light beams from a graphene containing structure*, Opt Commun. **391** (2017) pp. 68-76.

[136] SH, Luo *et al.*, *Broadband tunable terahertz polarization converter based on graphene metamaterial*, Opt Commun. **413** (2018) pp. 184189.

[137] V. Gruev, R. Perkins, T. York, CCD, *polarization imaging sensor with aluminum nanowire optical filters*, Opt. Express. **18** (2010) 18.

[138] X. Zhao, F. Boussaid, A. Bermak, V.G. Chigrinov, *High-resolution thin guest-host micropolarizer arrays for visible imaging polarimetry*, Opt. Express. **19** (2011) 6.

[139] F. Heismann, R.C. Aferness, *Wavelength-tunable electrooptic polarization conversion in birefringent waveguides*, IEEE J. Quantum Electron. **24** (1988) 1.

[140] H. Lajunen, J. Turunen, J. Tervo, *Design of polarization gratings for broadband illumination*, Opt. Express. **13** (2005) 8.

[141] D.R. Smith, W.J. Padilla, D.C. Vier, S.C. Nemat-Nasser, S. Schultz, *Composite medium with simultaneously negative permeability and permittivity*, Phys. Rev. Lett. **84** (2000) 4184.

[142] D. Schurig, J.J. Mock, B.J. Justice, S.A. Cummer, J.B. Pendry, A.F. Starr, D.R. Smith, *Metamaterial electromagnetic cloak at microwave frequencies*, Science. **314** (2006) 5801.

[143] N. Fang, H. Lee, C. Sun, X. Zhang, *Subdiffraction-limited optical imaging with a silver superlens*, Science. **308** (2005) 5721.

[144] M. Mutlu, A.E. Akosman, A.E. Serebryannikov, E. Ozbay, *Asymmetric chiral metamaterial circular polarizer based on four U-shaped split ring resonators*, Opt. Lett. **36** (2011) 9.

[145] N. Yu, F. Aieta, P. Genevet, M.A. Kats, Z. Gaburro, F. Capasso, *A broadband, background-free quarter-wave plate based on plasmonic metasurfaces*, Nano Lett. **12** (2012) 12.

[146] N. K. Grady *et al.*, *Terahertz Metamaterials for Linear Polarization Conversion and Anomalous Refraction*, Science. **340** (2013) 6138.

[147] D. R. Jackson and N. G. Alexopoulos, *Gain enhancement methods for printed-circuit antennas*, IEEE Trans. Antennas Propag. **33** (1985) 976987.

[148] Y. Li and J. Wang, *Dual-Band Leaky-Wave Antenna Based on DualMode Composite Microstrip Line for Microwave and Millimeter-Wave Applications*, IEEE Trans. Antennas Propag. **66** (2018) 4.

[149] A. A. Oliner, *Radiating periodic structures: Analysis in terms of k vs. diagrams, in Short Course on Microwave Field and Network Technique*, Polytechnic Inst. Brooklyn Graduate Center, New York, NY, USA. (1963).

[150] A. A. Oliner and D. R. Jackson, *Leaky-wave antennas*, in Antenna Engineering Handbook. Ed., 4th ed. New York, NY, USA: McGraw-Hill. (2007).

[151] J. H. Wang and K. K. Mei, *Theory and analysis of leaky coaxial cables with periodic slots*, IEEE Trans. Antennas Propag. **49** (2001) 12.

[152] F. L. Whetten and C. A. Balanis, *Meandering long slot leaky-wave waveguide-antennas*, IEEE Trans. Antennas Propag. **39** (1991) 11.

[153] H. Oraizi, A. Amini, A. Abdolali, and A. M. Karimimehr, *Design of Wideband Leaky-Wave Antenna Using Sinusoidally Modulated Impedance Surface Based on the Holography Theory*, IEEE Antennas Wirel. Propag. Lett. **17** (2018) 10.

[154] A. A. Oliner and A. Hessel, *Guided waves on sinusoidally-modulated reactance surfaces*, IRE Trans. Antennas Propag. **7** (1959) pp. 201208.

[155] N. Javanbakht, M. S. Majedi, and A. R. Attari, *Thinned Array Inspired Quasi-Uniform Leaky-Wave Antenna With Low Side-Lobe Level,*IEEE Antennas Wirel. Propag. Lett. **16** (2017) pp. 29922995.

[156] K. Hosseini and Z. Atlasbaf, *Analysis and synthesis of singly-curved microstrip structures utilizing modified Schwarz-Christoffel transformation*, IEEE Trans. Antennas Propag. **61** (2013) 12.

[157] L. M. Viculis, J. J. Mack, and R. B. Kaner, *A chemical route to carbon nanoscrolls*, Science. **299** (2003) 1361.

[158] P. R. Somani, S. P. Somani, and M. Umeno, *Planer nanographenes from camphor by CVD*, Chemical Physics Letters, **430** (2006) 56.

[159] J.S Gomez-Diaz, et. al, *Self-biased reconfigurable graphene stacks for terahertz plasmonics*, Nat Commun, . **6** (2015) 6334.

[160] M Esquius-Morote, et. al, *Sinusoidally modulated graphene leaky-wave antenna for electronic beamscanning at THz*, IEEE Trans Terahertz Sci Technol, . **4** (2014) pp. 116122.

[161] C Wang, et. al, *Dynamically tunable deep subwavelength high-order anomalous reflection using graphene metasurfaces*, Adv Opt Mater, . **6** (2018) 1701047.

Abstract

**Applications of Graphene Metasurfaces for Manipulation
of Electromagnetic Waves Scattering**

By
Zahra Hamzavi Zarghani

In this thesis, several graphene-based metasurfaces have been designed using two commercial software: CST Microwave Studio and HFSS. In the considered projects, analytical and numerical results agree very well which verifies the correctness of analytical approaches presented in the thesis.

Firstly, mantle cloaking of a dielectric cylinder under the oblique illumination of an incident TM_z polarized plane wave is considered. The required surface impedance of a covering metasurface is analytically obtained. By changing chemical potential of graphene, mantle cloaking is achieved for different frequencies and incident angles. In the next sections, dual-polarized tunable mantle cloaking for TM_z and TE_z incident wave is achieved by covering the dielectric cylinder with graphene strips. Scattering manipulation of dielectric and conducting cylinders are also studied. It is shown that by covering the cylinders with graphene nano-patches and by changing the chemical potential of graphene, the radar cross-sections of the cylinders transform to that of the smaller or larger cylinders.

A reconfigurable graphene-based metasurface lens is designed. By changing the chemical potential of the graphene, its operation frequency, and focal point change. Next, a tunable polarization converter based on graphene wires is designed which rotates the linear polarization of the incident wave with tunable operation. Finally, a graphene-based leaky wave antenna is designed whose gain is increased by loading it with a dielectric slab.

Keywords: Cloaking, Graphene, Lens, Metasurface.

به نام خدا

...عنوان پایان‌نامه/رساله در این‌جا نوشته شود...

به کوشش

...نام و نام خانوادگی دانشجو در این‌جا نوشته شود...

پایان‌نامه/رساله

ارائه شده به دانشگاه شیراز به عنوان بخشی از فعالیت‌های تحصیلی لازم

برای اخذ درجه‌ی کارشناسی ارشد/دکتری

در رشته

...عنوان کامل رشته-گرایش تحصیلی در این‌جا نوشته شود...

دانشگاه شیراز

شیراز

جمهوری اسلامی ایران

ارزیابی کمیته‌ی پایان‌نامه/رساله، با درجه‌ی: ...درجه‌ی ارزیابی در این‌جا نوشته شود...

دکتر ...نام و نام خانوادگی استاد راهنما...، ...مرتبه‌ی علمی... ...بخش... (استادراهنما)...........................

دکتر ...نام و نام خانوادگی استاد مشاور...، ...مرتبه‌ی علمی... ...بخش... (استاد مشاور)...........................

دکتر ...نام و نام خانوادگی استاد مشاور...، ...مرتبه‌ی علمی... ...بخش... (استاد مشاور)...........................

دکتر ...نام و نام خانوادگی داور...، ...مرتبه‌ی علمی... ...محل اشتغال... (داور خارج از دانشگاه).............

دکتر ...نام و نام خانوادگی داور...، ...مرتبه‌ی علمی... ...بخش... (داور متخصص داخلی)...........................

خرداد ۱۳۹۹

به نام خدا

تعهدنامه

اینجانب ...نام و نام خانوادگی دانشجو در اینجا نوشته شود... به شمارهی دانشجویی ...شمارهی دانشجویی در اینجا نوشته شود... دانشجوی مقطع کارشناسی ارشد/دکتری تأیید میکنم که این پایاننامه/رساله حاصل پژوهش خودم است و در مواردی که از منابع دیگران استفاده شده، نشانی دقیق و مشخصات کامل آن را نوشتهام. همچنین اظهار مینمایم که تحقیق و موضوع پایاننامه/رسالهام تکراری نیست و موارد زیر را نیز تعهد میکنم:

۱- بدون کسب مجوز دانشگاه شیراز و اجازه از استاد(ان) راهنما، تمام یا قسمتی از دستاوردهای پایان-نامه/رسالهی خود را در مجامع و رسانههای علمی اعم از همایشها و مجلات داخلی و خارجی به صورت مکتوب یا غیرمکتوب منتشر ننمایم.

۲- اسامی افراد خارج از کمیتهی پایاننامه/رساله را بدون اجازهی استاد(ان) راهنما به جمع نویسندگان مقالههای مستخرج از پایاننامه/رساله نامه اضافه نکنم.

۳- از درج نشانی یا وابستگی کاری (affiliation) نویسندگان سازمانهای دیگر (غیر از دانشگاه شیراز) در مقالههای مستخرج از پایاننامه/رساله بدون تأیید استاد(دان) راهنما اجتناب نمایم.

همهی حقوق مادی و معنوی این اثر مطابق با آییننامهی مالکیت فکری، متعلق به دانشگاه شیراز است. چنانچه مبادرت به عملی خلاف این تعهدنامه محرز گردد، دانشگاه شیراز در هر زمان و به هر نحو مقتضی حق هرگونه اقدام قانونی را در استیفای حقوق خود دارد.

...نام و نام خانوادگی دانشجو در اینجا نوشته شود...

امضا و تاریخ:

<div dir="rtl">

به نام خدا

تعهدنامه

اینجانب زهرا حمزوی زرقانی به شماره دانشجویی۹۳۳۰۱۹۰ دانشجوی مقطع دکتری تأیید میکنم که این رساله حاصل پژوهش خودم است و در مواردی که از منابع دیگران استفاده شده، نشانی دقیق و مشخصات کامل آن را نوشتهام. همچنین اظهار مینمایم که تحقیق و موضوع رسالهام تکراری نیست و موارد زیر را نیز تعهد میکنم:

۱- بدون کسب مجوز دانشگاه شیراز و اجازه از استادان، تمام یا قسمتی از دستاوردهای رساله خود را در مجامع و رسانههای علمی اعم از همایشها و مجلات داخلی و خارجی به صورت مکتوب یا غیرمکتوب منتشر ننمایم.

۲- اسامی افراد خارج از کمیتهپایاننامه/رساله را بدون اجازه استادان راهنما به جمع نویسندگان مقالههای مستخرج از پایاننامه/رساله اضافه نکنم.

۳- از درج نشانی یا وابستگی کاری (affiliation) نویسندگان سازمانهای دیگر (غیر از دانشگاه شیراز) در مقالههای مستخرج از رساله بدون تأیید استادان راهنما اجتناب نمایم.

همه حقوق مادی و معنوی این اثر مطابق با آییننامه مالکیت فکری، متعلق به دانشگاه شیراز است. چنانچه مبادرت به عملی خلاف این تعهدنامه محرز گردد، دانشگاه شیراز در هر زمان و به هر نحو مقتضی حق هرگونه اقدام قانونی را در استیفای حقوق خود دارد.

زهرا حمزوی زرقانی

امضا و تاریخ:

</div>

دانشکده مهندسی برق و کامپیوتر

رساله دکتری در رشته مهندسی برق (مخابرات میدان)

طراحی فراسطوح گرافنی برای شکل دهی پراکندگی امواج الکترومغناطیسی

به کوشش

زهرا حمزوی زرقانی

استادان راهنما:

دکتر علیرضا یاحقی

Dr. Ladislau Matekovits

مهر ۱۳۹۸